# MULTI-SCALE MULTI-PHYSICS MODELING OF LASER POWDER BED FUSION ADDITIVE MANUFACTURING

A Dissertation

by

KUBRA KARAYAGIZ

Submitted to the Office of Graduate and Professional Studies of
Texas A&M University
in partial fulfillment of the requirements for the degree of

DOCTOR OF PHILOSOPHY

| | |
|---|---|
| Chair of Committee, | Raymundo Arroyave |
| Committee Members, | Alaa Elwany |
| | Miladin Radovic |
| | Ibrahim Karaman |
| Head of Department, | Ibrahim Karaman |

August 2019

Major Subject: Materials Science and Engineering

# ABSTRACT

Laser Powder Bed Fusion (LPBF) is a fast-developing metal additive manufacturing process offering unique capabilities including geometric freedom, flexibility, and part customization. The process induces complicated thermal histories with high temperature gradients and cooling rates, leading to rapid solidification microstructures with anisotropic properties as different from those produced conventionally.

In addition, the LPBF parts exhibit to a large extent of in-sample and sample-to-sample variabilities in the microstructure and consequently part performance. The high variability in the microstructure and properties is considered the major obstacle against the widespread adoption of LPBF as a viable manufacturing technique. Therefore, a more in depth understanding and control of the solidification microstructure is needed to achieve the LPBF fabricated parts with desired properties.

Since the solidification microstructure is highly influenced by the thermal input, it is essential to have an accreditable thermal model first. Therefore, a portion of this dissertation was devoted to developing an accurate thermal model through various methods including code-to-code verification and experimental validation. The materials used in this portion include Ti-6Al-4V, NiTi-SMA (Shape Memory Alloy).

Next, a multi-scale multi-physics modeling framework which couples a finite element (FE) thermal model to a non-equilibrium phase field (PF) model was developed to investigate the rapid solidification microstructure during LPBF. The framework was utilized to predict the spatial variation in the morphology, size and micro-segregation in the single-track deposition of binary NiNb alloy during LPBF and a very good agreement with the experimental measurements was achieved.

# DEDICATION

To my daughter.

# ACKNOWLEDGEMENTS

First and foremost, I would like to express my sincere gratitude to my advisor Dr. Raymundo Arroyave for the continuous support of my doctorate study. Without his patience, guidance, motivation, and excellent supervision this work could not have accomplished.

Second, I want to thank my committee members: Dr. Alaa Elwany, Dr. Ibrahim Karaman and Dr. Miladin Radovic, as well as Dr. Ji Ma, for their continued guidance, support, advice and suggestions that made possible reaching the objectives of this dissertation.

I also would like to thank my fellow lab members and collaborators, especially Dr. Anjana Talapatra, Dr. Thien Duong, Dr. Gustavo Tapia, Dr. Luke Johnson, Dr. Brian Franco, Dr. Mo Mahmoudi, Raiyan Seede, and Vahid Attari for their insightful discussions and help in my research.

I owe my deepest gratitude to my life partner and colleague, Dr. Omer Karakoc for his understanding, support, patience, and encouragement. Last but not the least, I would like to thank my family: my parents, my in-laws, and my sister. They supported me in so many ways throughout my PhD study and my life as well.

# CONTRIBUTORS AND FUNDING SOURCES

## Contributors

This work was supervised by a dissertation committee consisting of committee chair, Professor Raymundo Arroyave of the Department of Materials Science and Engineering, and committee members, Professor Ibrahim Karaman of the Department of Materials Science and Engineering, Professor Miladin Radovic of the Department of Materials Science and Engineering and Professor Alaa Elwany of the Department of Industrial and Systems Engineering.

The experimental data presented in Chapter 2 was conducted by Brian Franco of the Department of Materials Science and Engineering and Gustavo Tapia of the Department of Industrial and Systems Engineering. The experimental analyses depicted in Chapter 3 was performed by Brian Franco of the Department of Materials Science and Engineering. The computational data for Model 2 presented in Chapter 3 was provided by Christapher Lang of NASA Langley Space Center. The thermal predictions utilized in Chapter 4 was performed by Luke Johnson of the Department of Materials Science and Engineering. The experimental data analyzed for Chapter 4 was provided by Raiyan Seede and Bing Zhang of the Department of Industrial and Systems Engineering. All other work conducted for the dissertation (or) dissertation was completed by the student independently.

## Funding Sources

Portions of this dissertation were supported by an Early Stage Innovations grant from NASA’s Space Technology Research Grants Program, Grant No. NNX15AD71G.

Portions of this dissertation were supported by Lawrence Livermore National Laboratory under Collaborative R&D in Support of LLNL Missions, Task Order No. B623252 and Master Task Agmt. B575363.

The FE and PF simulations were carried out at the Texas A&M Super Computing Center.

## TABLE OF CONTENTS

Page

ABSTRACT .......... ii

DEDICATION .......... iv

ACKNOWLEDGEMENTS .......... v

CONTRIBUTORS AND FUNDING SOURCES .......... vi

TABLE OF CONTENTS .......... viii

LIST OF FIGURES .......... xi

LIST OF TABLES .......... xvi

1. INTRODUCTION .......... 1

2. NUMERICAL AND EXPERIMENTAL ANALYSIS OF HEAT DISTRIBUTION IN THE LASER POWDER BED FUSION OF TI-6AL-4V .......... 8

- 2.1 Overview .......... 8
- 2.2 Introduction .......... 9
- 2.3 Literature Review .......... 13
  - 2.3.1 Powder Bed Modeling .......... 13
  - 2.3.2 Physical Mechanisms during LPBF .......... 13
    - 2.3.2.1 Heat Transfer .......... 13
    - 2.3.2.2 Fluid Flow .......... 16
  - 2.3.3 Material Properties .......... 17
  - 2.3.4 Heat Source Modeling .......... 19
  - 2.3.5 Volume Shrinkage and Layer Built .......... 21
  - 2.3.6 Thermal Distribution Analysis in Metal Based AM Process 21
- 2.4 Model Descriptions .......... 23
  - 2.4.1 Assumptions .......... 24
  - 2.4.2 Physical Description of the Model .......... 25
  - 2.4.3 Initial and Boundary Conditions .......... 27
  - 2.4.4 Moving Heat Source .......... 28
  - 2.4.5 Material Properties .......... 29
  - 2.4.6 Evaporation .......... 30

2.5 Experimental Details ........ 32
  2.5.1 Experimental Testbed ........ 32
  2.5.2 Experimental Validation ........ 33
2.6 Results and Discussion ........ 35
  2.6.1 Simulation Results ........ 35
    2.6.1.1 HAZ Size ........ 35
    2.6.1.2 Melt Pool Size ........ 36
    2.6.1.3 Thermal History ........ 37
    2.6.1.4 Cooling Rates ........ 43
  2.6.2 Sensitivity Analysis ........ 43
    2.6.2.1 Effect of Material Parameters ........ 44
    2.6.2.2 Effect of Evaporation ........ 48
2.7 Summary and Conclusions ........ 49

3. VERIFICATION ASSESSMENT OF TWO FINITE ELEMENT THERMAL MODELS FOR LASER POWDER BED FUSION ADDITIVE MANUFACTURING ........ 52

3.1 Overview ........ 52
3.2 Introduction ........ 53
3.3 Literature Review ........ 59
3.4 Mathematical Description of Models ........ 63
  3.4.1 Model 1 ........ 64
  3.4.2 Model 2 ........ 72
3.5 Model Verification ........ 73
  3.5.1 Effect of Mesh Size ........ 74
  3.5.2 Effect of Error Tolerance ........ 79
  3.5.3 Effect of Domain Size ........ 82
  3.5.4 Code-to-Code Verification ........ 83
    3.5.4.1 Case Study 1 (Localized Heat Source) ........ 84
    3.5.4.2 Case Study 2 (Single-Track Laser Melting) ........ 86
    3.5.4.3 Case Study 3 (Multi-Track Laser Melting) ........ 89
3.6 Model Validation ........ 90
3.7 Summary and Conclusion ........ 91

4. FINITE INTERFACE DISSIPATION PHASE FIELD MODELING OF NI-NB UNDER ADDITIVE MANUFACTURING CONDITIONS ........ 93

4.1 Overview ........ 93
4.2 Introduction ........ 93
4.3 Experimental Methodology ........ 101

4.4 Mathematical Description of Models .......................................................... 102
  4.4.1 Thermal Model ........................................................................... 102
  4.4.2 Phase Field Model with Finite Interface Dissipation .......................... 108
  4.4.3 Computational Procedures ................................................................. 112
    4.4.3.1 Macroscopic Thermal Model ................................................ 112
    4.4.3.2 Finite Interface Dissipation Phase Field Model ...................... 113
4.5 Results and Discussion ....................................................................... 115
  4.5.1 Macrostructure Characterization: Experiments .................................. 116
  4.5.2 Microstructure Characterization: Experiments .................................. 118
  4.5.3 General Features of the Microstructure ............................................... 120
  4.5.4 Microstructural Variability as a Function of Thermal Parameters (G, R) ................................................................. 125
  4.5.5 Microstructural Variability as a Function of Process Parameters .......................................................... 130
    4.5.5.1 Effects of Temperature Gradient, Growth Rate, and Cooling Rate ............................................................................ 131
    4.5.5.2 Morphology and Size ............................................................. 135
4.6 Summary and Conclusion ............................................................................. 143

5. SUMMARY AND FUTURE WORK ................................................................ 146

REFERENCES ............................................................................................ 149

APPENDIX A ............................................................................................ 163

APPENDIX B ............................................................................................ 164

# LIST OF FIGURES

FIGURE Page

1.1 Principles of powder bed fusion (PBF) process (top) and dominant physical mechanisms during melting (bottom)………………………….. 2

2.1 Physical mechanisms during Laser powder bed fusion (LPBF). Physical mechanisms considered in the present work are highlighted in yellow rectangles ……………………...…………………………….... 12

2.2 3-dimensional model and meshing geometry (a), and the scanning strategy during LPBF simulations (b). The Asterisk represents the position of the selected point at which temperature is calculated during simulation………………………………………………………… 24

2.3 Thermo-physical properties of Ti-6Al-4V (solid properties are reported in [69], liquid properties are extrapolated according to [23], powder properties are calculated based on equations 7 and 8)………… 28

2.4 ProX 100 DMP build chamber before (a) and after (b) custom integrating the ThermaViz sensor…………………………………………. 32

2.5 Comparison of HAZ size from the experiment (b) and simulation (a). The experimental HAZ width and depth in the substrate are measured in the range of 218±21 μm and 64.4±1.5 μm, respectively. The predicted HAZ width and depth in the substrate are 211 μm and 72 μm………...……………………………………...………………. 34

2.6 Melt pool size and geometry of Ti-6Al-4V alloy for the conditions provided in Table 2.1. The depth in the substrate, width and length of the melt pool are predicted as 22 μm, 144 μm, 149 μm, respectively........................................................................................... 36

2.7 Comparison of the thermal history from the experiments and simulations. The small peaks in the experimental results demonstrate the spatters (a). Calculated heating-cooling rate history at the selected point on the first track (b). Evolution of the melt pool, which is indicated by a circle, during LPBF. The images are taken at the times that correspond to the peaks above 900 K in the top-left figure. The small square that is in the middle of the first track corresponds to where the average temperature is calculated. The arrows in the bottom of the Figure 2.2.demonstrate the moving direction of the melt pool (c)………………………………………………………………... 41

2.8 Effects of thermal conductivity of the liquid phase on the predicted thermal history. $K_L$ represents the thermal conductivity of the bulk material………………………………………………………………... 44

2.9 Effect of the thermal conductivity of the liquid phase (a) and absorptivity (b) on the predicted HAZ and melt pool sizes...…………… 44

2.10 Change in the predicted HAZ geometry and size for different porosity values of 0.35, 0.45, 0.55. The red arrow indicates the front side of the HAZ ………………………………………………………… 46

2.11 Comparison of the single track thermal histories from the models without (case 1) and with (case 2) taking evaporation into account ….... 48

3.1 Model verification and validation process ……………………………… 55

3.2 Three-dimensional simulation domain and meshing geometry and the scanning strategy during LPBF simulations for the two cases: (a) single track, (b) three tracks in Model 1. Symmetry plane in the single-track model is shaded in red (a). The red dot represents the position of the selected point at which thermal history is measured for two cases: (c) single track, (d) three tracks..………………………… 64

3.3 For model 2, (a) the three-dimensional simulation domain and meshing geomety for single-track case, (b) and the position of Point *A* within the simulation domain where metrics a remeasured..…………… 68

3.4 Thermo-physical properties of Ti-6Al-4V (solid properties are reported in [69], liquid properties are extrapolated according to [23], powder properties are calculated based on Equations 11 and 12)……… 73

3.5 Effect of mesh refinement on the melt pool length and total computation time is presented……..…………………………………………… 75

3.6 Thermal history is plotted for the three different mesh sizes: fine (15 µm), medium (35 µm), coarse (55 µm). The corresponding peak temperatures for coarse, medium and fine meshes are 3852 K, 3477 K, 3315 K…...……………………………………………………… 77

3.7 The thermal history with varying error tolerance is depicted for select tests. A convergence problem appears at the solution for Test 3 with the high tolerances…..…………………………………………… 80

3.8 Thermal history plots for different domain sizes. Note the high cooling rate at small domain indicating the interference of the boundary conditions.……………………………………………………..………… 83

3.9 Block Geometry (Localized heat source is directed to the center of the top surface)...……………………………………………………... 84

3.10 Excellent agreement between the two models is achieved for Case Study 1. Note the decrease in the peak temperatures in case 2 with temperature dependent material properties and phase transition between solid and liquid……………………………………………………….. 85

3.11 Predicted thermal histories from both models are presented for Case Study 2. Reduction on the maximum predicted temperature due to evaporation is clearly seen on the plots……….……………………… 87

3.12 Predicted thermal histories from both models for Case Study 3 are presented. The thermal histories are measured at the point A, as shown in Figure 2 (d) and Figure 3 (b), respectively for Model 1 and Model 2……………………………………………………………… 88

3.13 Comparison of experimentally measured melt pool sizes (width and depth in the substrate) with the predicted values. The melt pool width and depth in the substrate were measured as 161.8±10.87 µm and 18.2±7.66 µm (a), indicating 11 % and 20.9% errors with the predicted values of 144 µm and 22 µm (b), respectively…...………………… 90

4.1 The coupling of the thermal model with the phase field model is illustrated. An example of predicted heat affected region of Ni-5wt. %Nb alloy during LPBF is presented on the three-dimensional thermal model geometry. The temperature gradient *G* and growth rate *R* are extracted from the thermal model and fed into the phase field model to predict the microstructure at the corresponding location at the melt pool indicated by a small rectangle in the magnified view of the heat affected region……………………………………………….. 103

4.2 Optical micrographs demonstrating transverse cross-sections of melt pool obtained under (a) P: 162 W, V: 957 mm/s, LED (low): 0.169 J/mm (b) P:96 W, V: 67 mm/s, LED (medium): 1.43 J/mm (c) P: 122 W, V: 50 mm/s, LED (high): 2.44 J/mm. From left, to right a clear transition from conduction mode to keyhole mode is shown…….... 116

4.3 The microstructure of the selected rectangular regions in Fig. 4.2 are characterized using SEM (middle column), WDS (right column), and WDS line scans (left column). SEM images show cellular and planar morphologies for the corresponding LED conditions in Fig. 4.2……………………………………………………………..……… 118

4.4 Typical cellular microstructure forms under LPBF condition. Nb concentration varies along line A (a), B (b), and C (c)…….………………. 121

4.5 Phase field evolution of the tip velocity and tip undercooling with time…………………………………………………………………. 122

4.6 The variation in morphology, size, and microsegregation as a function of growth rate and temperature gradient is shown……...…………... 125

4.7 The calculated primary dendrite arm spacing (PDAS) reduces as the cooling rate increases.As the solidification growth rate \$R\$ increases the segregation coefficient increases……..……………………………… 126

4.8 The predicted temperature gradient, G and growth rate, R are shown for varying solidification front depths for two set of process parameters………………………………………………………………. 130

4.9 The predicted cooling rates at varying solidification front depths are shown for two set of process parameters…………..……………………. 131

4.10 Variation in G and R are shown across the melt pool…………………… 132

4.11 The calculated G and R along the transverse section of the melt pool boundary are shown for two set of process parameters with different linear energy densities (LED)………………………………...………. 133

4.12 Variation in the cellular structure and size at varying cooling rates along the melt pool boundary is shown for high LED condition….…….. 136

4.13 Variation in the solidification structure and size at varying cooling rates along the melt pool boundary is shown for low LED condition. A transition from cell to plane structure is observed at high cooling rates……………………………………………………………………… 137

4.14 The predicted growth morphology and size throughout the melt pool are demonstrated along with the experimental measurements. Planar structure is observed throughout the melt pool. (P: 162 W, V: 957 mm/s, LED: 0.169 J/mm) ……………………………………….. 138

4.15 The predicted growth morphology and size throughout the melt pool are demonstrated along with the experimental measurements. Cellular structure is observed throughout the melt pool. (P: 96 W, V: 67 mm/s, LED: 1.43 J/mm) …..……………………………………… 139

4.16 The predicted growth morphology and size throughout the melt pool are demonstrated along with the experimental measurements at the corresponding locations. A transition from a planar to a cellular structure from the bottom to the top of the melt pool is observed. (P: 122 W, V: 50 mm/s, LED: 2.44 J/mm)…………..………….. 140

# LIST OF TABLES

TABLE Page

2.1 Materials and process parameters used in the simulations………………. 29

3.1 Materials and process parameters used in the simulations………………. 69

3.2 Mesh Convergence Study…………………………………………….... 76

3.3 Effect of Error Tolerances on the Computation Time…………………… 78

3.4 Effect of Domain Size on the Solution Accuracy and the Computation Time…...…………………………………………………….... 81

3.5 Predicted Melt Pool Sizes for Case Study 2…………………………..... 87

4.1 Thermophysical and processing parameters used in the FE thermal model. All thermophysical property values were calculated using a weighted average of the pure elemental properties of Ni and Nb……….. 105

4.2 The material properties used in the phase field simulations……………… 114

# 1. INTRODUCTION *

Additive Manufacturing (AM) refers to the processing technologies in which the three-dimensional objects are created directly from a digital CAD model by adding materials layer by layer. 3D printing, solid freeform fabrication, rapid prototyping are other common names used for these processes. Over the past decade, an increasing attention has been drawn to AM processes, especially in biomedical, dental and aerospace industries. The market for AM was reported as $3 billion in 2013 and an increase to more than $21 billion is expected by 2020 [1]. Various powder-based AM processes have been developed over the past years to produce metallic parts. These powder-based AM processes can be categorized under two groups as powder-bed and powder-injection. In powder bed-based AM processes, metallic powder is spread on a substrate before scanned by the heat source, whereas being provided to a moving nozzle to be deposited in the powder injection-based AM. Powder injection based processes can be further classified under Laser Engineered Net Shaping, Laser Cladding, Laser Metal Deposition Shaping, Directed Light Fabrication and Direct Metal Deposition[2], while powder bed based processes can be divided into two sub-group depending on whether the material is fully melted or partially melted. Among the numerous powder-bed based processes, Laser Powder Bed Fusion (LPBF) and Electron Beam Melting (EBM) are the most popular techniques due to their ability to produce fully dense parts with strong properties. In this

---

* Portions of this section are reprinted with permission from Karayagiz, K., et al., *Numerical and experimental analysis of heat distribution in the laser powder bed fusion of Ti-6Al-4V.* IISE Transactions, 2019. **51**(2): p. 136-152.

dissertation, we focus on LPBF process which is used for a variety of metallic materials such as steel [3-5], titanium alloys [6, 7], aluminum alloys [8, 9] and nickel alloys [10, 11] as well as for some metallic glasses [12, 13], and metal matrix composites (MMC) [14, 15]. A schematic illustration of the LPBF technique along with the observed physical mechanisms are demonstrated in Fig 1.1.

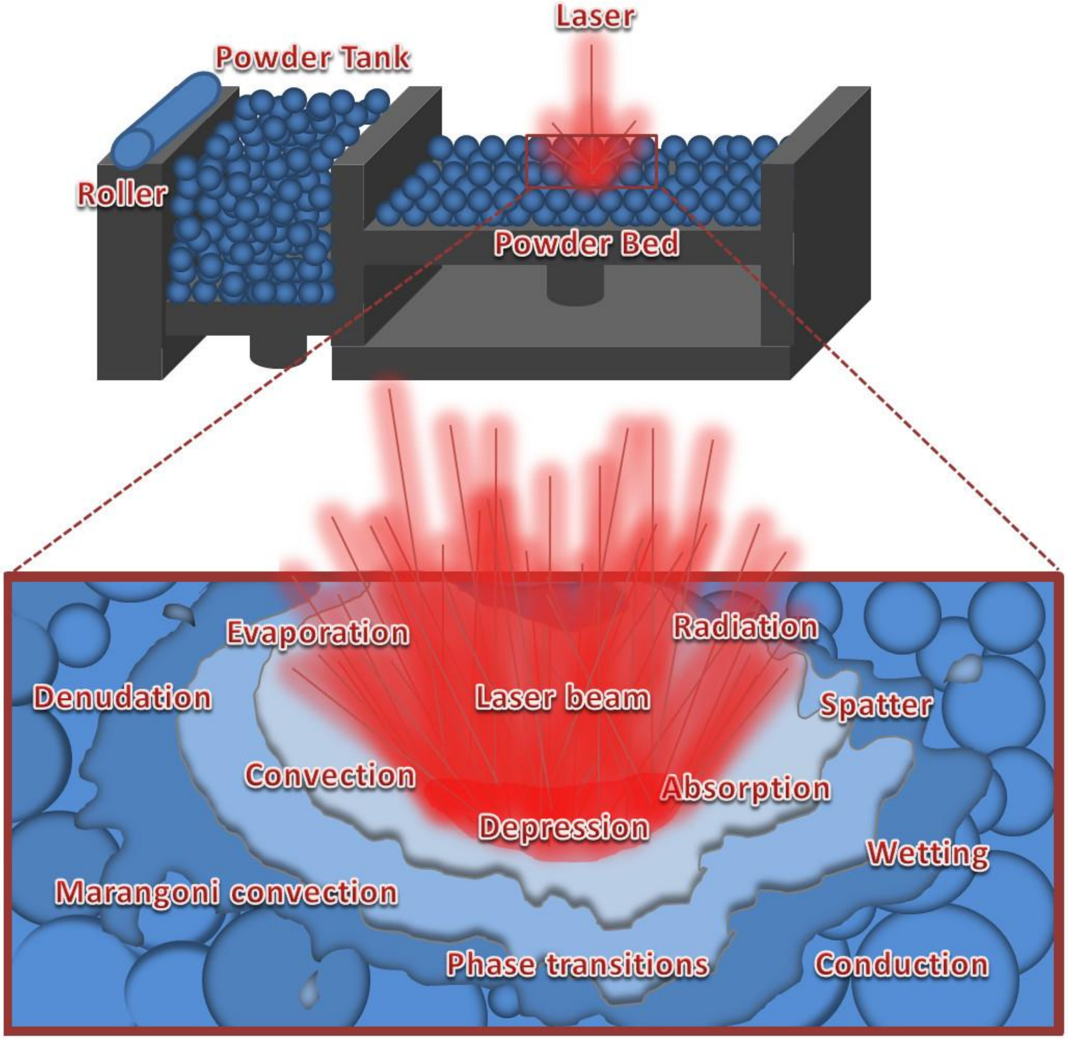

**Figure 1.1:** Principles of powder bed fusion (PBF) process (top) and dominant physical mechanisms during melting (bottom) [16]

In a typical LPBF process, metallic powders are spread as a thin layer and selectively melted by a laser beam. Then, the platform is lowered and the process is repeated for the next layer until the end-part is produced. In addition to well- known capabilities such as design freedom, material saving through design optimization, and flexibility, it also offers the capability to produce monolithic structures with spatially-tailored properties [17]. This feature could be the most valuable in applications where location- or time-specific properties in the part are needed.

Despite the promise of LPBF, there are several challenges to overcome in order to realize its full potential as a disruptive manufacturing technology suitable for industrial application. Mechanical defects such as porosity, residual stress, surface roughness, and internal cracks are common problems influencing the performance of the fabricated parts [18]. The process parameters such as laser beam power, scanning speed, powder layer thickness, hatch distance and the scanning path must be chosen carefully to minimize these defects to improve the mechanical properties. Another and a more serious concern regarding LPBF is the variability in the microstructure and consequently part performance. It is reported that LPBF-fabricated parts can exhibit to a large extent of in-sample and sample-to-sample variabilities [19]. These defects and variabilities are associated with the complex physical phenomena occurring during process, which lead to complicated thermal histories with high temperature gradients and cooling rates, as well as very rapid solidification. Studies on investigating the mechanical problems in LPBF parts can be found in the literature [20]. In this dissertation, we focus on the latter problem. The high variability in the microstructure and properties is considered the major obstacle against the widespread adoption of LPBF as a viable manufacturing technique. Quantifying and reducing variability in LPBF parts is a vital requirement for the part certification. Therefore, further researches are needed on LPBF processes.

In this regard, first the thermal history of the part must be well understood and controlled since it is the key factor affecting the variability. Once the thermal history is predicted as a function of process parameters, it should be then correlated to the microstructure and finally to properties for addressing the variability.

One possible direction to understand the thermal history is through directly capturing it experimentally during fabrication. Thermocouples (TC) can be used to measure the temperature at multiple locations in the part. However, the accuracy of the measurements can be affected by extremely high temperatures and steep gradients at locations near melt pool. It is almost impossible to measure the temperature within the melt pool due to the very high temperatures (above 3000 K) observed in this region, which is much higher than the operating temperature range of commercially available thermocouples. A typical temperature range that can be measured is 273.15 K to 2588 K by using a type-C thermocouple, which is well suited for high temperatures [21]. Another possibility for in situ temperature measurement is the use of contactless techniques. This involves multiple challenges associated with temperature measurement during LPBF process that involves a fast-moving laser beam, a micro-scale laser/powder interface, and the difficulty of implementing contactless temperature measurement techniques (commonly known as pyrometry). In addition, it is not possible to get the thermal history of the entire part using this method. Only the surface temperatures can be measured. A number of review papers [22, 23] provide a summary of the research efforts on experimentally capturing the thermal history in metal-based AM processes.

Regarding the experimental measurement of the microstructure, which is mostly an expensive and time-consuming method, some other challenges emerge. Characterization of the microstructural variabilities require different techniques. In addition, it is very difficult to define quantifiable metrics to investigate the effect of process parameters in microstructure. Although there are some studies on building statistical databases to analyze the mechanical properties in AM parts [24], these approaches are highly dependent on the material composition, and the type of AM process. A small change in such factors can lead to a big difference in the data.

Numerical-based modeling and simulation methods, on the other hand, are useful complements to investigate the variation in thermal history, in turn microstructure in LPBF parts. Over the past two decades, a significant number of Finite Element (FE) models have been developed to simulate the thermal history in LPBF processes [25, 26]. The FE method has been shown to be a versatile and accurate numerical method for solving engineering problems (e.g., heat transfer, solid mechanics, fluid dynamics) even for complex geometries and irregular meshes [27]. For the microstructure simulations, phase field (PF) modeling is one of the most popular techniques with the ability of predicting complex microstructural evolutions (e.g. solidification [28-30], solid-state phase transformations [31, 32], spinodal decomposition [33, 34], grain growth) without needing to track the interface. It has been implemented in number of researches to investigate the solidification microstructure of LPBF parts [35-37]

In this study, we developed a multi-scale multi-physics modeling framework coupling an FE-based thermal model to a PF-based microstructure model to investigate the rapid solidification microstructure during LPBF. Since the predicted microstructure is highly influenced by the thermal input, it is essential to have an accurate thermal model, which can be enabled with a rigorous verification and validation assessment. Therefore, the Section 2 and Section 3 of this dissertation are dedicated to the development of an accurate thermal model through various methods including code-to-code verification and experimental validation. Once the thermal history is predicted in the thermal model, it is then introduced into the PF model to predict the rapid solidification, particularly, cellular structure and Nb segregation in Section 4. The materials used in this work include Ti-6Al-4V, NiTi-SMA (Shape Memory Alloy) and NiNb binary alloy.

This study would contribute to the understanding and quantifying of microstructural variabilities as a function of process parameters, which can further be used to optimize and control the mechanical properties of LPBF parts, hence help in the part certification process.

This dissertation is organized as follows: Section 2 describes the details of developed thermal model and presents the prediction of multi-track thermal histories, the heating-cooling rates, the size of the heat affected zone (HAZ) and the melt pool during LPBF. The validation of the melt pool/HAZ size and thermal history through various experimental techniques (scanning electron microscopy (SEM) and pyrometry) is presented. The effects of selected model parameters on the predicted thermal history and predicted melt pool/HAZ size and geometry are discussed. Section 3 presents a thorough

Verification and Validation Assessment on the developed thermal model. The influence of meshing (mesh size and type), error tolerance and simulation domain size on the accuracy and computational cost of finite element-based thermal model is discussed. Section 4 presents a coupled thermal-microstructure model to predict the rapid solidification microstructure (e.g. the morphology, size, and Nb segregation) under LPBF conditions. To reveal the effect of process parameters on the microstructure variabilities, first, a conventional solidification microstructure map expressing the rapid solidification microstructure as a function of G and R is developed. Next, the microstructure predictions in multiple regions across the melt pool for sets of P and V are shown and compared with the experimental measurements for validation purposes. Finally, Section 5 summarizes this research and addresses the future directions.

# 2. NUMERICAL AND EXPERIMENTAL ANALYSIS OF HEAT DISTRIBUTION IN THE LASER POWDER BED FUSION OF TI-6AL-4V *

## 2.1 Overview

Laser powder bed fusion (LPBF) of metallic parts is a complex process involving simultaneous interplay between several physical mechanisms such as solidification, heat transfer (convection, conduction, radiation, etc.), and fluid flow. In the present work, a three-dimensional finite element (FE) model is developed for studying the thermal behavior during LPBF of Ti-6Al-4V alloy. Two phase transitions are considered in the model: solid-to-liquid and liquid-to-gas. It is demonstrated that metal evaporation has a notable effect on the thermal history evolution during fabrication and should not be overlooked in contrast to the majority of previous research efforts on modeling and simulation of additive manufacturing processes. The model is validated through experimental measurements of different features including the size and morphology of the heat affected zone (HAZ), melt pool size, thermal history. Reasonable agreement with experimental measurements of the HAZ width and depth are obtained with corresponding errors of 3.2% and 10.8%. Qualitative agreement with experimental measurements of the multi-track thermal history is also obtained, with some discrepancies whose sources are track thermal history using dual-wavelength pyrometry, as opposed to single track experi-

---

* Reprinted with permission from Karayagiz, K., et al., *Numerical and experimental analysis of heat distribution in the laser powder bed fusion of Ti-6Al-4V*. IISE Transactions, 2019. **51**(2): p. 136-152.

ments. The effects of selected model parameters and evaporation on the melt pool/HAZ size, geometry and peak predicted temperature during processing, and their sensitivities to these parameters are also discussed. Sensitivity analysis reveals that thermal conductivity of the liquid phase, porosity level of the powder bed, and absorptivity have direct influence on the model predictions, with the influence of the thermal conductivity of the liquid phase being most significant.

## 2.2 Introduction

Laser powder bed fusion (LPBF) additive manufacturing (AM) processes produce physical objects directly from a digital CAD model by selectively fusing metallic powder in successive layers using a laser beam. In addition to well- known capabilities such as design freedom, material savings through design optimization, and flexibility, it also offers the capability to produce monolithic structures with spatially-tailored properties [17]. This feature could be very valuable in applications where location- or time-specific properties in the part are needed.

Despite the promise of LPBF, there are several challenges to overcome in order to realize its full potential as a disruptive manufacturing technology suitable for industrial applications. Although extensive research efforts have been conducted to study the fundamental physical phenomena associated with complex LPBF processes (e.g., heat conduction, heat radiation, absorption or reflection, phase transitions, melt pool dynamics, Marangoni convection, evaporation, gravity, wetting, sintering), many of these phenomena, and their interactions, are not yet fully understood [38]. It is important to develop a more thorough understanding of these physical phenomena since they represent the key drivers of the thermal history during part fabrication which, in turn, plays an important role in the parts' properties. First, the high temperature gradients and cooling rates that occur during LPBF are likely to result in defects such as porosity, residual stress, surface roughness, and internal cracks; hence influencing the performance of the fabricated parts [18]. Second, variations in the thermal history drive changes in the microstructure and consequently part performance. Moreover, there is potentially high rewarding opportunity that upon the prediction, and subsequent control, of the thermal history, design and fabrication of parts with tailored properties through adjusting LPBF processing parameters (e.g., laser power, scanning speed, laser beam diameter, hatch distance) are possible.

One possible direction to understand the thermal history is through directly capturing it experimentally during fabrication. This involves multiple challenges associated with temperature measurement during the LPBF process that involves a fast-moving laser beam, a micro-scale laser/powder interface, and the difficulty of implementing contactless temperature measurement techniques (commonly known as pyrometry). A number of review papers [22, 23] provide a summary of the research efforts on experimentally capturing the thermal history in metal-based AM processes.

Numerical-based modeling and simulation methods, on the other hand, are a useful complement for understanding the thermal history in metal-based AM processes. The Finite Element (FE) method has been shown to be a versatile and accurate numerical method for solving engineering problems (e.g., heat transfer, solid mechanics, fluid dynamics) even for complex geometries and irregular meshes [27]. Over the past two decades, a significant number of FE models have been developed to simulate various aspects of AM processes with particular emphasis on investigating the thermal history, melt pool geometry, and residual stresses [39-42]. Most existing validation efforts of FE models, however, have either focused on comparing the predicted melt pool size and geometry with experimental measurements, or the thermal history in the case of single track deposits [25, 26, 39, 42, 43] without considering the role of subsequent passes of the laser beam. Although some experimental validation of multi-track thermal histories using thermocouples is available in the literature [44-46], the results are approximate since the thermocouples are positioned far away from the melt pool. In addition, most of the existing FE models developed for AM have typically ignored cooling effects due to evaporation [47, 48], which has a negative impact on the accuracy of predicting the melt pool temperature.

In the present work we provide efforts to fill in the gaps noted above through developing a three-dimensional FE model for investigating the thermal history during LPBF using Comsol Multiphysics®. The proposed model accounts for several heat transfer phenomena including conduction, convection, radiation, phase transitions, and evaporation (which has commonly been overlooked in the AM modeling and simulation literature as stated previously). The FE model is then used to predict the thermal history in multi-track builds, the heating-cooling rates, and the size of the heat affected zone (HAZ) and the melt pool during LPBF of Ti-6Al-4V. Experimental validation of the melt pool/HAZ size and the multi-tracks thermal history was performed by combining multiple experimental techniques including scanning electron microscopy (SEM) and contactless thermal measurements using pyrometry. The effects of selected model parameters as well as the influence of evaporation on the predicted thermal history and predicted melt pool/HAZ size and geometry are discussed.

The paper is organized as follows: Section 2.3 presents an overview of the work on powder-bed fusion modelling. Next, the developed model is described in Section 2.4, which introduces the physics of the process, the assumptions made and the modeling steps. Section 2.5 explains the experimental testbed and details for the formal validation of the model. Results from simulations, experiments and validations are reported in Section 2.6. The paper finalizes with Section 2.7 listing a summary and conclusions of the present work.

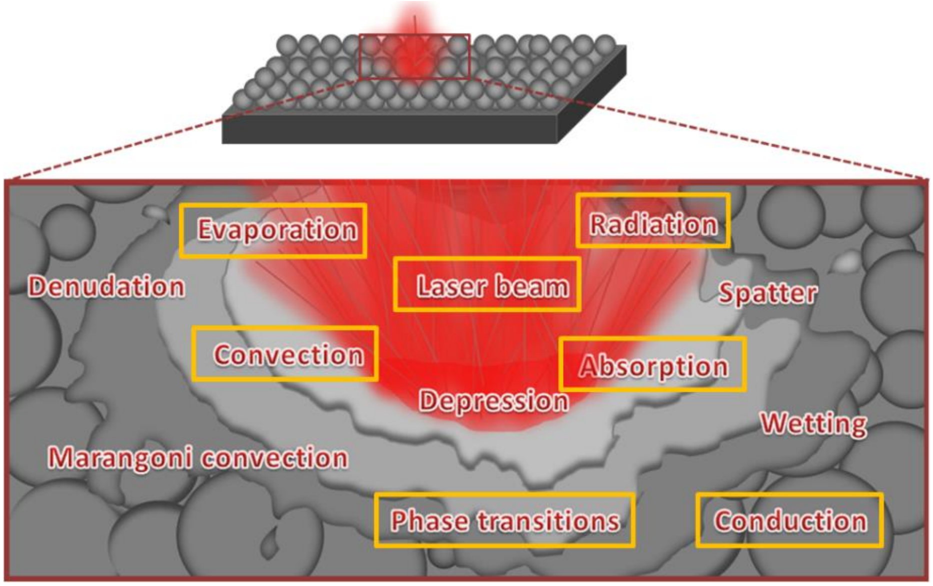

**Figure 2.1:** Physical mechanisms during Laser powder bed fusion (LPBF). Physical mechanisms considered in the present work are highlighted in yellow rectangles.

## 2.3 Literature Review

### 2.3.1 Powder Bed Modeling

There are two different approaches in modeling powder bed fusion AM processes: powder-scale and continuum-scale approaches. While the former directly accounts for the geometry, size and distribution of the powder particles, the latter is based on the assumption of a continuum layer with effective thermo-physical properties. Although the powder-scale modeling approach (e.g., [25, 49-53]) is more realistic in simulating the process, and offers higher accuracy on a micro-scale level, it is computationally expensive to an extent that can severely hinder its usability in simulating full-part fabrication. Therefore, the continuum-scale modeling approach has been widely adopted in the literature [26, 39-41, 43, 47, 48, 54-81] and in this study due to its relative ease of implementation and low computational cost compared to powder-scale modeling.

### 2.3.2 Physical Mechanisms during LPBF

Physical mechanisms that take place during LPBF are demonstrated in Figure 2.1. Accounting for all these mechanisms in a single model prohibitively increases the computational cost; hence some of these mechanisms were overlooked in a large number of works in the literature. The role of these mechanisms on the thermal history is briefly described next.

#### 2.3.2.1 Heat Transfer

Conduction plays the major role in transporting the heat applied by the laser beam to the powder particles and the substrate. In a typical thermal FE model, the transient

(Fourier's) heat conduction equation is solved using suitable initial and boundary conditions. The simplest form of the heat equation considering applied heat input to the system is given by

$$\rho C_p \frac{\partial T}{\partial t} + \nabla(-k\nabla T) = Q \tag{1}$$

where $T$ is the temperature in Kelvin, $t$ is the time, $\rho$ is the density of the material, $C_p$ is the specific heat capacity, $k$ is the thermal conductivity and $Q$ is a heat source. While this equation has been adopted in various studies [54, 60, 82-85], a variant of this equation has also been utilized in a significant number of studies [48, 52, 58, 78, 86-89] to account for the latent heat of fusion/evaporation that is important for an accurate prediction of the distribution of the energy in the system.

During LPBF and other AM processes, a portion of the heat applied to the system is lost through radiation, convection and evaporation on the surface. Therefore, incorporating these effects into the model is important to achieve accurate energy balance. Radiation is usually applied as a boundary condition on the surface [25, 40, 59], but it is worth noting that a number of works in the literature have neglected radiation claiming that the melt pool size is very small compared to the entire simulation domain; hence the effect of radiation can be assumed negligible [26, 39, 69].

Convection of heat between the powder surface and the surrounding gas has been taken into consideration in most LPBF studies [26, 61, 66], although it has been ignored in other works due to its insignificant effect on the heat loss [69, 71].

Evaporation takes place when the boiling temperature of the material is exceeded. It is an important phenomenon which should be taken into account especially at moderate or high beam powers, and low scanning speeds. During LPBF, evaporating material is removed through circulating flow of inert gas (Nitrogen or Argon) in the build chamber, resulting in heat and mass loss in the powder bed. It was demonstrated in [25] that the mass loss due to evaporation is negligible (much less than the mass of a powder particle). However, consideration of heat loss in the simulation is important in order to accurately predict the thermal history during the process. Neglecting evaporation results in the accumulation of heat which leads to an over estimation of the predicted temperature of the molten material. Since taking evaporation into account in the numerical models poses additional computational burden, most of the works in the literature have neglected it [26, 47, 69]. While this might not be problematic in processes with low energy input, for those with high energy input, it can lead to an increase in the predicted temperature of the melt pool above the boiling point which is unrealistic.

Several approaches are available to account for evaporation. One approach considers the Argon gas environment, vapor pressure and fluid dynamics along with the heat transfer [25, 43, 51, 90, 91]. However, this approach is more complex and computationally expensive compared to a conventional heat transfer model. Loh et al. [71] simulated the cooling effect of evaporation by artificially increasing the thermal conductivity of the vapor phase along the z direction. In our earlier FE model, we have implemented this simple approach which reduced the overestimated melt pool temperature (6300 K) to around 3650 K. However, the temperature was still much higher than the boiling temperature of the material (3315 K) and the predicted melt pool sizes were extremely large. Refer to Figure 2.A1 and A2 in the Appendix, for a comparison of the results from the two methods suggested by Loh et al. [71] and proposed in this study. In various simulations, it soon became obvious that this method is less effective for high beam powers and low scan speeds and leading to unrealistic large melt pool sizes. In the present study, the evaporation was accounted for by employing a new, simple and efficient method, which will be explained in detail in the following sections.

#### 2.3.2.2 Fluid Flow

One may also consider the convective effects — i.e. the Marangoni effect — due to the fluid flow of the material inside the melt pool. Marangoni convection is caused by the surface tension gradient — resulting from thermal gradients — in the free melt surface. It has been ignored in the vast majority of the modeling studies [41, 59, 62, 74] due to the relatively small size of the melt pool compared to the entire system [40]. Inclusion of fluid dynamics in the model is necessary to account for these effects. Jamshidinia et al. [40] and Yuan and Gu [76] developed numerical models which accounted for both fluid dynamics and heat transfer, and investigated the effect of Marangoni convection on the melt pool size. Their results demonstrated that by considering these effects a larger melt pool width and a shallower melt pool depth along with an extended surface with high temperatures were obtained. In another study [25], complex physics of melt flow were investigated and the effect of Marangoni convection on the formation of depression, denudation, the formation of spatters, pores, and incomplete melting were discussed. Recent works have begun to account for fluid dynamics effects [53, 91, 92].

Alternatively, Liu et al. [93], Taylor et al. [94], and De and DebRoy [95] proposed a simpler approach to account for the convection in the melt pool without the need for a fluid flow model. This method suggests using an effective thermal conductivity for the molten material, by simply increasing it above the melting point. This method has been employed in some studies [39, 62, 79] and the predictions were in reasonable agreement with the experiments.

In contrast to previous literature studies, in our proposed FE model we consider all the aforementioned heat transfer mechanisms including radiation, convection and evaporation, while the fluid flow was neglected for simplification. With regards to Marangoni convection, it is worth noting that the simple method proposed in [93-95] was employed to investigate its effect on the melt pool. For the sake of completeness, we have accounted for both convective and radiative heat transfer despite their low influence on model predictions, since trial simulations revealed that the additional computational cost is negligible (on the order of a few extra minutes).

### 2.3.3 Material Properties

Incorporating temperature-dependent material properties, especially thermal conductivity, specific heat capacity, and density in the simulations is essential to accurately predict the thermal history of the specific materials parts during an LPBF process. Numerous studies have considered temperature dependent properties [26, 39, 41, 43, 62, 71, 73, 74, 88], while a few others [54, 61, 87, 89] adopted constant thermo-physical properties.

The thermo-physical properties of the metal powder are notably different than those of the bulk material. Therefore, to account for this difference, it is required to utilize the effective thermo-physical properties in continuum-scale models. Sih and Barlow [96] developed a model to predict the effective thermal conductivity of the powder layer as a function of several physical parameters (i.e., thermal conductivity of the bulk material, thermal conductivity of the ambient gas, porosity of the powder bed, diameter of the powder particle, temperature of the powder bed), which has been employed in a variety of LPBF studies [45, 57, 60, 65]. Some simpler models, based on only the porosity and the thermal conductivity of bulk material, are also available and have been used in various investigations [26, 58, 66, 69, 71]. Effective density for the powder bed has been considered in some studies [26, 69, 71] while number of others have employed the density of the bulk material for the powder bed [39, 41, 62, 74]. On the other hand, the vast majority of the studies have assumed that the specific heat capacity and latent heat of fusion of the bulk material can be used for the powder [39, 43, 47, 69, 71, 74, 97].

Sih and Barlow also developed a model to predict the emissivity of the powder bed as a function of the emissivity of the bulk material and the porosity [96]. The results demonstrated that powder layer has a higher emissivity than that of the bulk. The model was experimentally validated and has been subsequently employed in the literature [45, 62]. A temperature dependent emissivity value has been utilized in other studies [74, 98, 99]. In this work, however, we noticed that emissivity changes have minimal influence on the radiative heat loss and we thus decided to employ a constant emissivity value, similar to values proposed in several recent works [39, 40, 71].

When a laser beam is applied onto the powder bed, only a portion of the deposited energy is absorbed by the material. Experimental measurement of absorptivity is difficult since it depends on several factors such as beam intensity, wavelength, oxidation, polarization, temperature, material properties (density, size, distribution, porosity). Yang et al. [99] developed an indirect model to calculate the absorptivity of Ti-6Al-4V plate during laser assisted machining. The results demonstrated that the absorptivity of the solid Ti-6Al-4V was between 0.28 and 0.41 in the temperature range of 500-1400$^{o}$C. Gusarov and Smurov [100] developed another model to calculate the absorptivity of optically thick powder layer of different materials as a function of porosity level and powder diameter. The calculations showed a much higher absorptivity for the powder layer (i.e. 0.77 for Ti) compared to the bulk material (i.e. 0.38 for Ti). Boley et al. [101], on the other hand, calculated the absorptivity of metallic powder spheres and flat surfaces of different materials (i.e. 0.64 for Ti). This model was experimentally validated by Rubenchik et al. [102] and close agreement with the predicted values were obtained (i.e. 0.7 for Ti-6Al-4V).

In the light of the aforementioned information in the previous paragraphs, temperature dependent material properties for thermal conductivity, density and heat capacity were taken into consideration in the present model, while constant values for the emissivity and absorptivity were found sufficient. Effective thermo-physical properties for the powder bed were also considered.

### 2.3.4 Heat Source Modeling

A proper treatment of the heat source is of paramount importance for an accurate thermal simulation of LPBF. Rosenthal [103] developed an analytical solution for a 1D moving point heat source (1D). Eagar and Tsai [104] presented a solution of Gaussian-distributed (2D) moving heat source and predicted the weld pool geometry for the first time. Goldak et al. [105] introduced a 3D double-ellipsoidal moving heat source, as a first approach for the 3D heat source, and developed a FE model to investigate the thermal history in a welding application. In the light of these prior studies, several 2D [41, 58, 106-108] and 3D [62, 109, 110] Gaussian distributed moving heat source models have been proposed and used in the thermal modeling of different powder bed-based AM processes. Note that, while some researchers [50, 56, 74, 89, 110] argued that a 3D heat source is a more accurate method of modeling the beam heating [110], a majority of the LPBF/Selective Laser Sintering (SLS) studies [43, 47, 48, 60, 69, 71, 78] used a 2D heat source to simplify the models. Another type of heat source model known as the Ray Tracing (RC) model, was formulated by Wang et al. [111] and has been adopted in a few recent studies [25, 26]. However, an accurate modeling of the laser beam through the RC model and the 3D heat source model require a reasonable estimation of the penetration depth which is in turn influenced by various factors (material type, powder size and geometry), and a precise estimation of the penetration depth is troublesome; hence the amount of such investigations is limited [87, 111-113].

As stated in the previous paragraph, a 2D heat source is found to be sufficient to model the laser beam and preferred in the majority of the LPBF studies for the simplification purposes. Due to these reasons, a 2D heat source was adopted in the present work.

### 2.3.5 Volume Shrinkage and Layer Built-up

During melting of the powder, the porosity gradually decreases resulting in a shrinkage in the volume of the powder layer. This phenomenon has been considered in various models [48, 71, 114]. It has been found that while the depth of the melt pool is slightly larger, the width and length of the melt pool are smaller, in addition to lower maximum temperature in the melt pool, when volume shrinkage is considered [48].

In terms of layer built-up simulations, Roberts et al. [58] investigated the thermal history along several layers by employing "element birth and death" method. Van Belle et al. [115] presented a numerical model based on this method to study the thermal distribution, residual stress, and the effect of annealing temperature on the plastic strain of the material. Similarly, Fu and Guo [47] employed "activated-deactivated" elements method to study the thermal history and melt pool geometry in a multi-layer LPBF process. Number of review papers regarding numerical modeling of AM processes are available for more information [2, 16, 116].

For simplification purposes and considering the small thickness of the powder layer (30 μm), volume shrinkage caused by melting of the powder was assumed to be negligible in the present study. Similarly, layer built-up was not taken into account in this work, due to the additional computational burden.

### 2.3.6 Thermal Distribution Analysis in Metal Based AM Process

A variety of literature works investigating the thermal distribution in metal-based AM process is available. Kolossov et al. [55] developed a three-dimensional thermal model for the SLS process and validated it experimentally using an infrared camera. The importance of using a temperature-dependent thermal conductivity in the model was demonstrated. The results indicated that a model with a constant thermal conductivity is not sufficient to accurately reproduce the real thermal distribution. Li et al. [57] developed a thermal model for Laser Powder Bed Fusion (LPBF) of 316L-stainless steel accounting for the temperature-dependent material parameters, effective powder properties and powder to liquid phase transformations to investigate the effect of various process parameters (e.g. beam power, scan speed, hatch distance) on the thermal distribution. Roberts et al. [58] built a finite element thermal model for simulating the AM of Ti-6Al-4V powder. The authors modelled the addition of new powder layers based on the element birth and death method. Verhaeghe et al. [59] developed a model considering the enthalpy formulation and volume shrinkage to study the LPBF process and investigated the effect of evaporation on the predicted temperature and melt pool size. It was demonstrated that a better agreement with experimental measurements are obtained when evaporation is taken into consideration in the model. Vasquez et al. [90] conducted a multi-physics simulation of laser powder deposition considering heat transfer, thermo-capillary forces and their influence on fluid flow. The effect of process parameters, evaporation and surface tension on the melt pool were investigated. Jamshidina et al. [40] developed a thermal-fluid flow model for Electron Beam Melting (EBM) of Ti-6Al-4V and investigated the influence of fluid convection in thermal distribution and melt pool geometry. The results indicated that a larger melt pool width and a shallower melt pool depth along with an extended surface with high temperatures are obtained when fluid convection is accounted for in the model. Khairallah et al. [25] developed a powder-scale model for laser powder bed fusion AM process and investigated various fluid flow dynamics in the molten region (e.g. the effect of Marangoni convection, recoil pressure, pore defects, denudation zones, spattering).

## 2.4 Model Description

Numerical simulation of the thermal history during LPBF was implemented in Comsol Multiphysics®. A three-dimensional model consisting of a thin layer of powder and a thick substrate with the dimensions of 6.5x2.5x0.03 $mm^3$ and 6.5x2.5x1 $mm^3$, respectively, is shown in Figure 2.2 (a). The laser beam was simulated to move between the points x = 1.25 mm and x = 4.25 mm along the x-axis on the top surface (Figure 2.2 (b)), melting 3 parallel tracks of length 4 mm. The spacing between the tracks (hatch distance) was set to 70 μm. This scanning strategy is illustrated in Figure 2.2 (b). Ti-6Al-4V alloy was selected as the material for both the powder bed and the substrate.

The high temperature gradients in the laser-powder interaction zones necessitate the use of a finer mesh in these regions to ensure accurate analysis. To account for both accuracy and computational burden, convergence experiments with different mesh sizes were performed. As a result, a mapped mesh of 25 μm was found to be suitable for the laser scanned region, while a coarser mapped mesh was employed for further areas. The meshing strategy is represented in Figure 2.2 (a).

The following assumptions and other model details are consistent with what has been discussed in Section 2.3.

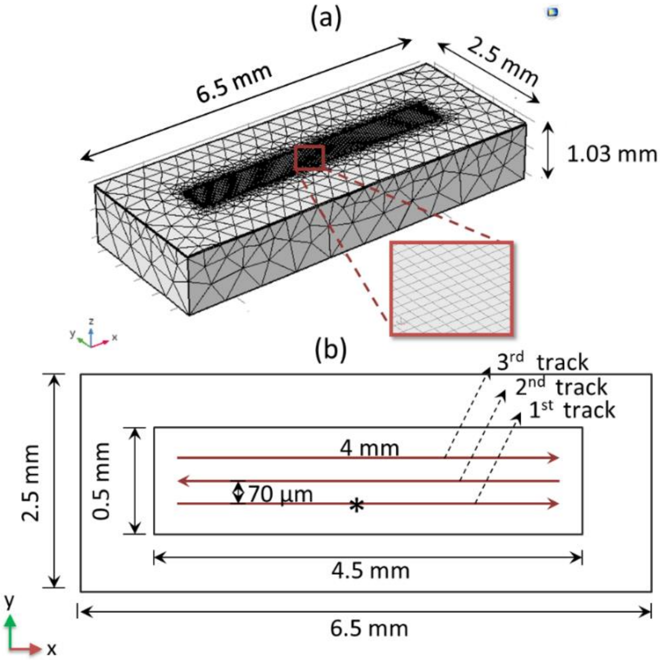

**Figure 2.2:** 3-dimensional model and meshing geometry (a), and the scanning strategy during LPBF simulations (b). The Asterisk represents the position of the selected point at which temperature is calculated during simulation.

### 2.4.1 Assumptions

The powder layer was assumed as a continuum medium with an initial porosity of 0.35. For simplification purposes and considering the small thickness of the powder layer (30 µm), volume shrinkage caused by melting of the powder was assumed to be negligible. A constant value for the absorptivity of the powder layer was assumed. Fluid dynamics effects in the molten metal were neglected.

### 2.4.2 Physical Description of the Model

To simulate phase transitions during LPBF, namely solid-to-liquid and liquid-to-gas transitions, the “heat transfer with phase change” feature of Comsol Multiphysics® was utilized. The heat equation represented in equation (1) was used while the latent heat was also considered as presented in equation (4) and (5) below. The values of the thermo-physical properties during phase transitions are described by the following equations:

$$\rho = \sum_{i=1}^{N} \theta_i \rho_i \tag{2}$$

$$k = \sum_{i=1}^{N} \theta_i k_i \tag{3}$$

$$C_p = \frac{1}{\rho}\left(\sum_{i=1}^{N} \theta_i \rho_i C_{p,i}\right) + \sum_{j=1}^{N-1} L_{j\to j+1} \frac{d\alpha_{m,j\to j+1}}{dT} \tag{4}$$

$$\alpha_{m,j\to j+1} = \frac{1}{2}\frac{\theta_{j+1}\rho_{j+1} - \theta_j \rho_j}{\theta_{j+1}\rho_{j+1} + \theta_j \rho_j} \tag{5}$$

where $\theta_i$ is the volume fraction of phase i before the transition (which smoothly changes from 1 to 0 during the transition), while $\rho_i$, $k_i$ and $C_{p,i}$ are the density, conductivity and heat capacity of phase i, respectively. In this case, N (the number of phases) was set to 3 to account for the solid (i=1), liquid (i=2) and vapor (i=3) phases present. $L_{j\to j+1}$ stands for the latent heat of fusion ($L_f$) or the latent heat of evaporation ($L_v$) depending on the type of phase transition. The function $\alpha_{m,j\to j+1}$ is used to describe the mass fraction of the phase after transition.

During LPBF, the powder porosity Ø gradually decreases and reaches Ø = 0 when the powder is fully melted. The process is modeled as follows:

$$\emptyset = \begin{cases} \emptyset_{0,} & T_0 < T < T_s \\ \dfrac{\emptyset_0}{T_s - T_m}(T - T_m), & T_s < T < T_m \\ 0, & T > T_m \end{cases} \tag{6}$$

where $\emptyset_0$, $T_m$, $T_s$ are initial powder porosity, melting temperature and sintering temperature, respectively.

Since the powder bed was assumed to be a continuum medium, it is important to utilize the effective thermo-physical properties for the powder material. The effective density $\rho_{eff}$ and effective thermal conductivity $k_{eff}$ of the powder bed are defined as [97]:

$$\rho_{eff} = \rho_{solid}(1 - \emptyset) \tag{7}$$

$$k_{eff} = k_{solid}(1 - \emptyset)^n \tag{8}$$

where $\emptyset$ is the porosity function described in equation (6), $\rho_{solid}$ is the density of the bulk solid; $\rho_{eff}$ is the density of the powder, $k_{solid}$ is the thermal conductivity of the bulk solid; $k_{eff}$ is the thermal conductivity of the powder, and $n$ is an empirical parameter which was selected as 4 according to Yin et al. [97]. Note that, the heat capacity for the powder material was assumed the same as that of the bulk solid which was the case in the majority of the literature.

It is also worth mentioning that, initially, effective thermo-physical properties are assigned in the powder layer. However, once the molten powder solidifies the thermo-physical properties of the bulk solid must be assigned. Therefore, a variable accounting for the different forms of solid phases (0: powder, 1: bulk) was introduced and a change criterion (i.e., $T > T_m$ ) was applied. When the criterion is satisfied, the type of the solid phase is fixed to 1 to prevent the solidified material from taking the powder properties.

### 2.4.3 Initial and Boundary Conditions

The initial temperature of the entire build was set to the ambient temperature expressed as:

$$T\,(x, y, z, t)_{t=0} = T_0 \tag{9}$$

where $T_0$ is the ambient temperature (298 K in the present study).

The temperature on the boundary surfaces, except the top surface, was maintained at the ambient temperature during the simulation. Both natural convection and radiation were applied on the top surface as the boundary conditions. These conditions can be expressed as:

$$q_{convection} = h(T_{amb} - T) \tag{10}$$

$$q_{radiation} = \varepsilon\sigma_B(T_{amb}^4 - T^4) \tag{11}$$

where h, $T_{amb}$, T, ε and $\sigma_B$ are the convective heat transfer coefficient, ambient temperature, current temperature, surface emissivity and Stefan–Boltzmann constant, respectively. The surface emissivity was set to 0.7 according to [99].

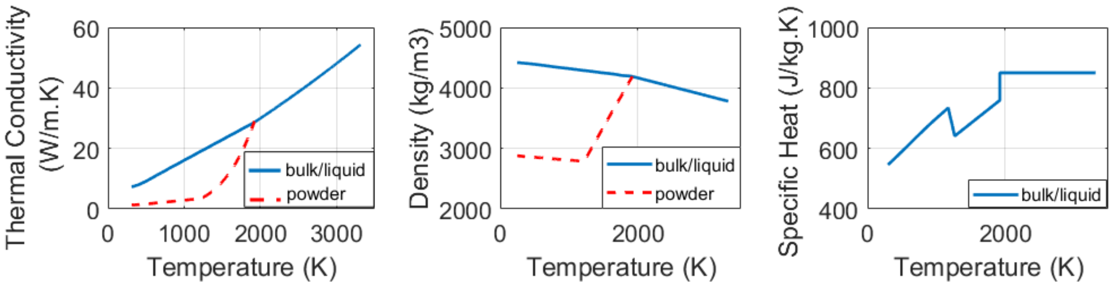

**Figure 2.3**: Thermo-physical properties of Ti-6Al-4V (solid properties are reported in [69], liquid properties are extrapolated according to [23], powder properties are calculated based on equations 7 and 8)

### 2.4.4 Moving Heat Source

The laser beam was defined as a moving surface heat source with a Gaussian distribution and modeled using the Deposited Beam Power feature of Comsol Multiphysics®. The laser beam power and speed were set at 50 W and 80 mm/s, respectively, for the purpose of experimental validation, and a constant absorptivity of 0.7 [102] was used in this model. The heat source with Gaussian distribution can be defined as:

$$Q_{\text{source}} = \frac{PA}{2\pi\sigma^2} e^{\left(-\frac{d^2}{2\sigma^2}\right)} \tag{12}$$

where P is the beam power, A is the absorptivity, σ is the standard deviation (i.e. $\sigma = \frac{1}{4}D$ where D is the beam diameter). Here, d is the radial distance from the center of the beam which is calculated based on the beam origin point and the beam orientation.

**Table 2.1.** Materials and process parameters used in the simulations

| Parameters | Values |
|---|---|
| Boiling temperature, $T_v$ (K) | 3315 [117] |
| Liquidus temperature, $T_m$ (K) | 1923 [118] |
| Solidus temperature, $T_s$ (K) | 1878 [118] |
| Latent heat of fusion, $L_f$ (kJ/kg ) | 286 [118] |
| Latent heat of evaporation, $L_v$ (kJ/kg ) | 9830 [118] |
| Absorption coefficient, A | 0.7 [102] |
| Emissivity, ε | 0.7 [99] |
| Initial powder porosity, $\emptyset_0$ | 0.35 |
| Powder layer thickness, V (µm) | 30 |
| Laser beam diameter, D (µm) | 70 |
| Laser beam power, P (W) | 50 |
| Scanning speed, V (mm/s) | 80 |
| Hatch distance, $H_d$(µm) | 70 |

### 2.4.5 Material Properties

The temperature dependent material properties of Ti–6Al–4V are reported in [118] from room temperature up to melting point. This data was extrapolated according to [39] to obtain the temperature range of the liquid phase. The effective thermal conductivity

($k_{eff}$) and density of the powder ($\rho_{eff}$) were calculated based on equations 7 and 8, while the specific heat capacity of the powder was assumed to be the same as that of the solid as in the majority of the previous studies [39, 43, 47, 69, 71, 74, 97]. Due to the lack of data on the thermal conductivity, density and specific heat capacity of the Ti-6Al-4V vapor phase, their corresponding values were estimated based on the general knowledge of the thermo-physical properties of the gaseous materials. Figure 2.3 illustrates the thermo-physical parameters used in this study. The material and process parameters used in the simulations are listed in Table 2.1.

### 2.4.6 Evaporation

Initially, single track simulations were performed considering only powder, solid and liquid phases and assuming the applied energy density to be low. These simulations showed that the temperature in the molten region exceeded the boiling point indicating that the applied energy density was high enough to cause both melting and evaporation of the powder particles. However, the situation of a molten material with a temperature above the boiling point is not physical. Therefore, the vapor phase was defined in the system and evaporation was considered. In general, during evaporation, both mass and heat are lost from the system. However, Khairallah [25] demonstrated that the mass loss due to evaporation is negligible (much less than the mass of a powder particle), therefore it was neglected in our simulation and only heat loss through evaporation was considered to balance the energy.

Evaporation was achieved by employing a new physics-based approach, based on the implementation of a heat sink on the surface of the powder bed, which accounts for the heat loss from the evaporation of the material. The heat sink (at an arbitrary time step) is described as follows:

$$\mathrm{Q_{sink}} = -\,\dot{\mathrm{m}}_{\mathrm{v}} * \mathrm{L_v} \tag{13}$$

where $\dot{\mathrm{m}}_{\mathrm{v}}$ is the evaporative mass rate and $\mathrm{L_v}$ is the latent heat of evaporation. $\dot{\mathrm{m}}_{\mathrm{v}}$ is calculated based on the fraction of the vapor phase, $\theta_{\mathrm{v}}$, which is an internal variable in Comsol Multiphysics® updated at each time step as described in [119]. It is noteworthy to point out that the heat sink only removes energy from the elements with vapor phase. For instance, if $\theta_{\mathrm{v}} = 0$ for a specific element, there will be no heat loss due to evaporation such that, $\mathrm{Q_{sink}} = 0$.

Note that the proposed approach for the evaporation has been tested with different material systems (Ti-6Al-4V, Ni-Ti, 316L stainless steel) and process parameters (beam power, scanning speed, beam diameter) in order to demonstrate its robustness to different material systems and process conditions. A peak temperature around the boiling point was observed for each of these different conditions and the material systems indicating the adequacy of the method.

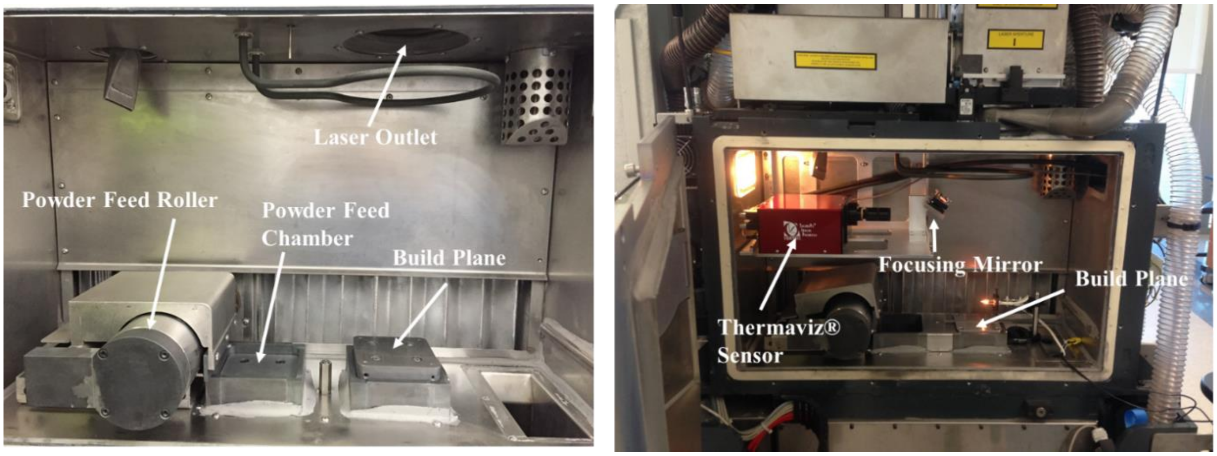

**Figure 2.4**: ProX 100 DMP build chamber before (a) and after (b) custom integrating the ThermaViz sensor

## 2.5 Experimental Details

### 2.5.1 Experimental Testbed

For this study, we employed a ProX 100 DMP commercial LPBF from 3D Systems. Figure 2.4 shows the ProX 100 DMP build chamber before (a) and after (b) custom integrating a pyrometer sensor. The laser source generates a beam with a Gaussian distribution, wavelength of $\lambda$=1070 nm, beam spot diameter of D=70 μm (measured according to 1/$e^2$ method), and maximum power of P=50 W. Additionally, ultra-high purity (UHP) Argon was used as an inert protective atmosphere during fabrication to prevent oxidation of the molten metal.

The raw material used was Ti-6Al-4V powder by LPW Technology Ltd., sieved down to a 45 μm mesh, and substrate plates made of Ti-6Al-4V were used.

The LPBF system was custom-instrumented with a thermal imaging sensor to monitor the temperature using high speed thermography during the fabrication. The sensor used is a ThermaViz® pyrometer developed by Stratonics Inc. This is a dual-wavelength pyrometer with CMOS imaging technology and provides a 1300x1000 pixel field of view (FOV) mapped to a 26 x 20 mm spatial resolution, yielding a 20 μm spatial resolution per pixel. The pyrometer captures frames at a rate of 100 Hz for the full FOV and can achieve up to 3 kHz frame rates for partial FOV. The sensor is calibrated for measurements in the 1273 K to 2773 K range, making it suitable for characterizing the thermal history during LPBF. It is important to point out that dual-wavelength pyrometry is a useful method to account for emissivity variations among different materials and material phases, since the temperature is computed as a function of the ratio of radiation at two different wavelengths.

### 2.5.2 Experimental Validation

The heat-affected zone (HAZ) predicted by the FE model, particularly, the depth into the solid substrate and width, as well as the thermal history at a selected location on the surface were compared with experimental measurements. The validation experiments were consistent with the simulation setup, previously defined in Section 2.4. Specifically, 4 mm-long single-track and three-track deposits were printed onto the solid substrate, while monitoring the process with the pyrometer. The laser parameters were set to a power of 50 W and scanning speed of 80 mm/s, on a 30 μm thick powder layer. Additionally, the hatch distance (i.e. distance between two adjacent passes of the laser beam within the same layer) for the three-track case was selected as 70 μm.

The single-track deposits were further used to measure the width and depth of the HAZ in the solid substrate. The Ti-6Al-4V substrate was initially in a two-phase (α+β) microstructure, but when heated above the β transus temperature of approximately 1255 K [120], the α phase is dissolved. Because the cooling rate in the LPBF process exceeds 10,000 K/s, parts of the β austenite phase transform to martensite phase upon removal of the laser source, creating a difference in the microstructure that can be detected using electron microscopy. In the present work, the cross sections of the single tracks were cut out using wire electrical discharge machining (EDM). The cross sections were then embedded in epoxy resin, mechanically polished, and imaged using a Tescan Fera-3 SEM using the backscattered electron (BSE) detector. This allows us to distinguish between the heat affected martensite and the original α+β two-phase microstructure of the substrate.

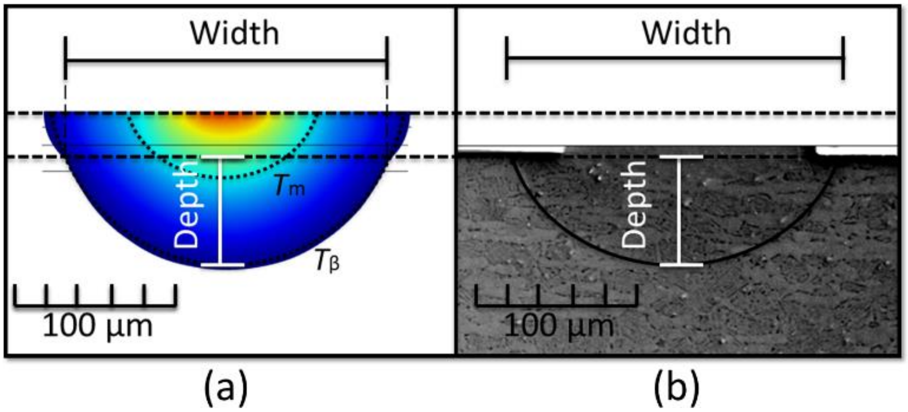

**Figure 2.5**: Comparison of HAZ size from the experiment (b) and simulation (a). The experimental HAZ width and depth in the substrate are measured in the range of 218±21 µm and 64.4±1.5 µm, respectively. The predicted HAZ width and depth in the substrate are 211 µm and 72 µm.

## 2.6 Results and Discussion

### 2.6.1 Simulation Results

This section discusses the simulation results obtained using the parameter settings listed in Table 2.1.

#### 2.6.1.1 HAZ Size

The HAZ refers to the region around the molten material whose microstructure is affected during fabrication. In LPBF, phase transformations in the HAZ take place due to high temperature gradients. Figure 2.5 demonstrates the predicted versus experimentally measured depth in the solid substrate and width of the HAZ. The β transus temperature was used to define the HAZ size in the predictions. Note that the predicted cooling rate at this region was already higher than the reported critical cooling rate [121] required for martensitic transformation to occur. The experimentally measured width and depth (in the solid substrate) of the HAZ were 218±21 μm and 64.4±1.5 μm, respectively, based on the average of 5 different single-track melting experiments. The predicted HAZ width and depth in the solid substrate were 211 μm and 72 μm, respectively, with corresponding prediction errors of 3.2% and 10.8%. The main source of the error in the HAZ size is believed to originate from neglecting martensitic transformation in the model. This mechanism will be needed to include in the future studies. On the other hand, considering higher prediction errors reported in previous models in the literature [39, 71, 92], we believe the error percentages obtained in the present work are reasonable.

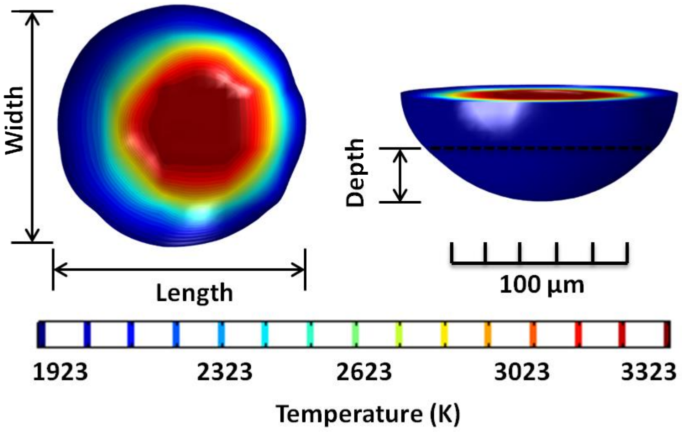

**Figure 2.6**: Melt pool size and geometry of Ti-6Al-4V alloy for the conditions provided in Table 2.1. The depth in the substrate, width and length of the melt pool are predicted as 22 μm, 144 μm, 149 μm, respectively.

### 2.6.1.2 Melt Pool Size

Figure 2.6 demonstrates the representative melt pool geometry composed of several isothermal contours with a minimum temperature of 1923 K corresponding to the melting temperature of Ti-6Al-4V.

It has been emphasized in the literature that the depth of the molten pool is one of the crucial factors to produce parts with high quality [122-124]. The depth of the molten pool needs to be large enough in order to effectively fuse the powder to the substrate or to the previously solidified layers. The predicted melt pool depth into the solid substrate at steady state was calculated as 22 μm for the aforementioned conditions, indicating that the applied energy density was sufficiently high such that melting of the substrate was achieved.

A "comet tail" profile that is observed in a number of studies [41, 47, 125] was not observed in the present simulation due to the relatively low maximum laser power provided by the ProX 100 DMP system. The width of the melt pool was experimentally measured as 170±13 μm from the BSE images, indicating 15% error relative to the predicted value of 144 μm. It is worth noting that the error percentage obtained in the present study is much lower than that of the similar studies in the literature [39, 71, 92]. It was not possible to distinguish the depth of the melt pool in the solid substrate from these images; hence a comparison of the measured and predicted melt pool depths could not be obtained. The main source of the error in the melt pool width is believed to originate from the neglect of Marangoni convection in our model. As already discussed, Marangoni convection leads to a larger melt pool width (and shallower melt pool depth). Other possible sources of discrepancy include the absorptivity and powder bed porosity levels used in the model. As discussed in the previous sections, these two parameters have direct influence on the accuracy of the model. Therefore, a sensitivity study was carried out to investigate the effect of these factors on the melt pool and thermal history in Section 2.6.2.

#### 2.6.1.3 Thermal History

The thermal history in the powder bed and the already solidified layers change rapidly with time. The largest temperature gradients are observed on the powder surface at the center of the laser beam and decrease with the distance from the center of the beam following a Gaussian distribution. The thermal history at a specific point was tracked during the 3-track simulation. Figure 2.2 (b) illustrates the position of the selected point on the powder surface and in the middle of the first laser track. The predicted and experimentally measured thermal histories at the selected point are presented in Figure 2.7 (a). The Figure indicates good agreement between the predicted thermal history during the first laser scan and the experimentally measured one. However, there are notable differences between the predicted and measured thermal histories during the second and third scans. We start by discussing details of the simulation and experimental results in the next paragraphs, and then explain the possible reasons for these observed discrepancies towards the end of the sub-section.

From the simulation results in Figure 2.7 (a), it can be seen that the selected point experienced three heating-cooling cycles with gradually decreasing peak temperatures and cooling rates during the scanning of the three tracks. The temperature of the first peak reaches approximately 3310 K, close to the boiling temperature [117], demonstrating that evaporation took place after melting of the powder during the scanning of the first track. The next two peak temperatures are predicted approximately at 1860 K and 1060 K during the scanning of the subsequent tracks. This indicates that the material experienced re-heating without melting, during scanning of the second and third tracks, and demonstrates the influence of the subsequent scanning on the previously solidified regions. Note that the effect of subsequent scanning on the already solidified region is directly proportional to the hatch distance—and thus deposited thermal energy, or energy density—used in the process. The effect of subsequent scans is reduced at larger hatch distances.

Experimental measurements of the thermal history were based on the average temperature within a 3x3 pixels window, with a pixel size of about 20 μm. The monitored point was at the center of this 3x3 window. As seen in Figure 2.7, multiple peaks appear in the thermal history of the selected point. However, only three of them (labeled as 1st, 2nd, and 3rd tracks in Figure 2.7 (a)), are due to the laser heating of the powder, while the remaining are spatters that evolve during the process. The spatter formation mechanism during LPBF was investigated in detail by Khairallah et al. [25] and experimentally observed in [126]. During melting of the powder, the molten material is built-up like a bow-wave, which results in spattering of the molten metal onto the powder particles in the vicinity of the melt pool. The small peaks observed in the thermal history illustrate this phenomenon.

To elucidate spatter formation during LPBF, the still images of the melt pool during the LPBF experiments were taken. Figure 2.7 (c) demonstrates 6 images of the melt pool taken at the times corresponding to the peaks above 900 K in Figure 2.7 (a). The small white square in Figure 2.7 (c), corresponds to the middle of the first track, where the average temperature was calculated. A spatter is seen in the white box at 0.02 s, which corresponds to the 3rd peak in Figure 2.7 (a). Looking at the color bar in Figure 2.7 (c), it is seen that the square has a temperature between 2000 and 2500 K, which is the same for the 3rd peak in Figure 2.7 (a). Looking at the image at 0.027 s in Figure 2.7 (c), a temperature above 3000 K is seen, as is observed in the 4th peak in Figure 2.7 (a). This corresponds to the time that the laser moves through the selected point on the 1st track. The other peaks can be explained in a similar way.

Other than the discrepancies originated by the spatters, there are differences in the temperature peaks corresponding to the scanning of the subsequent tracks, although the first temperature peaks perfectly match each other. Both experimental and numerical results demonstrate that the temperature reached the evaporation point in the first track. The possible sources of the discrepancies in the subsequent tracks will be discussed in the following paragraphs.

To start this discussion, it is note-worthy to highlight challenges related to the calibration of the pyrometer and associated difficulties in measuring the melt pool size. We first emphasize that the dual-wavelength pyrometer provides several benefits. It enables contact-free detection of the radiation emitted out of the laser beam-powder bed interaction even at high scanning speeds and is capable of measuring the ultra-high temperatures, and therefore, is suitable for monitoring of the melt pool temperatures [22]. Furthermore, the dual-wavelength technology is invariant to emissivity variations which typically poses significant challenges in contactless temperature measurements [127]. The dual-wavelength pyrometer has the capability of [128]: (1) compensating for signal dilution due to misalignment, smoke, dust, steam, plasma, dirty windows, (2) measuring low emissivity and compensating for emissivity alteration due to multiple factors (e.g., surface characteristics, temperature) and detecting the highest temperature. However, note that the performance of the pyrometer is highly affected by the sensor wavelength [128]. Even when careful selection of the wavelength is done, interference sources such as steam, smoke and contaminated windows can still result measurement noise. Detailed information about challenged in contactless temperature measurements using pyrometry can be found in [128]. In addition, the dual-wavelength pyrometer operates on a grey body assumption meaning that the emissivity does not depend on the wavelength, but this might

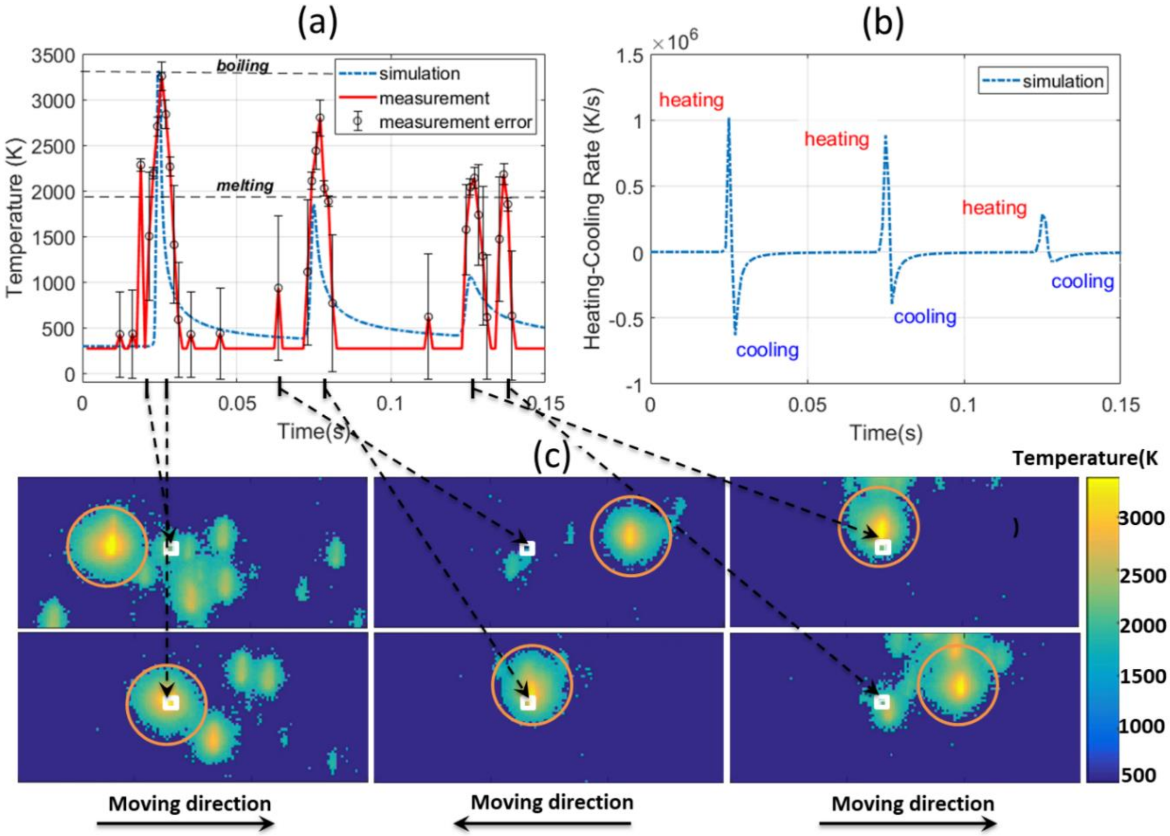

**Figure 2.7**: Comparison of the thermal history from the experiments and simulations. The small peaks in the experimental results demonstrate the spatters (a). Calculated heating-cooling rate history at the selected point on the first track (b). Evolution of the melt pool, which is indicated by a circle, during LPBF. The images are taken at the times that correspond to the peaks above 900 K in the top-left figure. The small square that is in the middle of the first track corresponds to where the average temperature is calculated. The arrows in the bottom of the Figure 2.2.demonstrates the moving direction of the melt pool (c).

not be valid for some materials with complex emissivity characteristics (i.e., aluminum, stainless steel, copper) [127, 128]. Hijazi et al. [127] suggested re-calibration of the pyrometer to determine the non-grey body compensation factor (NGCF), which was then used to eliminate the error [127]. Note that, utilizing a multi-wavelength pyrometer might be more adequate for non-grey body materials [128].

Considering the difficulties noted above, which have been observed and highlighted in previous literature works, we believe that the discrepancy between the experimental and simulation measurements of melt pool dimensions in the 3-tracks experiment originates from the measurement noise due to the absorption of the emitted thermal radiation in the vapor plume. This effect is also discussed by Bober and Singer [129]. The sensitivity study presented in the Section 2.6.2 will be helpful to understand how the thermal history at the subsequent peaks changes with an increase in the melt pool size. Note that the inaccurate temperature measurement due to vapor plume is not observed in the first peak due to the fact that the material is already evaporated and high temperatures are reached.

It is worthwhile to mention that the three-tracks experiments were performed one more time to identify whether the error was random or systematic. It was found out that the same temperature peaks during subsequent scans were obtained as seen in Figure 2.8, indicating systematic error that needs to be understood and eliminated.

#### 2.6.1.4 Cooling Rates

Investigating the effect of cooling rate during LPBF is very important since it influences the residual stresses, grain growth and other microstructural features of an LPBF part. Figure 2.7 (b) shows the calculated heating-cooling rate vs time at the selected point. The cooling rate at the selected location gradually decreases as the laser moves through subsequent tracks such that the predicted cooling rates are $-6.35 \times 10^5$ K/s, $-3.94 \times 10^5$ K/s, $-7.32 \times 10^4$ K/s corresponding to the 1st, 2nd, and 3rd tracks, respectively. Note that calculated heating-cooling rates are within the expected range ($10^3$ - $10^8$ K/s) [130] for LPBF process typically involving rapid heating and cooling cycles. Note that high cooling rates may lead to very high residual stresses [131].

### 2.6.2 Sensitivity Analysis

It is well known that the thermal history in the built part is directly influenced by the process and materials parameters. The effect of process parameters on the melt pool geometry and thermal history have been previously investigated [48, 57, 69, 71, 132]. In the current study, sensitivity analysis was performed to investigate the effect of selected material parameters, namely, thermal conductivity of the liquid phase, absorptivity, and porosity, on the thermal history and the melt pool/HAZ size. In addition, the effect of evaporation on the accuracy of the predictions will be demonstrated.

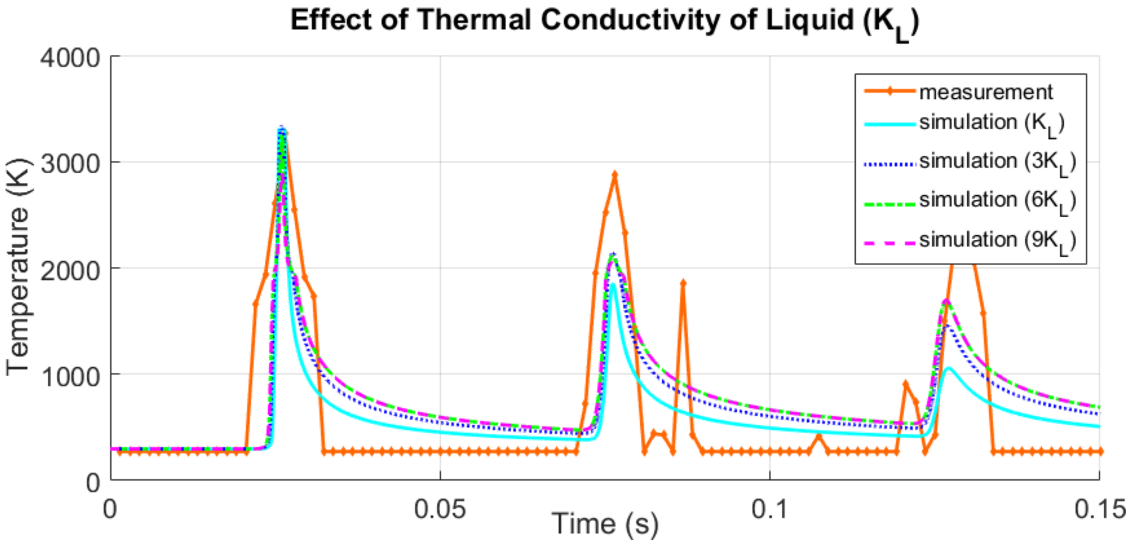

**Figure 2.8**: Effects of thermal conductivity of the liquid phase on the predicted thermal history. $K_L$ represents the thermal conductivity of the bulk material.

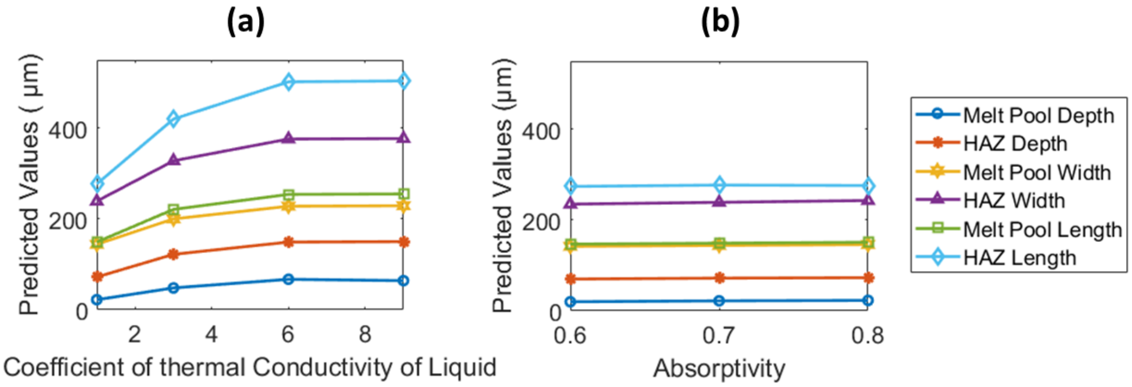

**Figure 2.9**: Effect of the thermal conductivity of the liquid phase (a) and absorptivity (b) on the predicted HAZ and melt pool sizes.

### 2.6.2.1 Effect of Material Parameters

Thermal Conductivity of Liquid Phase: To artificially account for the effect of Marangoni convection on the melt pool, the thermal conductivity of the liquid phase was increased. As already discussed, this method has been used in few previous studies [39, 62, 80]. However, there is no consensus in the community on the appropriate amount of increase for the conductivity. While a thermal conductivity that is approximately 8 times larger than that of the solid material was used in [95], a value 15 times larger was used in another recent study [79]. Therefore, in the present work the thermal conductivity of the liquid material was gradually increased and results were analyzed. Figure 2.8 presents the comparison of the thermal histories with different thermal conductivities of liquid phase, particularly 3, 6, and 9 times increased values of the originally used thermal conductivity of the liquid phase, which is presented in Figure 2.3. Increasing the thermal conductivity of the liquid phase up to a level (6 times increase) leads to an increase in the melt pool size as seen in Figure 2.9 (a), therefore enhancing the subsequent peaks in the thermal history. However, when a value 9 times larger than the original thermal conductivity of the liquid is used, a decrease in the first peak temperature that is below the boiling point is observed. This indicates that due to the ultra-high thermal conductivity used for the liquid, the deposited energy is rapidly transmitted to the regions that are far from the origin of the heat source. As a result, the energy intensity at the origin point is reduced and the boiling temperature is not reached. Note that, by increasing the thermal conductivity of the liquid about 3 times, very close agreement with the experimentally measured melt pool width (170±13 μm) is achieved. However, note that by increasing the thermal conductivity of the liquid phase, the melt pool depth also increases (as seen in Figure 2.9 (a)), and diverges from the experimental measurements. This contradicts the effect of Marangoni convection, which in general leads to a shallower melt pool depth, and hence indicates the limitation of the suggested method.

Absorptivity: A detailed discussion on the difficulties in the measurement of the absorptivity in the powder bed LPBF has been discussed above. It should be kept in mind that an acceptable deviation from the measured or predicted value of the absorptivity may occur due to these difficulties and uncertainties. In addition, it is known that the absorptivity of the material changes with temperature and is difficult or not possible to determine with 100% certainty. Therefore, simulations were performed for three different values of absorptivity (0.6, 0.7, 0.8). We limited the investigated range of the absorptivity values to what was measured/predicted for pure Ti and Ti-6Al-4V powder beds in the literature. Therefore, very low and high values were outside the scope of the current work. Figure 2.9 (b) demonstrates the slight increase in the melt pool and HAZ size with an increase in absorptivity.

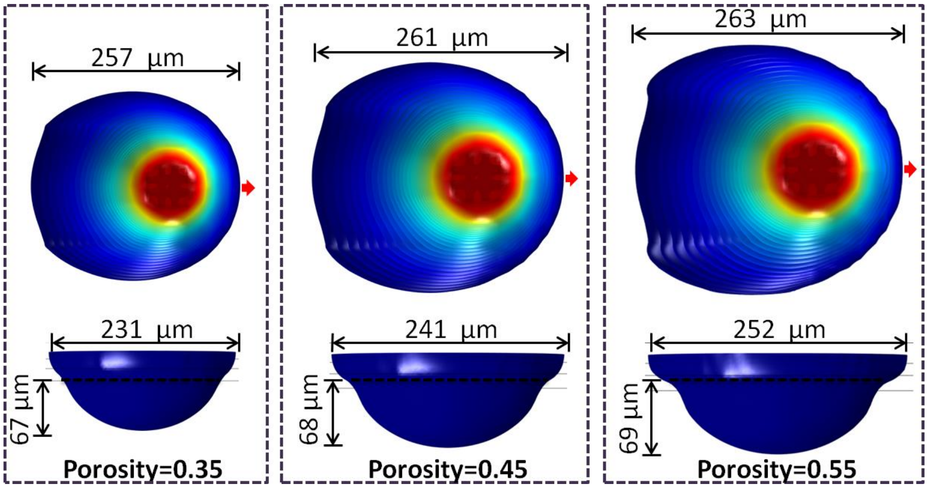

**Figure 2.10**: Change in the predicted HAZ geometry and size for different porosity values of 0.35, 0.45, 0.55. The red arrow indicates the front side of the HAZ.

Changes in the maximum temperatures in the thermal history were also investigated. It was found that by increasing the absorptivity, increases in temperatures up to about 80 K were observed in the second and third peaks while the first peak remained constant around the boiling temperature. The increase in the temperature peaks and the sizes of the melt pool and HAZ with the increase in the absorptivity can be explained by an increase in the effective applied energy input. Since the temperature of the first peak was unchanged, we can conclude that the energy intensities at each of these absorptivity values were high enough such that the temperature of the material reached the boiling temperature and evaporation took place.

Porosity: The porosity of the powder bed influences the size and geometry of the melt pool and HAZ since it directly changes the effective thermo-physical properties in the powder bed. Figure 2.10 illustrates the predicted HAZ geometry and size for different porosity values of 0.35, 0.45, 0.55 that are within the range of the expected values for the powder used in this study. As the porosity increases, the size of the HAZ increases in all directions. This can be explained as follows: by increasing the porosity, the thermal conductivity of the powder bed decreases such that the heat dissipation through conduction is less; hence the applied heat is confined within a narrow space, which results in a larger HAZ. In addition, it is clear that the geometry of the HAZ changes with a change in the porosity. This is due to the fact that a higher porosity results in a higher thermal resistance in the scanning direction (i.e., front side of the HAZ); hence the heat is dissipated through the opposite direction (i.e., rear side of the HAZ) with less thermal resistance (due to the higher thermal conductivity of the solidified material). Note that, the HAZ around the melt pool were demonstrated here. Similar trends were observed in the melt pool geometries. Since the change in the maximum temperatures with these porosity changes was not pronounced, the results are not presented here.

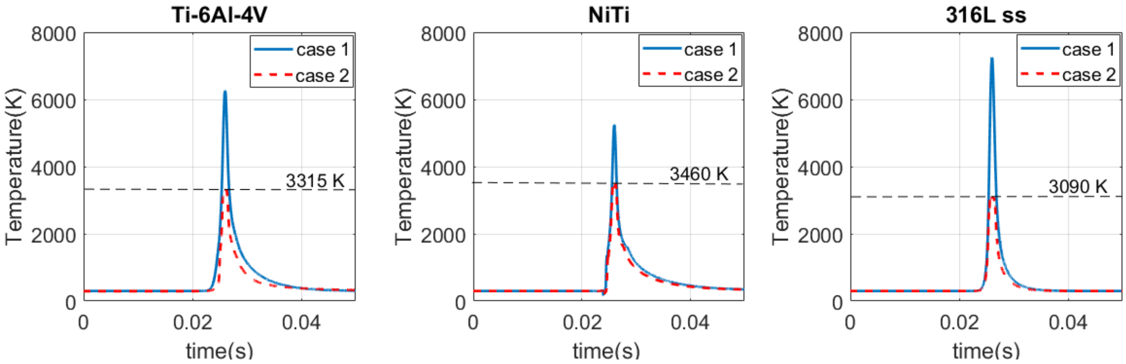

**Figure 2.11**: Comparison of the single track thermal histories from the models without (case 1) and with (case 2) taking evaporation into account.

#### 2.6.2.2 Effect of Evaporation

Figure 2.11 represents the thermal histories of different materials from the simulations with and without evaporation. In the case of Ti-6Al-4V, it is seen that by considering evaporation, the highest temperature in the molten metal is reduced from 6300 K, which is not realistic or physical, to a value that is around the boiling temperature of Ti-6Al-4V (3315 K) [117]. This decrease in the highest temperature demonstrates the importance of the heat loss through evaporation. Similar results were obtained in the case of nickel-titanium and 316L Stainless Steel. It was found that by considering evaporation the maximum temperatures decreased to around the boiling temperatures of each material, which is demonstrated in each plot in Figure 2.11. Note that the melt pool and HAZ sizes are also influenced by evaporation. In the previous sections, it was demonstrated that by considering evaporation, good agreement with the experimental measurements were achieved in the HAZ depth and width, with corresponding errors of 3.2% and 10.8%. On the other hand, it was found that the depth in the solid substrate and width of the HAZ of Ti-6Al-4V increased from 72 μm to 124 μm and from 211 μm to 348 μm, respectively, when the evaporation was not taken into consideration, which indicates a significant disagreement with the experimental measurements (i.e., corresponding errors for the HAZ depth and width were 90.8% and 59.6%, respectively)

## 2.7 Summary and Conclusions

In this study, a three-dimensional FE model was developed for studying the thermal history during laser powder bed fusion (LPBF) of Ti-6Al-4V alloy. In contrast to most existing works in the literature, the developed model considers material evaporation, which was achieved by employing a new physics-based approach. The validation experiments including state-of-the-art in-situ thermal measurements were also conducted to measure the size of the HAZ as well as to monitor the thermal history on the surface, which were then compared to the calculated values to validate the model. To our knowledge, this is the first study demonstrating a comparison of multi-track thermal history with in-situ experimental measurements using dual-wavelength pyrometry, in addition to concurrently presenting two FE model validation techniques (physical experimentation observations with SEM and pyrometer). The major findings can be summarized as follows:

1. Considering evaporation in the FE model is of importance in order to accurately predict the thermal history during the LPBF process. More specifically, it was demonstrated that the predicted peak temperature was successfully reduced to be consistent with the boiling temperature (3315 K), in contrast to an unrealistically high value (6300 K) upon accounting for evaporation in the model. In addition, the predicted HAZ size showed a much better agreement with the experimental measurements, with percent errors for the depth and width reduced from 90.8% to 10.8% and from 59.6% to 3.2%, respectively, when evaporation was considered.
2. Typical simulation results showed good agreement with the experimentally measured HAZ width and depth in the solid substrate while the melt pool width was underestimated with a 15% error. The major source of the error is believed to originate from neglected Marangoni convection. Therefore, incorporation of the fluid dynamics into the developed model will be one of the future goals.
3. The predicted and experimentally measured 3-track thermal history showed similar trends and good agreement in the first track, while few discrepancies were noted in the subsequent tracks. Possible sources of the differences were discussed.
4. A sensitivity analysis was carried out to investigate the effect of selected materials parameters on the melt pool and HAZ as well as the thermal history. The sensitivity analysis showed that the thermal conductivity of the liquid phase, porosity level of

the powder bed and the absorptivity had direct influences on the predictions, therefore, the calibration of these parameters are required. Note that this calibration is significantly difficult. Therefore, future investigations will include a systematic study on calibration of these parameters.

# 3. VERIFICATION ASSESSMENT OF TWO FINITE ELEMENT THERMAL MODELS FOR LASER POWDER BED FUSION ADDITIVE MANUFACTURING

## 3.1 Overview

Laser Powder Bed Fusion (LPBF) is a fast-developing metal additive manufacturing process offering unique capabilities including geometric freedom, flexibility, and part customization. The process induces complicated thermal histories with high temperature gradients and cooling rates, leading to microstructures and mechanical properties different from those produced conventionally. A more in depth understanding and control of the thermal history is needed to achieve desired performance of the LPBF fabricated parts. Computational modeling and simulation offer notable advantages that support and complement experimental techniques. However, the accuracy of their results is often unknown. Verification and Validation (V&V) are the primary means of assessing the accuracy and reliability of numerical models. A significant number of numerical models have been developed to study the thermal history in LPBF processes. While experimental validation of the thermal models by means of comparisons of melt pool size were conducted in the majority of studies, verification of the thermal models went unheeded. However, verification also contributes to building credibility in these models. In this paper, a V&V study for thermal modeling of LPBF processes is presented. Two different finite element-based thermal models are developed and implemented in two different platforms (Comsol Multiphysics® and Sierra Mechanics). Simulations are run using the same process and material parameters for the verification purposes. The predicted melt pool sizes and the thermal histories are compared under different conditions and different locations of the fabricated part and the effect of temperature dependent thermo-physical properties, phase transitions, and evaporation are investigated. In addition, the influences of mesh size, domain size, and error tolerance are discussed. For validation, the predicted melt pool sizes are compared with those experimentally measured.

## 3.2 Introduction

Additive Manufacturing (AM) technologies enable the fabrication of physical objects directly from a three-dimensional CAD model through adding materials layer-by-layer. Laser powder bed fusion (LPBF) [133] is a class of powder bed based AM techniques which employs a laser beam to selectively melt metallic powders placed in a powder bed in a layer-wise fashion. The capabilities offered by LPBF processes such as producing near net shape fully-dense parts with high degrees of geometric complexity and customization are well understood by now. In addition to well-known capabilities, its ability to produce materials with spatially-tailored properties are demonstrated [17]. The challenges that hinder its widespread adoption are also defined and agreed upon by the scientific and industrial communities. These include high susceptibility to defects (e.g., delamination, porosity, cracks) and variability in the microstructures [134] and performance of fabricated parts. As a first step towards addressing some of these challenges, adequate understanding (and control) of the thermal history during part fabrication is necessary.

Numerical models offer notable advantages that support and complement experimental techniques. A significant number of numerical models have been developed to study the thermal history of LPBF and other similar AM processes [49, 79, 135, 136] . Experimental validation has been an essential aspect in such models whereby model predictions are compared with experimentally measured melt pool geometry and temperature. While experimental validation is extremely important, it has its own challenges. For example, there are challenges associated with in-situ measurement of the melt pool temperature in metal AM (e.g., extremely high peak temperatures above the operating range of conventional thermocouples, and difficulties in implementation of contactless temperature measurement techniques) [22, 23]. In addition, experimental measurement techniques are limited to capturing temperatures at a point or a surface, hence it is not possible to investigate the full thermal history of the entire part, especially in the case of LPBF processes. Due to these limitations of experimental measurement techniques, validation procedures should be supported with verification. Verification focuses on whether the problem has been solved correctly, whereas validation focuses on whether the correct problem has been solved. Both verification and validation (V&V) are processes that enhance the correctness or reliability of the model, thus can ensure that the model is adequate for its intended use. For example, it is not uncommon in such models to have two mathematical errors cancel each other, leading to a right answer obtained by chance. To eliminate similar issues, verification should be carefully performed before validation.

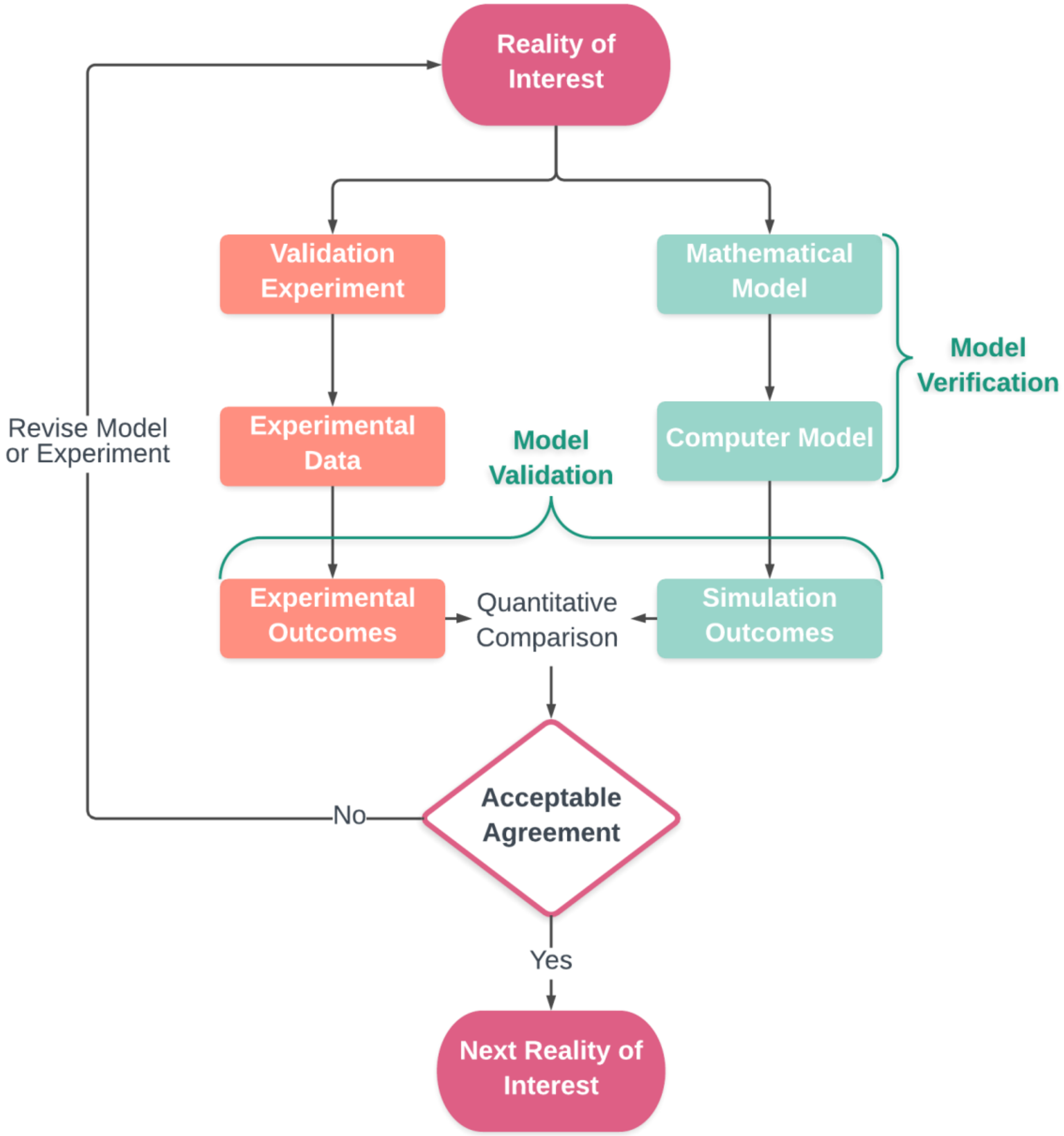

**Figure 3.1:** Model verification and validation process

With rapid advances in modeling and simulation for AM (and other applications), V&V processes continue to be a theme of special interest. In 2002, participants from government, academia and industry met to describe the foundations for modeling and simulation V&V in the 21st Century in the Foundations ’02 workshop [137]. The American Society of Mechanical Engineers (ASME) has created a Committee to promote the development of standards for V&V procedures for computational models and simulations. A number of reports on V&V procedures in a variety of fields [138, 139] have been published by this committee. Los Alamos National Laboratory published an overview [140] to describe the definitions, concepts and procedures to successfully perform V&V for complex computational models. National Aeronautics and Space Administration (NASA) and Air Force Research Laboratory (AFRL) have been working on the development of guidelines and activities for V&V to enable the use of numerical models for certification [140]. Recently, NASA emphasized the need for a V&V study on the finite element-based thermal modeling of LPBF process to enable an accurate prediction of the transient thermal response during the process [141].

A schematic of the V&V process is presented in Figure 3.1. The schematic illustrates the typical modeling and assessment processes involved in V&V. In Figure 3.1, *Reality of Interest* represents the investigated physical problem. The right branch in Figure 3.1 represents modeling activities, and the left branch represents experimental activities. The *Mathematical Model* consists of the mathematical governing equations (e.g. partial differential equations, initial and boundary conditions) describing the *Reality of Interest*. The *Computer Model* refers to the numerical implementation of the *Mathematical Model* such as a finite element-based model. It involves the computer code, solution method, mesh size, and error tolerances. Model verification should be performed during the development of the *Computer Model*. It focuses on the identification and removal of errors in the numerical implementation of the *Mathematical Model.* Subsequently, to conduct model validation the *Simulation Outcomes* are compared with the *Experimental Outcomes* obtained from designed *Validation Experiments*.

Verification has two aspects: code verification and calculation verification. Code verification is required to make sure the code algorithms are working correctly. The two models presented in the current work are implemented in Comsol Multiphysics® (a commercial software with rigorous quality assurance) and Sierra Mechanics which has already been developed, tested, and verified by Sandia National Laboratories. Therefore, code verification is outside the scope of the present work. Calculation verification is performed to ensure that the model's solution is sufficiently accurate. A typical calculation verification assessment includes studies on mesh, time and error tolerances [140]. In calculation verification activities, the accuracy of the model is primarily determined relative to an existent highly accurate solution (e.g. an analytical solution or a highly accurate numerical solution). However, in some cases due to the complexity of the "reality of interest", it may not be possible to find a highly accurate solution. In this scenario, code-to-code verification is recommended [140].

Validation assessment is performed to determine how accurate the model represents the physical *Reality of Interest* and whether an *Acceptable Agreement* is achieved or not, as illustrated in Figure 3.1. If the agreement is not to satisfactory level, then the model or the experiment is revised.

In this paper, a V&V study related to thermal modeling of LPBF metal AM processes is presented. Two different finite element-based thermal models are developed and implemented in two different platforms (Comsol Multiphysics® and Sierra Mechanics) and simulations are run using the same process and material parameters. First, a thorough discussion on the effect of typical modeling parameters including mesh size, domain size, and error tolerance on the accuracy of the solution is presented. Next, a number of case studies are performed, the predicted melt pool sizes and the thermal histories are compared under different conditions and different locations of the fabricated part. In addition, the effect of temperature dependent thermo-physical properties, phase transitions, and evaporation on the thermal history are presented. While the focus of this study is on code-to-code verification, experimental validation is also conducted for completeness.

The structure of the article is as follows: in Section 2 a literature review on thermal modeling of AM processes is conducted. The mathematical description of each model including governing equations, initial conditions, boundary conditions, and modeling assumptions are presented in Section 3. Section 4 is dedicated to the verification assessments. First, the effect of typical modeling parameters on the accuracy of the solution is discussed. Next, a code-to-code verification process is performed and the predicted melt pool sizes and the thermal histories are compared. Afterwards, the validation of the models is carried out through the comparisons of predicted and experimentally measured melt pool sizes in Section 5. Finally, the article is concluded with Section 6, in which the important findings are summarized.

## 3.3 Literature Review

Two different approaches in modeling powder particles have been employed in the literature: powder-scale and continuum-scale. The powder-scale approach (e.g., [25, 49-53, 142, 143]) offers higher accuracy through simulating the size variations and the non-uniform distribution of the particles, and in turn the local changes in the melt pool (incomplete melting, consolidation, spatter formation, pore defects, denudation zone) [25, 49]. This approach, however, is computationally expensive, which makes it almost impossible to use in full-part simulation. The continuum-scale approach, on the other hand, is computationally less expensive, potentially applicable to a full part simulation, and has been widely adopted in the literature [26, 39, 41-43, 77]. Since the powder particles are assumed as a homogeneous layer in this approach, effective thermo-physical properties must be utilized to account for the powder porosity. Sih and Barlow [96] developed an inclusive model to predict the thermal conductivity of the powder bed as a function of multiple parameters such as, porosity of the powder bed, size of the powder particles, and thermal conductivity of the bulk material. The model has been utilized in a number of LPBF studies [45, 57, 60, 65]. Simpler models, only accounting for the thermal conductivity of bulk material and the powder porosity, are also available and have been employed in previous works [26, 58, 66, 69, 71]. The density of the powder bed has been modeled in a variety of studies [26, 69, 71]. Some investigations using the same density of the bulk material for the powder bed also exist [39, 41, 62, 74]. Regarding the specific heat capacity of the powder bed, majority of previous studies used the values for the bulk material [39, 43, 47, 69, 71, 74, 97].

Different physical mechanisms associated with the LPBF process have been considered in the current continuum scale thermal model simulations: heat transfer through conduction, heat loss through radiation/convection/evaporation, and fluid dynamics effects in the melt pool. While the simplest form of Fourier’s heat conduction equation has been utilized in some studies [54, 60, 82-85], the majority of investigations [48, 52, 58, 78, 86-89] have modified it to consider the latent heat of fusion/evaporation. Heat loss through radiation has been taken into account in some studies [25, 40, 59], but it was also neglected in a number of literature studies [26, 39, 69] due to the small size of the high temperature region in the build part. Since the LPBF process is conducted in an inert gas environment, heat loss through convection has been taken into account in the majority of studies [26, 61, 66]. Finally, heat loss through evaporation has been neglected in most of the studies [26, 47, 69]. However, if the applied energy is high, neglecting evaporation might unrealistically over-predict temperatures above the boiling temperature of the material being processed. Evaporation has been modeled based on the vapor pressure in various investigations [25, 43, 51, 90, 91]. This method is computationally more expensive and relatively difficult to implement compared to a pure heat transfer model. Loh et al. [71] employed a simpler method to account for evaporative heat loss by increasing the thermal conductivity in the build direction once the material is evaporated. In the present study, a simple and efficient method to account for evaporation was used, which will be described in Section 3.

While a number of literature studies have taken fluid dynamics effects in the melt pool into consideration [53, 91, 92], most of the works in the literature [41, 59, 62, 74] have ignored these effects for simplification purposes. Some models [40, 76] which accounted for both heat transfer and fluid dynamics have been developed and the effect of fluid dynamics (i.e., Marangoni convection) on the melt pool geometry and size have been investigated. Results have shown that a melt pool with larger width and shallower depth is obtained due to Marangoni convection. In another work [25], complex physical mechanisms associated with the melt flow were considered (e.g., Marangoni convection, depression, denudation, spatters, pore defects, incomplete melting, recoil pressure). Liu et al. [93], Taylor et al. [94], and De and DebRoy [95] proposed an alternative method, based on increasing the thermal conductivity of the molten metal, to account for the convective effects in the melt pool for the pure heat transfer models. It has been utilized and validated in some studies [39, 62, 79].

Temperature-dependent material properties have also been taken into consideration in numerous investigations [26, 39, 41, 43, 62, 71, 73, 74, 88], while a few other studies [54, 61, 87, 89] assumed constant properties for simplification. Note that, due to rapid temperature changes and high temperature gradients occurring during LPBF, incorporating temperature-dependent material properties in the thermal models becomes crucial for accurate prediction of the thermal history during processing. Other important material properties include laser absorptivity and the emissivity of the powder bed. Sih and Barlow suggested a model to predict the emissivity of the powder bed as a function of the porosity and the emissivity of the bulk material [96]. The model has been adopted in the literature [45, 62] and reasonable agreement with experimentally measured values was obtained. Some other studies [74, 98, 99] employed temperature dependent emissivity for the powder bed. In the present work, a constant emissivity value as in [39, 40, 71] was found suitable due to the negligible change in predictions when temperature dependent values were used. Predictive models for the laser absorptivity in the powder bed have also been developed [100, 101] as complement to experimental measurements [102] which can be complicated due to multiple factors affecting absorptivity such as temperature, beam intensity, wavelength, and oxidation.

The heat source model employed in thermal simulations is an important consideration towards achieving accurate temperature predictions. Two-dimensional [41, 58, 106-108] and three-dimensional [62, 109, 110] Gaussian distributed moving heat source models have been developed and employed in different studies of powder bed-based AM processes. Note that, in a vast majority of the LPBF studies [43, 47, 48, 60, 69, 71, 78] a two-dimensional heat source was found suitable. Alternatively, the Ray Tracing (RC) model was proposed [111] and has been reported in some recent works [25, 26].

Volume shrinkage during melting of the powder was taken into account in various models [48, 71, 114] and differences in the melt pool size and the peak temperature were reported [48]. Addition of successive layers based on “element birth and death” method was modeled in some literature studies [47, 58, 115, 144]. Recent studies have been focused on multi-scale multi-physics simulation of AM processes in which the predicted thermal history is used as an input to investigate the microstructure or mechanical properties of the AM part [37, 145, 146].

Based on the above review, it is clear that a plethora of studies on thermal modeling of the LPBF process are already available. Although the experimental validation of the thermal models has been provided in many of the studies, research on the verification of the models is much less studied in the existing literature. The present work emphasizes the significance of model verification and presents a V&V study on the thermal modeling of the LPBF process.

## 3.4 Mathematical Description of Models

The LPBF process involves multiple physics (e.g. heat conduction, convection, radiation, evaporation, phase transitions, powder-laser interactions, melt pool dynamics), leading to complicated thermal histories within the fabricated part. In the present work code-to-code verification was performed as recommended in [140]. Two different models,

Model 1 and Model 2, were developed and implemented in two different finite element software packages, Comsol Multiphysics® and Sierra Mechanics, respectively. Single-track and three-tracks simulations during LPBF of Ti-6Al-4V alloy were conducted to predict the thermal history and melt pool size. The same process parameters, material properties and physics were used in both models, while the numerical implementation and the modeling parameters such as mesh size, mesh type, or error tolerances used in the models were set differently. The laser power and the scanning speed used in these simulations were 50 W and 80 mm/s, respectively. The hatch spacing was set to 70 μm for the three-tracks simulation. Note that the process parameters used in the model were determined to ensure successful prints (i.e., without lack of fusion or macro size defects) based on the previous experience on the printing of the particular material. The laser switching off and on between the tracks was not considered in the present models. The details of each model are first described in the following subsections.

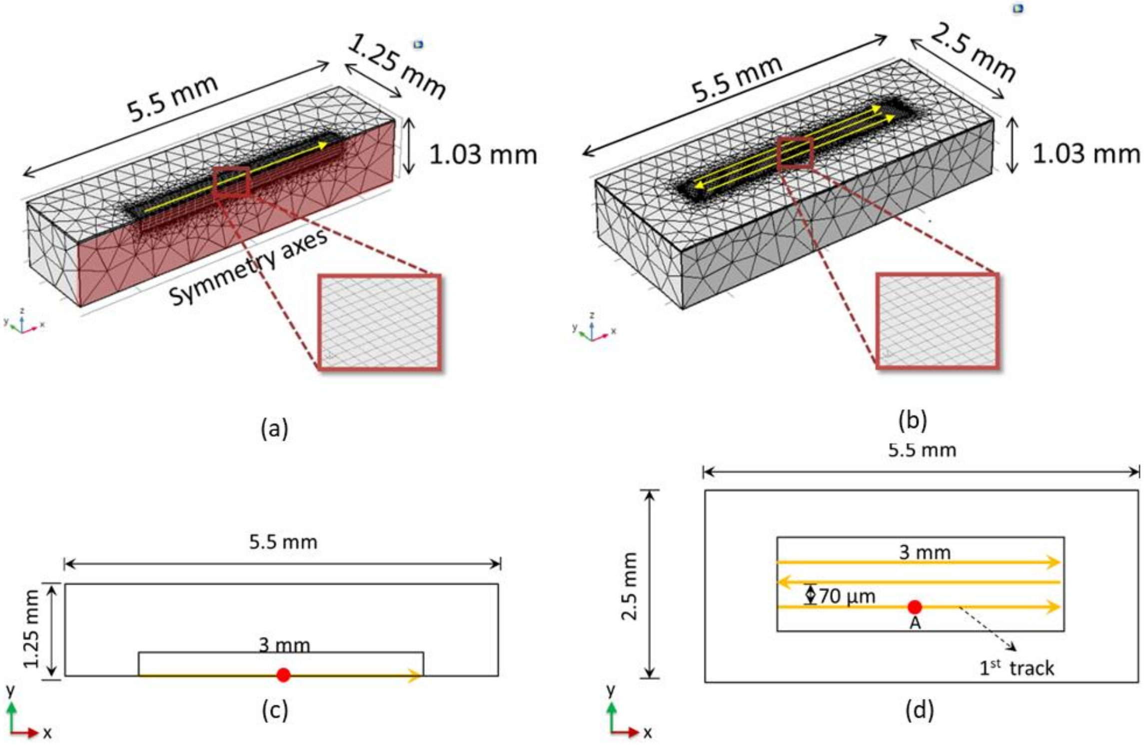

**Figure 3.2:** Three-dimensional simulation domain and meshing geometry and the scanning strategy during LPBF simulations for the two cases: (a) single track, (b) three tracks in Model 1. Symmetry plane in the single-track model is shaded in red (a). The red dot represents the position of the selected point at which thermal history is measured for two cases: (c) single track, (d) three tracks.

### 3.4.1 Model 1

Model 1 was developed in Comsol Multiphysics® software. The three-dimensional models for single- and three-tracks simulations consisting of a thin layer of powder (30 μm) and a thick substrate are presented in Figure 3.2 (a) and (b), respectively. The scanning strategies as well as the position of Point A, where the thermal histories are measured, are depicted in Figure 3.2 (c) and (d) for single-track and three-tracks simulations, respectively. Due to the high computational cost, the substrate size was reduced without losing the accuracy of the solution as described in Section 4.3. The resultant model size for the three-tracks simulation was 5.5×2.5×1.03 mm, while it was set to 5.5×1.25×1.03 mm for the single-track simulation due to the symmetry axes employed as the boundary condition along the laser scanning direction (x-axis). The track length was 3 mm and the laser beam was simulated to move between the points x = 1.25 mm and x = 4.25 mm along the x-axis on the top surface as shown in Figure 3.2 (c) and (d).

The heat applied by the laser beam to the powder surface is transported through conduction to the surrounding powder particles and the substrate. The heat conduction equation is given by

$$\rho C_p \frac{\partial T}{\partial t} + \nabla(-k\nabla T) = Q \tag{1}$$

where $\rho$ is the density of the material, $C_p$ is the specific heat capacity, $T$ is the temperature, $t$ is the time, $k$ is the thermal conductivity and $Q$ is the volumetric heat flux. The phase transitions between the phases (i.e.; solid-liquid and liquid-gas) during LPBF was modeled based on the apparent heat capacity method and the effect of latent heat was also considered as presented in Equations (8)-(9).

The initial temperature of the build was set to the ambient temperature expressed as:

$$T\ (x, y, z, t)_{t=0} = T_0 = 298\ \mathrm{K} \tag{2}$$

The temperature on the boundary surfaces, except the top surface, was kept at the ambient temperature during the simulation.

Natural convection and radiation heat fluxes were applied on the powder surface as boundary conditions expressed as:

$$q_{convection} = h(T_{amb} - T) \tag{3}$$

$$q_{radiation} = \varepsilon \sigma_{\mathrm{B}}(T_{amb}^4 - T^4) \tag{4}$$

where $h$, $T_{amb}$, $T$, $\varepsilon$ and $\sigma_{\mathrm{B}}$ are the coefficient of the convective heat transfer, the ambient temperature, the current temperature, the emissivity coefficient and the Stefan–Boltzmann constant, respectively. The emissivity coefficient for the present study was set to 0.7 according to [99] and the value of $h$ was set to $14\ \mathrm{W/m^2K}$.

The laser was modeled as a moving two-dimensional, surface heat flux with Gaussian distribution defined as:

$$Q_{laser} = \frac{PA}{2\pi\sigma^2} e^{(-\frac{d^2}{2\sigma^2})} \tag{5}$$

where $P$ is the laser beam power, $A$ is the absorptivity, $\sigma$ is the standard deviation described as $\sigma = \frac{1}{4}D$ where $D$ is the beam diameter, and $d$ is the radial distance from the center of the beam. The values of $P, A,$ and $D$ are set to $50\ \mathrm{W}, 0.7,$[102] and $70\ \mu\mathrm{m}$, respectively.

The thermo-physical properties during phase transitions are described by the following equations:

$$\rho(T) = \sum_{i=1}^{N} \theta_i \rho_i(T) \tag{6}$$

$$k(T) = \sum_{i=1}^{N} \theta_i k_i(T) \tag{7}$$

$$C_p(T) = \frac{1}{\rho}\left(\sum_{i=1}^{N} \theta_i \rho_i(T) C_{p,i}(T)\right) + \sum_{j=1}^{N-1} L_{j\to j+1} \frac{d\alpha_{m,j\to j+1}}{dT} \tag{8}$$

$$\alpha_{m,j\to j+1} = \frac{1}{2}\frac{\theta_{j+1}\rho_{j+1}(T) - \theta_j \rho_j(T)}{\theta_{j+1}\rho_{j+1}(T) + \theta_j \rho_j(T)} \tag{9}$$

where $\theta_i$ is the volume fraction of phase $i$, which linearly changes from 1 to 0 during the phase transition interval of $dT$ while $k_i(T)$, $\rho_i(T)$ and $C_{p,i}(T)$ are the conductivity, density and heat capacity of phase $i$, respectively. The value of $dT$ is set to $(T_{m-}T_s)$ for melting and is estimated to be 30 K for boiling. Here, $T_m$ is the liquidus temperature and $T_s$ is the solidus temperature with the values of 1923 K and 1878 K, as presented in Table 3.1. The total number of the phases present in the system was $N = 3$ considering the solid, liquid and vapor phases represented with the indices of $i$=1,2,3, respectively. The parameter $L_{j\to j+1}$ represents the latent heat of fusion ($L_f$) or the latent heat of evaporation ($L_v$) depending on the type of the phase transition taking place. The function $\alpha_{m,j\to j+1}$ describes the mass fraction of the phase after transition.

The porosity of the powder during melting is described by the function Ø such that

$$Ø(\mathrm{T}) = \begin{cases} Ø_{0,} & T_0 < T < T_{sint} \\ \dfrac{Ø_0}{T_{sint} - T_m}(T - T_m), & T_{sint} < T < T_m \\ 0, & T > T_m \end{cases} \tag{10}$$

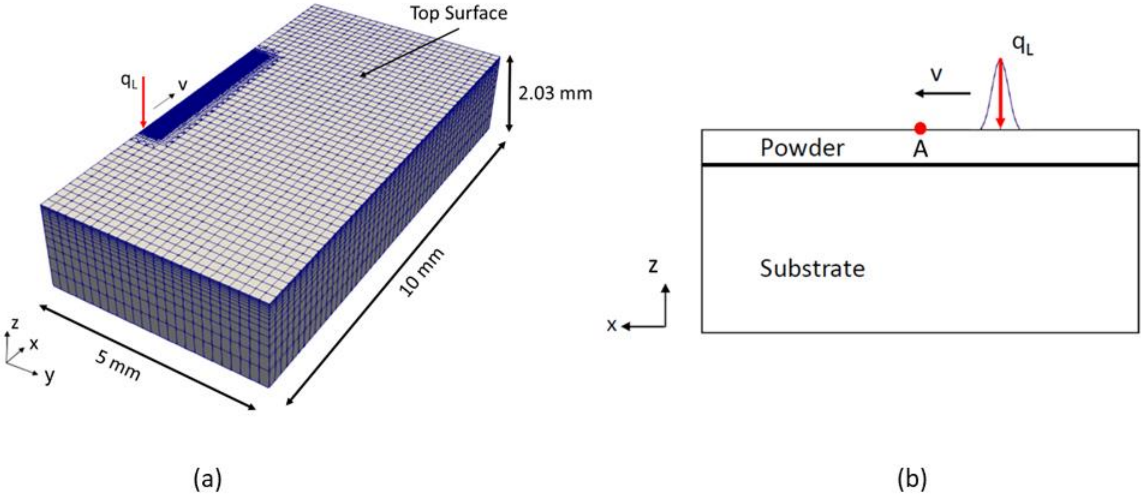

**Figure 3.3**: For model 2, (a) the three-dimensional simulation domain and meshing geomety for single-track case, (b) and the position of Point *A* within the simulation domain where metrics are measured.

where $\emptyset_0$, $T_{sint}$, $T_m$ are initial powder porosity, sintering temperature and liquidus temperature, respectively. $T_{sint}$ was set to 1223 K. The porosity of the powder decreases to 0 when the powder is fully melted. Note that $\emptyset(\mathrm{T}) = 0$ for all temperatures once the powder is fully melted.

**Table 3.1:** Materials and process parameters used in the simulations

| Parameters | Values |
|---|---|
| Boiling temperature, $T_v$ (K) | 3315 [117] |
| Liquidus temperature, $T_m$ (K) | 1923 [118] |
| Solidus temperature, $T_s$ (K) | 1878 [118] |
| Latent heat of fusion, $L_f$ ($\mathrm{kJ/kg}$) | 286 [118] |
| Latent heat of evaporation, $L_v$ ($\mathrm{kJ/kg}$) | 9830 [118] |
| Absorptivity, $A$ | 0.7 [102] |
| Emissivity coefficient, $\varepsilon$ | 0.7 [99] |
| Initial powder porosity, $\emptyset_0$ | 0.35 |
| Powder layer thickness, $V$ (μm) | 30 |
| Laser beam diameter, $D$ (μm) | 70 |
| Laser beam power, $P$ (W) | 50 |
| Scanning speed, $V$ ($\mathrm{mm/s}$) | 80 |

| | |
|---|---|
| Hatch spacing, $H_d$ (μm) | 70 |
| Track Length (m) | 3 |

The effective thermo-physical properties for the powder layer, in particular the effective density $\rho_{eff}$ and the effective thermal conductivity $k_{eff}$, are defined as [97]:

$$\rho_{eff}(T) = \rho_{solid}(T)(1 - \emptyset(T)) \tag{11}$$

$$k_{eff}(T) = k_{solid}(T)(1 - \emptyset(T))^{n} \tag{12}$$

where $\rho_{solid}$ is the density of the bulk solid, $\rho_{eff}$ is the density of the powder, $k_{solid}$ is the thermal conductivity of the bulk solid, $k_{eff}$ is the thermal conductivity of the powder, $\emptyset$ is the porosity function as described in Equation (10), and $n$ is the empirical parameter. In the present model, $n$ was set to 4 according to Yin et al. [97]. The specific heat capacity for the powder is assumed to be the same as that of the bulk material as suggested in [39, 43, 47, 69, 71, 74, 97]. Initially, the effective thermo-physical properties as described in (11) and (12) are assigned for the powder layer, while the bulk properties are used once the molten powder solidifies. This was achieved by introducing a simple material phase switch method. Basically, a variable $q$ representing the different forms of the solid phases ($q = 0$: powder, $q = 1$: bulk) was introduced and its value was changed from 0 to 1 when the phase change criterion (i.e., $T > T_m$ ) was satisfied. Therefore, the general formulation for calculating the thermal conductivity of the powder layer in solid phase ($i$=1) becomes:

$$k_{powder\_layer}(T) = \begin{cases} k_{eff}(T), & T < T_m \; and \; q = 0 \; (before \; melting) \\ k_{solid}(T), & T < T_m \; and \; q = 1 \; (once \; solidified) \end{cases} \tag{13}$$

Temperature dependent material properties of Ti–6Al–4V for bulk solid phase were used from [118] and extrapolated according to [39] to obtain the properties for liquid phase. Regarding the powder properties, the thermal conductivity and density were calculated based on Equations (11) and (12), while the same values for the specific heat capacity of the bulk solid was used as in the majority of the previous literature [39, 43, 47, 69, 71, 74, 97]. Due to the lack of information in the literature, the thermo-physical properties of the vapor phase were estimated based on similar materials' properties. The material and process parameters used in the present study are listed in Table 3.1, while the thermo-physical parameters are illustrated in Figure 3.4.

The trial simulations showed that the applied energy density was high enough for both melting and evaporation of the powder, hence heat loss due to evaporation was considered.

A surface heat flux on the powder bed surface was applied as a boundary condition to account for the heat loss due to evaporation of the material and defined as

$$Q_{sink} = -\theta_3 * m_v * L_v \tag{14}$$

Here, $m_v$ and $L_v$ represent the mass of vapor and the latent heat of evaporation, respectively. The mass of vapor is calculated based on the volume fraction of vapor phase $(\theta_3)$, which is updated at each time step. No heat loss due to evaporation occurs for $\theta_3 = 0$.

The assumptions made in the model are as follows. The powder layer was represented as a continuum medium with effective thermo-physical properties and an initial porosity of 0.35. For simplification, volume shrinkage during melting of the powder, Marangoni convection and other fluid dynamics effects such as denudation, spatter, incomplete melting were neglected. The absorptivity of the laser beam and the emissivity of the powder bed were assumed to be constant with the value of 0.7 based on [102]. Khairallah [25] pointed out that the mass loss due to evaporation during LPBF was negligible, hence was neglected in our simulation.

### 3.4.2 Model 2

Model 2 was implemented in Sierra Mechanics. Note that the process parameters, material properties, and physics in this model were the same as those in Model 1, while the two models differ in terms of their numerical implementation, the size of the simulation domain, and the modeling parameters such as mesh size, mesh type, or error tolerances. In this section, only those differences in Model 2 will be described.

A simulation domain consisting of a 10×10×2 mm substrate with a 30 µm powder layer was utilized in the three-tracks simulations, while the size of the domain reduced to 10×5×2 mm in the single-track simulations and a symmetry boundary condition in the x-z plane along the scan path was applied (as shown in Figure 3.3 (a) to increase the computational efficiency. Hexahedral elements were used throughout the simulation domain. The mesh size for the substrate and powder layer was 22 μm in the $x$ and $y$ directions along the laser scan path due to the high temperature gradients near the melt pool region. A coarser mesh size was applied away from the scan path region. The level of mesh refinement within the scan path region was determined by convergence of the melt pool depth and the peak temperature at Point $A$ shown in Figure 3.3 (b), which is in the middle of the laser scan and at the surface of the powder bed. The percent difference in the peak temperature at Point $A$ and melt pool depth for refinement to a mesh size of 11 μm was 0.19% and 0.18%, respectively.

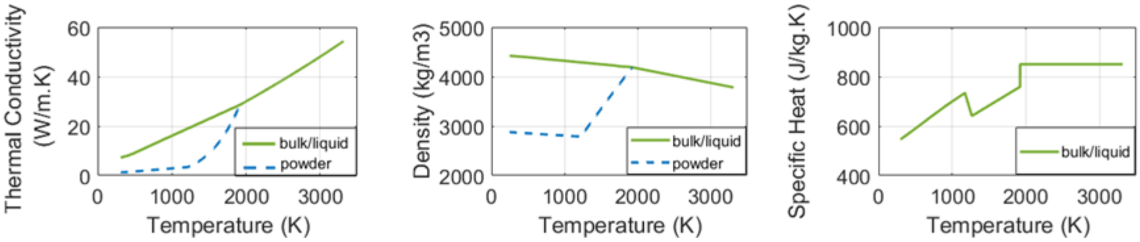

**Figure 3.4**: Thermo-physical properties of Ti-6Al-4V (solid properties are reported in [69], liquid properties are extrapolated according to [23], powder properties are calculated based on Equations 11 and 12).

### 3.5 Model Verification

As previously discussed in Section 1, there are two main tasks involved in model verification: code verification and calculation verification, and the focus of the present work is on the latter. It is worth mentioning that although the same physics and material properties were used, Model 1 was initially computationally more expensive than Model 2 (10 times slower), hence rigorous analysis was first carried out for Model 1 to optimize the mesh size/type, error tolerance, and domain size, such that the simulation time is reduced without losing the accuracy of the solution. It is common to conduct this type of analysis as part of calculation verification assessments [140]. Note that this analysis is conducted and presented for Model 1 in this work since it had not been conducted previously, unlike Model 2 whose mesh sizes and error tolerances were optimized a priori. Afterwards, the predicted thermal histories and melt pool sizes from each model will be compared and discussed to enable code-to-code verification. To avoid two mathematical errors canceling each other in the models, simulations were run for a number of different cases and the predictions were compared at different locations within the simulated prints.

### 3.5.1 Effect of Mesh Size

Meshing is one of the important factors to consider in finite element modeling. The quality of the mesh directly affects the convergence and accuracy of the solution. To ensure an adequate mesh, several factors must be taken into consideration, such as aspect ratio, element type and element size. In general, a high aspect ratio (ratio of the longest to the shortest element dimension) must be avoided. An aspect ratio which is equal to one is considered ideal. A variety of element types including 2D and 3D elements are available for meshing. The tetrahedron provides flexibility for meshing complex 3D geometry. However, it is not always the best choice. One reason to use other element types such as hexahedron or pyramid is that they can significantly reduce the memory and time requirements through reducing the total number of elements. The algorithm in Comsol for creating a tetrahedral mesh maintains an aspect ratio close to one. Therefore, it is plausible to utilize other element types with high aspect ratios at locations where the solution varies slowly to help reduce the computational requirements. Note that the optimal mesh will typically be a combination of different element types. In addition to the element type, careful selection of the element order and size is needed. Element order is correlated to the number of nodes used in a single element. Different element orders require different memory and time requirements. For example, a significant reduction in computation time can be achieved by using a first-order quadrilateral Lagrange element instead of a second-

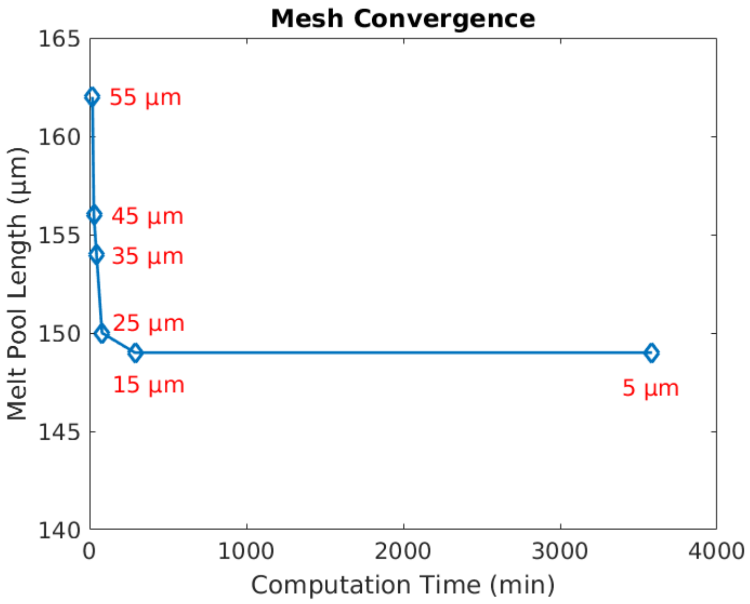

**Figure 3.5:** Effect of mesh refinement on the melt pool length and total computation time is presented.

order quadrilateral Lagrange element. Note that, for a single physics problem, all the element orders will converge to the same solution as long as a sufficiently refined element is used. A mesh convergence study using a variety of element sizes is required to assure solution accuracy with respect to the element size. In general, smaller element sizes yield higher solution accuracy. However, this in turn results in an increase in computational cost. The trade-off between the accuracy and the computational cost must be taken into consideration in the selection of the correct element size. Mesh convergence is performed through reducing the element size and checking the solution convergence as well as the time requirement. It is in general observed that when a sufficiently small element size is reached, the solution accuracy will generally be the same for further reduction of the

**Table 3.2:** Mesh Convergence Study

| Mesh Size (μm) | Computation Time | Melt Pool Size (μm) (Length-Width-Depth) | Total Number of Elements |
|---|---|---|---|
| 5 | 59 hr 45 min | 149-144-52 | 592451 |
| 15 | 4 hr 50 min | 149-144-52 | 80384 |
| 25 | 1 hr 20 min | 150-144-52 | 33349 |
| 35 | 45 min | 154-144-54 | 20600 |
| 45 | 28 min | 156-150-54 | 13675 |
| 55 | 19 mins | 162-152-53 | 10561 |

element size while the time requirement will increase significantly (Figure 3.5). To reduce the time, a small element size is preferred only where the solution changes rapidly, while a coarser element size is applied for other locations.

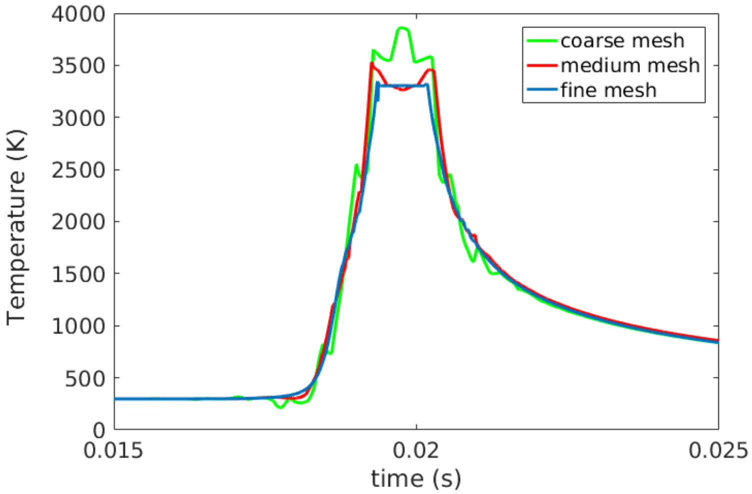

**Figure 3.6:** Thermal history is plotted for the three different mesh sizes: fine (15 µm), medium (35 µm), coarse (55 µm). The corresponding peak temperatures for coarse, medium and fine meshes are 3852 K, 3477 K, 3315 K.

In the present study, the meshing of the domain was established in the light of the previous information. Performance of different element types and sizes were compared. The best meshing was achieved using a combination of hexahedral and tetrahedral elements. Hexahedral elements with an aspect ratio close to 1 were used where the temperature variations are rapid, while tetrahedral elements were used at other locations. A mesh convergence study was also performed to be able to find the best mesh size. The result of this study is presented in Figure 3.5 and Table 3.2. It can be seen that the minimum element size of 25 µm was found best in terms of accuracy and computation time. In addition, the thermal histories are shown in Figure 3.6 for selected mesh sizes: fine (15 μm), medium (35 μm), coarse (55 μm). The corresponding peak temperatures for coarse, medium and fine meshes are 3852 K, 3477 K, 3315 K, respectively. It is observed that reducing the mesh size decreases the peak temperature as well as the noisy peaks.

**Table 3.3:** Effect of Error Tolerances on the Computation Time

| Test Number | $RTol$ | $ATol$ | Computation Time |
|---|---|---|---|
| Test 1 | $1 \cdot 10^{-1}$ | $1 \cdot 10^{-1}$ | Error (convergence issue) |
| Test 2 | $1 \cdot 10^{-3}$ | $1 \cdot 10^{-1}$ | 35 hr 25 min |
| Test 3 | $1 \cdot 10^{-3}$ | $1 \cdot 10^{-3}$ | 6 hr 24 min |
| Test 4 | $1 \cdot 10^{-3}$ | $1 \cdot 10^{-5}$ | 6 hr 16 min |
| Test 5 | $1 \cdot 10^{-3}$ | $1 \cdot 10^{-7}$ | 8 hr 20 min |
| Test 6 | $1 \cdot 10^{-5}$ | $1 \cdot 10^{-3}$ | 4 hr 5 min |
| Test 7 | $1 \cdot 10^{-5}$ | $1 \cdot 10^{-5}$ | 13 hr 36 min |
| Test 8 | $1 \cdot 10^{-5}$ | $1 \cdot 10^{-7}$ | 25 hr 25 min |
| Test 9 | $1 \cdot 10^{-7}$ | $1 \cdot 10^{-3}$ | 4 hr 3 min |
| Test 10 | $1 \cdot 10^{-7}$ | $1 \cdot 10^{-5}$ | 21 hr 16 min |
| Test 11 | $1 \cdot 10^{-7}$ | $1 \cdot 10^{-7}$ | 26 hr |

### 3.5.2 Effect of Error Tolerances

Convergence of the solution is also affected by the selected error tolerance values. There are two different tolerance values used by the time dependent solver: relative tolerance and absolute tolerance. Relative tolerance is a global property which is used for all state (dependent) variables and must be between 0 and 1. It is a unitless quantity. Absolute tolerance has the same unit as the corresponding state variable and can be a global value for all the state variables or set to different values for each of them. It is recommended to set the absolute tolerance to one to two orders of magnitude lower than the value of the corresponding state variable. At each time step, the solver computes the state variables and calculates the estimated error of the state variables. The inequality which must be satisfied to continue to the next step is expressed as:

$$Estimated\ Error \leq Rtol * Ab(Y) + ATol(Y) \tag{15}$$

Where $Ab(Y)$ is the absolute value of the vector of state variables $Y$, $Rtol$ is the relative tolerance, and $ATol$ is the absolute tolerance.

If the estimated error is greater than the acceptable error, which is calculated based on the selected tolerance values, the solver reduces the time step and repeats the computation. The default value for the relative tolerance is $1 \cdot 10^{-3}$ which is suitable for most cases. However, it is recommended to use different values of tolerance and compare the accuracy and computation time. Higher tolerance values can decrease the computation time at the expense of the accuracy which might cause a convergence issue. Whereas, a lower tolerance value results in an increase in accuracy while making the simulation excessively slow.

The absolute or relative tolerance can become the dominating term for the estimated error depending on the relative values of the tolerances and magnitudes of the state variables. One way to check whether an accurate result is achieved with the selected tolerance value is to repeat the simulation with 10 times lower tolerances. If the new result is not significantly different than the previous, then one can trust the accuracy of the solution.

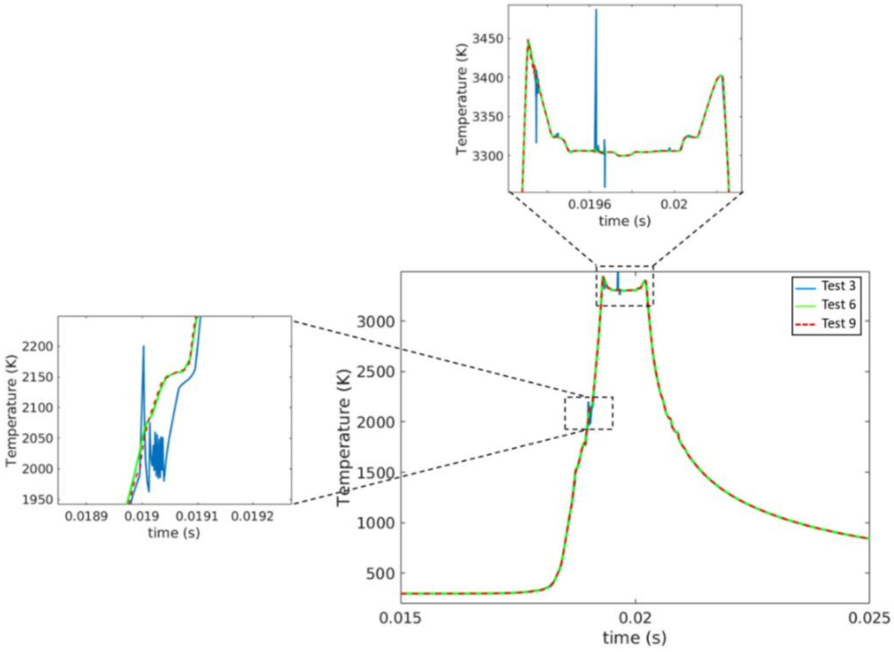

**Figure 3.7:** The thermal history with varying error tolerance is depicted for select tests. A convergence problem appears at the solution for Test 3 with the high tolerances.

**Table 3.4:** Effect of Domain Size on the Solution Accuracy and the Computation Time

| Domain Size (mm) (Length-Width-Height) | Computation Time | Melt Pool Size (μm) (Length-Width-Depth) | HAZ Size (μm) (at 1255 K) (Length-Width-Depth) |
|---|---|---|---|
| Small<br>3.5x0.5x0.23 | 3 hr 55 min | 150-144-52 | 269-232-100 |
| Medium<br>5.5x1.25x1.03 | 4 hr 3 min | 151-144-52 | 275-238-102 |
| Big<br>7.5x2.25x2.03 | 4 hr 16 min | 151-144-52 | 275-238-102 |

In the present study, the performance of the simulation was analyzed using different tolerance values. Table 3.3 represents a set of different tolerance values and their corresponding computation time requirement. As seen in the table, larger tolerances show convergence problem and simulation is stopped. Figure 3.7 shows the thermal history results from the simulations with different tolerance values. As seen in the figure, when the tolerance values are increased, the simulation speeds up. However, a convergence problem is shown in Figure 3.7 for Test 3. Decreasing the tolerance leads to an increase in the accuracy while slowing down the simulation. In the present study, Test 9 was selected which gives an accurate solution with reasonable computation time. The tolerance values for Test 6 provided similar solution accuracy and computation time as Test 9. One can consider the high computation time requirement for the higher tolerance values (e.g., Test 2), contradicting with the general knowledge. However, this can be explained as follows. When excessively high tolerance values are employed, the solver is not able to converge. Therefore, the time step is reduced automatically until the convergence is reached. This reduction in the time step causes the computation time to increase.

### 3.5.3 Effect of Domain Size

The substrate used in the LPBF experiment has the dimension of 10×10×1 cm. To reduce the computation time, in the simulations we used a relatively smaller substrate. LPBF experiments are conducted under room temperature. Therefore, it is plausible to set all the boundary conditions except the top boundary (as explained in Section 3.1) of the simulation domain to room temperature. However, if the substrate size used in the simulation is too small, then the solution will be affected by the chosen boundary conditions. To check whether the substrate size is sufficient, a set of simulations with increased substrate size are performed and the change in the cooling rates and the melt pool size are compared. As seen in Figure 3.8, when a domain size of 3.5×0.5×0.2 mm is selected (small domain) the cooling rate increases due to the influence of the boundary condition. In addition, a relatively smaller melt pool and Heat Affected Zone (HAZ)-defined by the region with the temperature greater than the β transition temperature of 1255 K [120]- size is obtained compared to the medium and big domain solutions shown in Table 3.4. When a medium domain with the dimensions of 5.5×1.25×1.03 mm is used, the cooling rate is slower and the melt pool/HAZ size is larger. There is no significant difference in the results for medium and big domain (7.5×2.25×2.03 mm) cases, which implies that the medium domain is sufficient for accurate results. A further increase in the domain size does not improve the accuracy of the solution, although the computation time is increased.

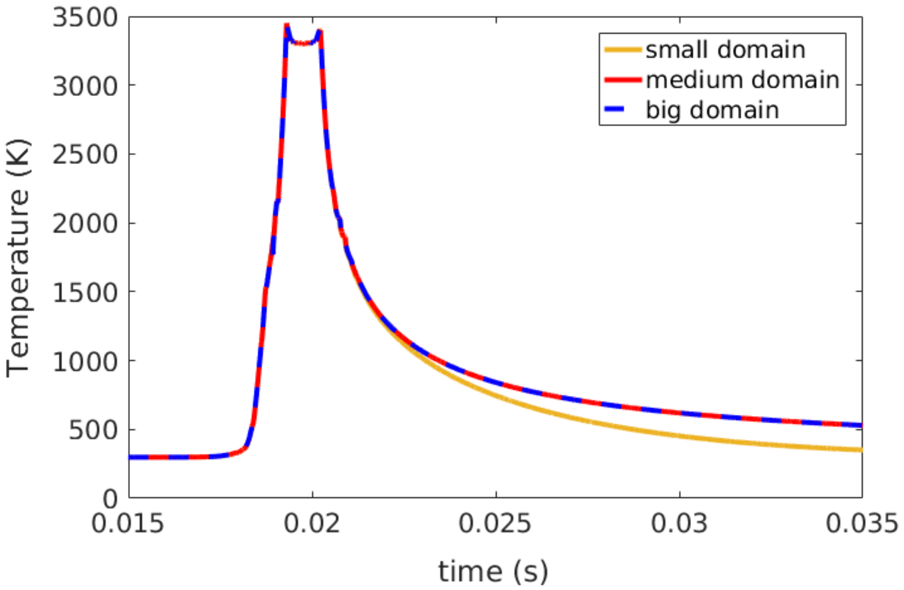

**Figure 3.8:** Thermal history plots for different domain sizes. Note the high cooling rate at small domain indicating the interference of the boundary conditions.

### 3.5.4 Code-to-Code Verification

Three case studies were devised to conduct code-to-code verification: (1) localized heat source, (2) moving heat source (single-track), and (3) moving heat source (three-tracks). The predicted melt pool sizes and thermal histories were compared. The importance of incorporating temperature dependent material properties, phase transitions and evaporation in the thermal modeling of LPBF process is demonstrated.

#### 3.5.4.1 Case Study 1 (Localized Heat Source)

In this study, the heat source is applied to a fixed point on the surface of the powder. The focus here is to investigate the heating and subsequent cooling process. Since the heat source does not move, a relatively small simulation domain is found sufficient in this study. The substrate has the form of a square block depicted in Figure 3.9 with the edge length of 1 mm, while the thickness of the powder layer is set to 200 µm. The boundary condition for the bottom of the domain is set to room temperature (298 K), while an adiabatic boundary condition is used for the sides of the domain. Both radiation and convection are used for the top surface of the domain. Evaporation is neglected in this study.

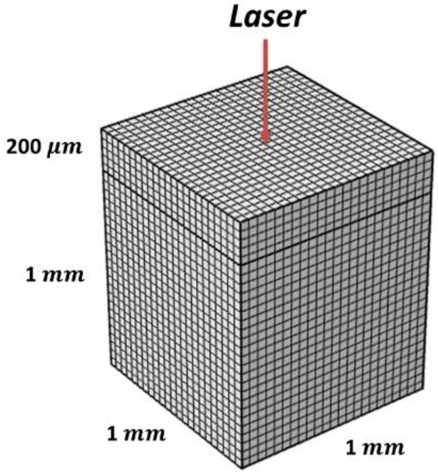

**Figure 3.9:** Block Geometry (Localized heat source is directed to the center of the top surface)

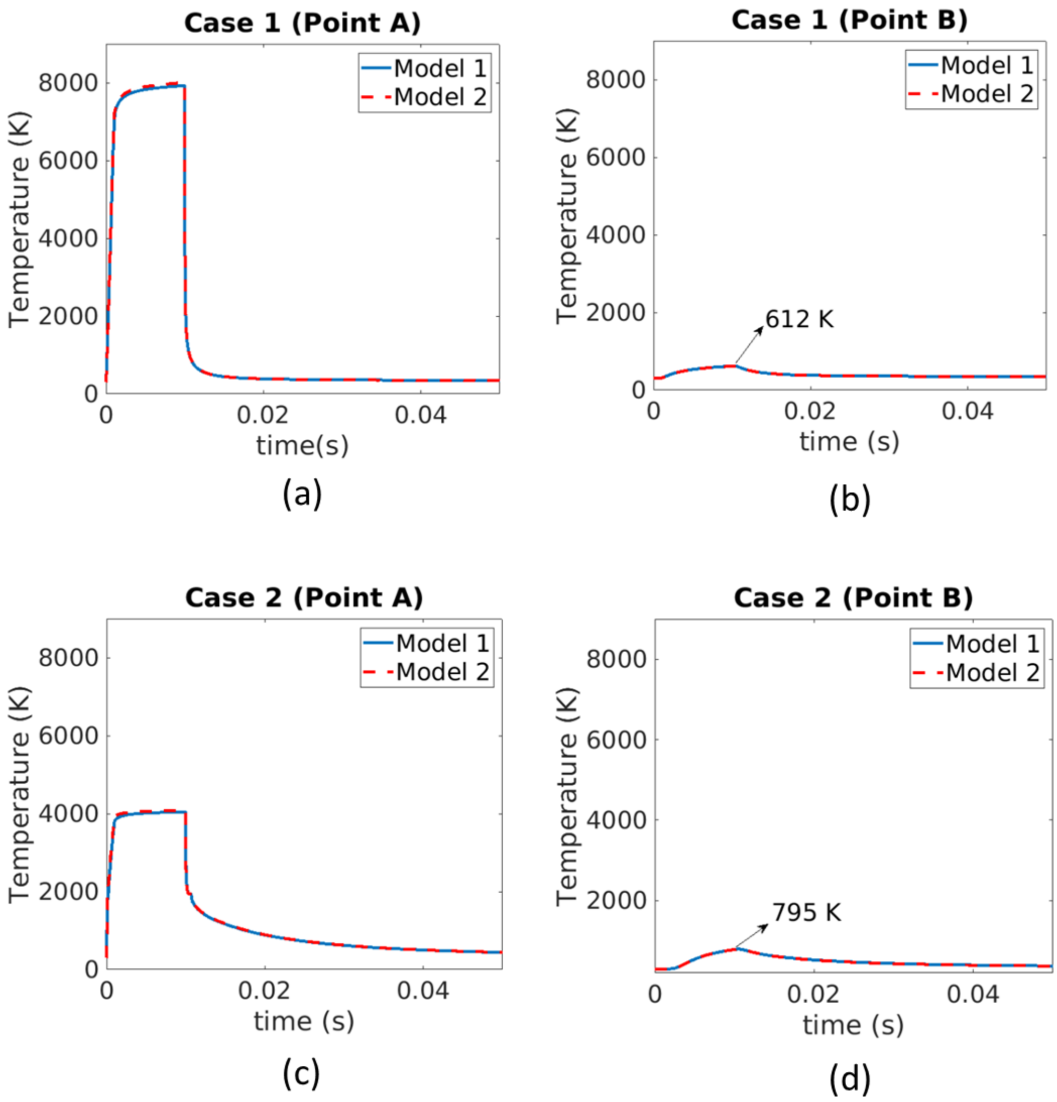

(a) (b)

(c) (d)

**Figure 3.10:** Excellent agreement between the two models is achieved for Case Study 1. Note the decrease in the peak temperatures in case 2 with temperature dependent material properties and phase transition between solid and liquid.

Two different cases are investigated: case 1 with constant thermo-physical properties and no phase transition between solid-liquid, case 2 with temperature dependent thermo-physical properties and phase transition between solid-liquid. The laser power is set to 15 W. Constant properties used in Case 1 are as follows: thermal conductivity, density, and specific heat are $15\,\text{W/m.K}$, $3000\,\text{kg/m}^3$, $700\,\text{J/kg.K}$, respectively. Temperature dependent properties used in case 2 are represented in Figure 3.4. Thermal history at two different locations – point A (at top center of the powder layer) and point B (at bottom center of the powder layer) are monitored for both cases. As seen in Figure 3.10, excellent agreement between the two models is achieved. There is a decrease in the peak temperature from 8000 K in case 1 to 4000 K in case 2 when the temperature dependent material properties and phase transition between solid and liquid are applied. Considering the boiling temperature of Ti-6Al-4V which is 3315 K, the peak temperature of 8000 K is highly unphysical. This strongly suggests temperature dependent material properties and phase transition significantly impact the solution and should be considered in thermal modeling of the LPBF process. Note that the evaporative heat loss was neglected in this case. Therefore, the peak temperature of 4000 K is reasonable. The effect of evaporation will be shown in the next case study.

#### 3.5.4.2 Case Study 2 (Single-Track Laser Melting)

In this case study, single-track laser melting is simulated. A rectangular block consisting of a layer of powder on the substrate used in this simulation is illustrated in Figure 3.2 (a) and Figure 3.3 (a), respectively for Model 1 and Model 2. The red dot which is in the middle of the track represents the position of the point where the thermal histories are measured in Model 1 and Model 2 as shown in Figure 3.2 (c) and Figure 3.3 (b), The laser power, laser speed, and the track length are listed in Table 3.1. Note that the track

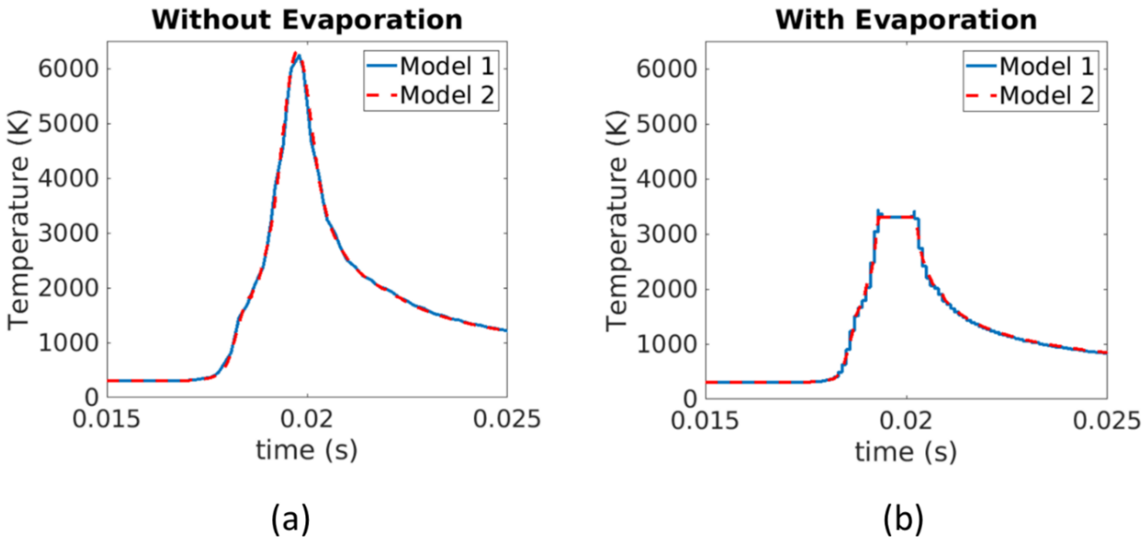

**Figure 3.11:** Predicted thermal histories from both models are presented for Case Study 2. Reduction on the maximum predicted temperature due to evaporation is clearly seen on the plots.

**Table 3.5:** Predicted Melt Pool Sizes for Case Study 2

| | **Melt Pool Sizes (μm)** | |
|---|---|---|
| | **Without Evaporation** | **With Evaporation** |
| **Model 2** | 275x237x76 | 146x141x51 |
| **Model 1** | 270x234x75 | 149x144x52 |

length of 3 mm was sufficient to reach steady state at which the melt pool size remains unchanged during the transient simulation. Initially, heat loss due to evaporation was neglected and the results were compared. Agreement between the two models was achieved, and the thermal histories at point A are depicted in Figure 3.11 (a). However, the predicted maximum temperature of approximately 6000 K is much higher than the boiling temperature of the selected material (3315 K). Therefore, next step was to incorporate the heat loss through evaporation. This was achieved by implementing a simple evaporation technique as described in Section 3.1. As seen in Figure 3.11 (b), the maximum temperature was successfully reduced to around the boiling temperature in both models. Depending on this cooling effect, the melt pool sizes were also reduced in both models. Table 3.5 lists the predicted melt pool sizes without and with evaporation for both models. Overall, a very good agreement in the results was achieved.

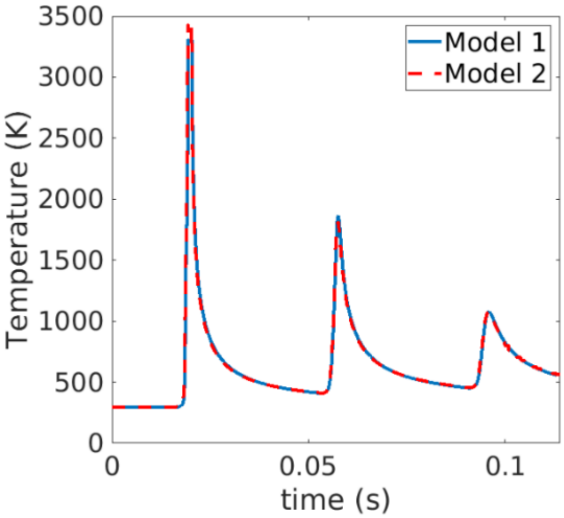

**Figure 3.12:** Predicted thermal histories from both models for Case Study 3 are presented. The thermal histories are measured at the point A, as shown in Figure 2 (d) and Figure 3 (b), respectively for Model 1 and Model 2.

#### 3.5.4.3 Case Study 3 (Multi-Track Laser Melting)

In this study, multi-track laser melting was simulated to investigate the subsequent heating and cooling process. Rectangular block geometry and the laser scanning path were illustrated in Figure 3.2 (b) and (d). Evaporation was taken into account in both models. The process parameters and the material properties were the same as the single track simulations. The hatch spacing between subsequent tracks was set to 70 µm. The thermal history at point A located in the middle of the first track was monitored in both models as shown in Figure 3.2 (d) and Figure 3.3 (b). As seen in Figure 3.12, the selected location experienced multiple heating-cooling cycles with descending peak temperatures during the scanning of three tracks. The temperature of the first peak was predicted around 3315 K in both models and indicates that there was heat loss due to evaporation. The small difference in the first peak temperature between Model 1 and Model 2 is due to the different convergence criteria utilized. Additional refinement of the error convergence control is expected to reduce the difference in the first peak temperature between the models. More discussion on the effect of error tolerance can be found in Section 4.2. The peak temperatures during scanning of subsequent tracks agreed well and were predicted around 1860 K and 1060 K in both models. This indicates that the material was exposed to re-heating without melting during laser scanning of second and third tracks.

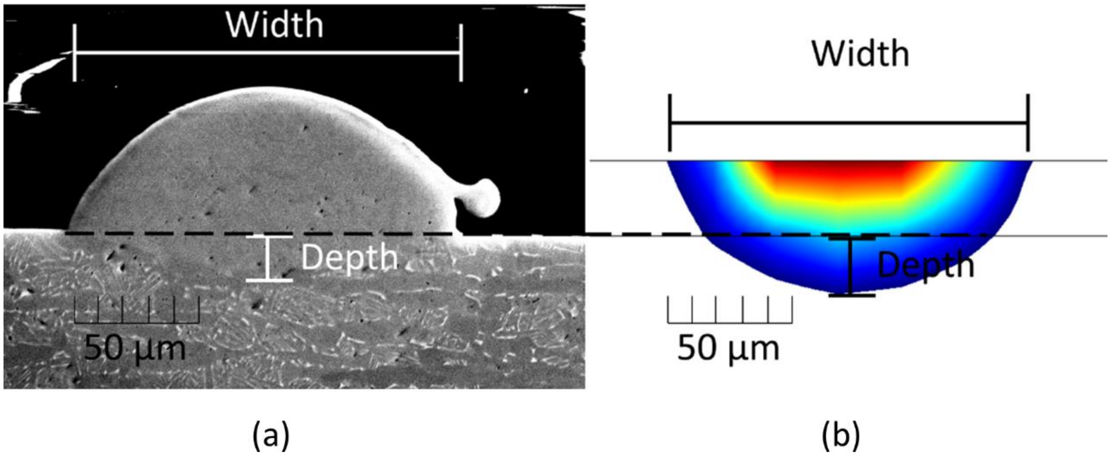

**Figure 3.13:** Comparison of experimentally measured melt pool sizes (width and depth in the substrate) with the predicted values. The melt pool width and depth in the substrate were measured as 161.8±10.87 µm and 18.2±7.66 µm (a), indicating 11 % and 20.9% errors with the predicted values of 144 µm and 22 µm (b), respectively.

### 3.6 Model Validation

Validation experiments were conducted on a commercial LPBF system: ProX 100 DMP by 3D Systems. The system is equipped with a laser beam with maximum power of $P$=50 W and beam spot diameter of $D$=70 µm**.** Ti-6Al-4V was used for both powder and substrate plates.

To validate the simulation models, the melt pool width and depth in the substrate were experimentally measured and compared with model predictions. Single-track deposits with track length of 3 mm were made on a solid substrate from the same material. The thickness of the powder layer was 30 µm. The power and scanning speed were set to

50 W and 80 mm/s, respectively. Electrical discharge machining (EDM) was used to cut cross sections of the deposits, which were then embedded in epoxy resin and polished. Afterwards, the images of the cross sections were taken using Tescan Fera-3 SEM with the backscattered electron (BSE) detector.

Figure 3.13 represents a comparison of experimentally measured and predicted melt pool width and depth in the substrate. In the figure, the melt pool prediction is shown for Model 1. The melt pool width and depth in the substrate were measured as 161.8±10.87 μm and 18.2±7.66 μm, indicating 11% and 20.9% errors with the predicted values of 144 μm and 22 μm from Model 1. Similar comparisons for Model 2 indicated 12.8% and 15.3% errors with the predicted values of 141 μm and 21 μm for the melt pool width and depth, respectively. Reasonable agreement with the experimental measurements was obtained for both models. The predictions from both models showed slightly smaller melt pool width and larger melt pool depth in the substrate, which can be explained by the negligence of the Marangoni convection in the models.

### 3.7 Summary and Conclusion

In the present work, a V&V study for thermal modeling of LPBF processes was presented. In particular, the focus was on the code-to-code *Verification* assessments, which went unheeded in the existent literature. To this end, two different finite element-based thermal models were developed and implemented in two different platforms (Comsol Multiphysics® and Sierra Mechanics). The same process parameters, material properties and physics were used in both models, while the numerical implementation and the modeling parameters such as mesh size, mesh type or error tolerances used in the models were set differently. Three case studies were devised to conduct code-to-code verification: (1) localized heat source, (2) moving heat source (single-track), and (3) moving heat source (three-tracks). The predicted melt pool sizes and thermal histories in both models were compared. Overall, an excellent agreement in the results was achieved. The importance of incorporating temperature dependent material properties, phase transitions and evaporation in the thermal modeling of the LPBF process was demonstrated. In addition, the influences of mesh size, domain size, and error tolerance on the accuracy of the results as well as the trade-off between the accuracy and the computational cost were discussed. Finally, the predicted melt pool sizes were compared with those experimentally measured and reasonable agreements were achieved.

# 4. FINITE INTERFACE DISSIPATION PHASE FIELD MODELING OF NI-NB UNDER ADDITIVE MANUFACTURING CONDITIONS

## 4.1 Overview

During the laser powder bed fusion (LPBF) process, the material undergoes multiple rapid heating-cooling cycles, leading to complex microstructures with nonuniform properties. In the present work, we employed a computational framework, which couples a finite element thermal model to a non-equilibrium phase field model to investigate the rapid solidification microstructure of a Ni-Nb alloy during LPBF. The framework is utilized to predict the spatial variation of the morphology, size, and microsegregation in the single-track melt pool microstructures obtained under different process conditions. A planar to cellular transition was predicted in the majority of keyhole mode melt pools, while a planar interface was predominant in the conduction mode melt pools. The predicted morphology and size of the solidification features agreed well with the experimental measurements. Finally, a solidification map demonstrating the variation of the microstructural features as a function of the laser processing parameters was presented.

## 4.2 Introduction

During Additive manufacturing (AM) refers to the technologies in which three dimensional objects are created by adding materials layer-by layer [147, 148]. A number of AM processes has been developed over the past decades. Among them, laser powder bed fusion (LPBF), a powder-based AM process, has attracted much attention due to its ability to produce fully dense parts with improved properties. During this process, the material undergoes multiple rapid heating-cooling cycles, leading to complex solidification microstructures with anisotropic properties. Typically, post-processing heat treatments are performed to homogenize and control the LPBF microstructures. However, it is also possible to control the as-deposited microstructure by tailoring the process parameters, which in turn can reduce the cost and time needed for post-processing and thus facilitate the qualification process. Therefore, it is essential to develop an understanding of the influence of the process parameters on LPBF solidification microstructure [147]. Once the solidification microstructure is expressed as a function of process parameters, the knowledge can be used to aid the design of AM materials to obtain desired properties.

Numerical modeling of the solidification microstructure has been performed using various methodologies [29, 149-153]. A thorough discussion on solidification microstructures and simulation methods can be found elsewhere [151, 154-157]. A number of simulation methods have been adopted in the literature to investigate the solidification microstructure of AM parts. Korner et al. [158] studied the equiaxed and columnar grain structures during electron beam melting (EBM) of IN718 using Lattice Boltzmann (LB) method and experimental techniques. It was demonstrated that the grain structure can be tailored from columnar to equiaxed using different scanning strategies. Markl et al. [135] developed a model by coupling LB and cellular automata (CA) methods to investigate the evolution of grain structure during EBM of Ti-6Al-4V. The predicted thermal history in LB model was fed into CA model to predict the grain structure. It was demonstrated that at a low power, stray grains were formed due to incomplete melting. Nie et al. [159] predicted solidification microstructure during laser AM of a nickel-based superalloy using a multi-scale modeling approach that couples finite element (FE) method and stochastic analysis. The model was used to investigate the evolution of dendritic structure, niobium (Nb) segregation, and formation and morphology of the Laves phase. It was demonstrated that the morphology of the Laves phase, which is an undesired phase, was influenced by the cooling rate. As the cooling rate increased, the morphology of the Laves phase changed from a coarse and chain-like structure to a fine and discrete structure, which is considered to be less detrimental. Lopez-Botello et al. [160] employed a CA-FE model to investigate the grain structure (equiaxed vs. columnar) during LPBF of aluminum alloys.

Recently, the phase field (PF) method has attracted much attention in investigation of solidification microstructure that results during an AM process [161, 162]. It is a promising approach with the ability of describing complex microstructural evolution without needing to track the moving interface, as opposed to the classical sharp interface models [28, 163-166]. The phase field model, also called ‘diffuse interface model’, assumes the interface between phases to have a finite thickness, in contrast to the sharp interface assumption. The phase field variable in these models is used to describe the relative amount of a phase and is a state variable with values span in space and time. It varies smoothly along the interface with each phase having a constant value. For example, in a system with solid-liquid interface, the phase field variable takes the value of 0 in the solid phase, 1 in the liquid phase, and a value between 0 and 1 in the interface.

It has been proven that by the coupling of PF method with a FE thermal model, quantifiable predictions of the solidification phenomenon during AM can be achieved. Acharya et al. [35] employed a computational fluid dynamics (CFD) model coupled with a PF model to simulate the microstructure evolution during LPBF of IN718, which was approximated as a binary alloy. The authors investigated the dendritic structure (size, morphology, and orientation), segregation of Nb, primary dendrite arm spacing (PDAS) and secondary dendrite arm spacing (SDAS). The influence of laser speed on the orientation of dendritic structure was also investigated. Keller et al. [167] investigated the evolution of cellular/dendritic structure and micro-segregation in IN625 alloy during LPBF process using multiple computational techniques including DICTRA simulation, Scheil-Gulliver model, PF model, and FE-based thermal model. Micro-segregation of multiple substitutional elements (e.g. Nb, Mo, Fe, Cr) were predicted using DICTRA software and Scheil-Gulliver model. Both approaches showed an increase in Nb, Mo, C and a decrease in Fe and Cr at the growth front of $FCC_{\gamma}$ cells during solidification. The microsegregation of Nb element was further investigated using a PF model with an approximation of IN625 alloy to a binary alloy system with the composition of Ni-4 wt.% Nb. In this work, the predicted PDAS varied between 0.2 μm and 1.8 μm depending on the cooling rate, in the range of $10^4$ K/s-$10^6$ K/s calculated using a FE model. Ghosh et al.

[36, 168] employed a coupled FE-PF model to simulate the solidification microstructure of a Ni-5 wt.% Nb alloy (a binary approximation of IN718 alloy) during the LPBF process. Varying values of temperature gradient (G: $2.4\times10^7$ K/m-$0.14\times10^7$ K/m) and growth rate (R: 0.01 m/s - 0.3 m/s) were predicted by the FE model and fed into the PF model to investigate the PDAS and Nb enrichment at different conditions. Predicted PDAS ranged from 0.2 μm to 0.7 μm as the cooling rate decreased from $10^6$ K/s to $3\times10^5$ K/s. Nb segregation in the interdendritic region was predicted as 16 wt. %. Similar studies in which the solidification microstructure under AM conditions was simulated using a number of different PF models can be found in the literature [145, 169].

Note that, the aforementioned phase field works were based on the equal diffusion potential condition (the local equilibrium condition). During a typical LPBF process, the system is out-of-equilibrium due to the extremely high solidification growth rates. Therefore, a novel phase field model with the capability of describing the rapid solidification phenomenon under LPBF conditions is required. Recently, Steinbach et al. [170, 171] proposed a phase field model, namely, the finite interface dissipation model, in which both the equilibrium and strongly non-equilibrium conditions are successfully described. The novelty of this model is that the rate of transportation of the components between the phases can be controlled with a kinetic coefficient, namely, "interface permeability", $P^{intf}$. The value of the interface permeability can be chosen (i.e. $P^{intf} \rightarrow 0$) such that the large non-equilibrium case can be modeled. In contrast, when $P^{intf} \rightarrow \infty$, the condition of equal diffusion potential in the conventional models (system with local equilibrium condition) can be recovered. To account for the non-equilibrium solidification effects observed during the LPBF process, the finite interface dissipation phase field model is adopted in the present work.

It is a common practice to describe the multi-component alloys using a binary approximation due to the complexity of implementing the phase field model for multi-component systems. Although this is a reasonable approach to simulate the microstructure of complicated technical alloys consisting of a number of constituent elements (e.g. Inconel 718 with 15 constituent elements), it will introduce uncertainties associated with the model assumptions. NiNb has been widely used as a binary approximation for Ni-based superalloys such as Inconel 718 [35, 36] and Inconel 625 [167]. Although the Nb percent in the binary modeling material is the same as that exists in the approximated multi-component alloy (e.g. 5 wt. % Nb in Inconel 718), it is evident that there will be contribution of other constituent elements (e.g., Cr, Fe, Mo, Al) in the formation of microstructure phases in the aimed multi-component alloy, which might influence the accuracy of the comparison with the binary phase field model predictions. The present work, on the other hand, provides a consistent framework by adopting a Ni-5 wt. % Nb (Ni-3.2 at. % Nb) alloy in both phase field model and validation experiments. We believe that the use of a simple binary alloy will eliminate the complexity and uncertainty associated with the microstructure evolution, which is a serious concern in the AM community [172]. Indeed, the recent modeling and experimental efforts of AM have adopted various binary alloy systems (e.g., Ti-Nb [173], Al-Cu [174], Al-Si [174]) to elucidate the solidification microstructure developed under AM conditions.

It is worthwhile to mention that the finite interface dissipation phase field model adopted in the present work is well suited for describing multi-phase multi-component systems. Very recently, this model was employed in [175]to investigate the solidification microstructure of Fe-Cr-Ni-Mo-C and stainless steels under AM conditions. The authors emphasized the capability of the model in simulating the solidification microstructure for multi-component systems in high temperature gradient and growth rate. Note that the present work differs from the aforementioned study due to the implementation of FE-PF coupled framework and rigorous experimental validation. The main goal of the present work is to present a consistent framework which can be used to elucidate the influence of the process parameters on the variabilities in Ni-Nb solidification microstructure during single-track laser melting. Once the microstructure variabilities in a simple binary alloy during single-track experiments are well understood, the next step would be employing the presented framework to investigate more complex alloying systems (e.g. Inconel 718) under multi-track multi-layer laser melting conditions.

Current PF modeling efforts in the AM literature [168, 173, 176] typically demonstrate the microstructure predictions (e.g. morphology, size, segregation) as a function of G and R. A significant insight on the solidification microstructures under AM conditions have been revealed through these types of investigations. However, it is known that the AM microstructures vary locally in a single melt pool under constant process parameters as well as from melt pool to melt pool depending on the variation of G and R. Therefore, these types of studies fall short of elucidating the relationship between the process parameters and the microstructure variabilities. In this regard, solidification maps demonstrating AM solidification microstructure as a function of process parameters (e.g. laser power P and scan speed V) are essential to understand and control the microstructure variabilities under AM conditions.

In the present work, we developed an integrated modeling framework which couples a finite element (FE) based thermal model to a finite interface dissipation phase-field (PF) model to investigate the rapid solidification microstructure during single track laser melting of a binary Ni-5 wt. % Nb (Ni-3.2 at.% Nb) alloy. First, the thermal history of the material will be predicted by the FE simulations which will then be introduced into the PF model to predict the rapid solidification microstructure (e.g. the morphology, size, and Nb segregation) under L-PBF conditions. To reveal the effect of process parameters on the microstructure variabilities, first, a conventional solidification microstructure map expressing the rapid solidification microstructure as a function of G and R is developed. Next, the microstructure predictions in multiple regions across the melt pool for sets of P and V are shown and compared with the experimental measurements for validation purpose. Finally, a solidification microstructure map representing the microstructural variabilities as a function of P and V is demonstrated.

The paper is structured as follows. In Section 2, the experimental methodology is described. Section 3 describes the models and procedures. Section 4 presents the experimental measurements, simulation predictions, and discusses the effect of process parameters on the LPBF microstructures. Finally, Section 5 summarizes and addresses the future directions.

## 4.3 Experimental Methodology

Gas atomized Ni-5wt.%Nb powder provided by Nanoval GmbH & Co. KG was used to manufacture LPBF NiNb specimens. Single tracks were printed using a 3D Systems ProX DMP 200 Laser Type (fiber laser with a Gaussian profile $\lambda$= 1070 nm, and beam size = 100 µm). The tracks were printed on a Ni-5wt.%Nb base plate. These tracks were 10 mm in length with 1 mm spacing between tracks. Cross-sections of the single tracks were wire cut using wire electrical discharge machining (EDM), and these specimens were polished down to 0.25 µm with water-based diamond suspension polishing solutions. Kalling's Solution No. 2 (5 g CuCl2, 100 mL HCl, and 100 mL ethanol) was used to etch the Ni-5wt.%Nb single tracks to obtain optical micrographs.

Optical microscopy (OM) was carried out using a Keyence VH-X digital microscope equipped with a VH-Z100 wide range zoom lens. Scanning electron microscopy (SEM) and wavelength dispersive spectroscopy (WDS) were performed with a CAMECA SXFive electron probe microanalyzer equipped with a LaB6 electron source. Backscattered electron (BSE) images of polished single tracks were captured at 15 kV and 30 nA. Quantitative WDS composition maps were obtained at settings of 15 kV, 100 nA, and 110 µm pixel dwell time with a 0.1 µm step size. Composition data was extracted from the WDS maps to create line scans for visual aid purposes. BSE images were processed using Image J © software in order to determine PDAS at different locations along select single tracks. The displayed PDAS values were averaged from 30 measurements at each location.

## 4.4 Model Description

### 4.4.1 Thermal Model

The thermal history during the LPBF process can be determined by numerically solving the transient heat transfer equation given by:

$$\rho C_p \frac{\partial T}{\partial t} + \nabla(-k\nabla T) = Q \tag{4.1}$$

where $\rho$ is the density, $C_p$ is the specific heat, $k$ is the thermal conductivity, $T$ is the temperature, $t$ is the time, and $Q$ is the heat source term. This basic form of the heat transfer equation describes the transient evolution of temperature $T$ and is typically modified to account for additional physical phenomena that serve to increase the accuracy of the predictions. Examples of such phenomena are phase transformation energy contributions and temperature dependent material properties. In this model, we include both of the aforementioned phenomena and also perform a coordinate transformation:

$$\frac{\partial T}{\partial t} = \frac{\partial T}{\partial x}\frac{\partial x}{\partial t} + \frac{\partial T}{\partial y}\frac{\partial y}{\partial t} + \frac{\partial T}{\partial z}\frac{\partial z}{\partial t} = \nabla T \cdot V \tag{4.2}$$

Substituting Equation 4.2 into Equation 4.1 eliminates the transient portion of the governing heat transfer equation and shifts the reference frame from the material substrate to the heat source which is moving at a constant speed *V*.

$$\rho C_p (\nabla T \cdot V) + \nabla(-k\nabla T) = Q \tag{4.3}$$

The effect of this transformation is the conversion of the transient problem to a steady-state simulation, which is a much simpler problem that results in several orders of magnitude decrease in simulation time. This simplification in the governing equations opens up the possibility to use a very fine finite element mesh size (2 μm) in and around the melt pool, which is essential for the accurate prediction of solidification properties at the solid-liquid interface. A schematic of the finite element domain and the representative heat affected region can be seen in Fig. 4.1.

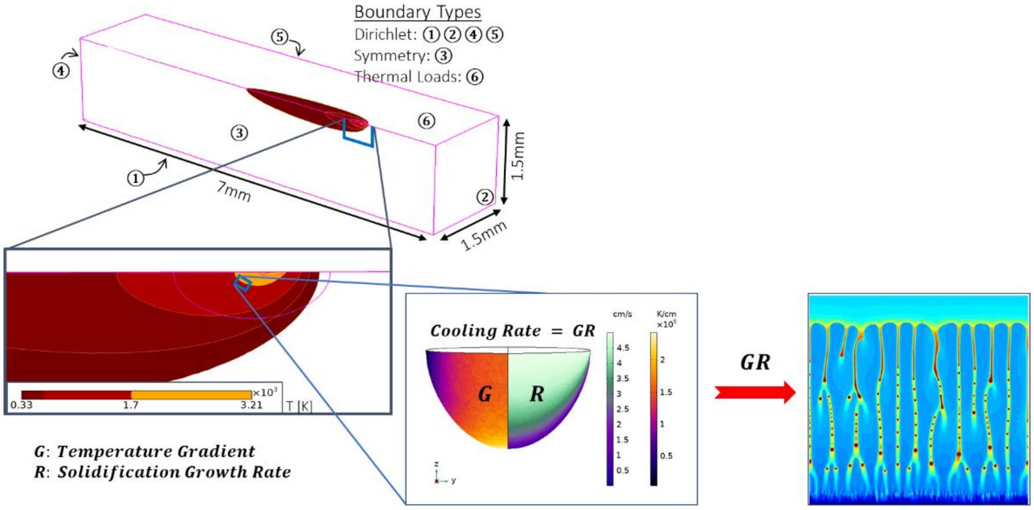

**Figure 4.1:** The coupling of the thermal model with the phase field model is illustrated. An example of predicted heat affected region of Ni-5wt.%Nb alloy during LPBF is presented on the three-dimensional thermal model geometry. The temperature gradient *G* and growth rate *R* are extracted from the thermal model and fed into the phase field model to predict the microstructure at the corresponding location at the melt pool indicated by a small rectangle in the magnified view of the heat affected region.

Boundary conditions for this model can be broken down into three categories: Dirichlet, Symmetry, and Thermal Loads. Boundaries 1, 2, 4, and 5 are Dirichlet boundary conditions with a fixed temperature of $T_0$=298 [K]. A symmetry condition imposed on the centerline of the track (Boundary 3) essentially halves the computational expense of the simulation. The top surface (Boundary 6) contains all of the heat transfer phenomena that contribute to the source term $Q$ in Equation 4.3.

$$Q = q_{rad} + q_{conv} + q_{vap} + q_{beam} \tag{4.4}$$

$$q_{radiation} = \varepsilon \sigma_{\mathrm{B}} (T_{amb}^4 - T^4) \tag{4.5}$$

$$q_{convection} = h(T_{amb} - T) \tag{4.6}$$

$$q_{vap} = L_v \sum_{i=1}^{n} X_i 44.331 p_i(T) \sqrt{(MW_i)/T} \tag{4.7}$$

$$q_{beam} = a(T)P \left[ \frac{1}{2\pi\sigma^2} e^{\left(-\frac{(r-r_0)^2}{2\sigma^2}\right)} \right] \tag{4.8}$$

Equations 5-8 describe surface radiation, natural surface convection, vaporization, and deposited beam power, respectively. The radiation, convection, and beam terms are commonly implemented in the finite element modeling of LPBF. Evaporative energy loss $q_{vap}$ accounts for energy transferred out of the system in the form of mass transfer via hot vapor. The form of this equation is taken from Bolten-Block and Eagar [177] and modified to include temperature dependent partial pressure relationships for each element.

**Table 4.1:** Thermophysical and processing parameters used in the FE thermal model. All thermophysical property values were calculated using a weighted average of the pure elemental properties of Ni and Nb.

| Phase Properties | Values | Sources |
|---|---|---|
| **Solid** | | |
| $p_s$ | 8900 [kg/m$^3$] | |
| $k_s$ | 85 [W/$mK$] | |
| $c_{ps}$ | 550 [J/kg$K$] | |
| $a_s$ | 0.3 [unitless] | |
| **Solid-Liquid** | | |
| $T_m$ | 1703 [K] | |
| $\Delta T_m$ | 50 [K] | |
| $L_m$ | $2.9(10)^5$ [J/kg] | |
| **Liquid** | | |
| $p_L$ | 8450 [kg/m$^3$] | |
| $k_L$ | 120 [W/$mK$] | |
| $Cp_L$ | 650 [J/kg$K$] | |
| $a_L$ | 0.3 [unitless] | |
| **Liquid –Vapor** | | |

| | | |
|---|---|---|
| $T_v$ | 3209 [K] | |
| $\Delta T_v$ | 200 [K] | |
| $L_v$ | $7.1(10)^6$ [J/kg] | |
| **Vapor** | | |
| $p_v$ | Temp. Dep. | |
| $k_v$ | 1000 [W/$mK$] | |
| $Cp_v$ | Temp. Dep. | |
| $a_v$ | 0.6 [unitless] | |
| $p_i$ | Temp. Dep | |

| **Constants** | **Values** | **Source** |
|---|---|---|
| **Laser** | | |
| $P$ | 70-255 [W] | |
| V | 50-2300 [mm/s] | |
| $4\sigma$ | 70 [µm] | |
| **General** | | |
| $T_{amb}$ | 298 [K] | |
| $MW_{Ni}$ | 58.7 [g/mol] | |
| $MW_{Nb}$ | 92.9 [g/mol] | |
| $\varepsilon$ | 0.7 [unitless] | |

In general, the parameters in equations 4.3-4.8 can be sorted into temperature dependent and non-temperature dependent properties. Parameters considered to be constant are:

ambient temperature ($T_{amb}$), emissivity ($\varepsilon$), Stefan-Boltzmann constant ($\sigma_{\mathrm{B}}$), molecular weights of Ni and Nb ($MW_i$), laser power (P), beam standard deviation ($\sigma_{\mathrm{B}}$), and beam centerpoint ($r_0$). The group of temperature dependent material properties include: partial pressure ($p_i$), density ($\rho$), specific heat ($C_p$), thermal conductivity ($k$), and laser speed (V), and absorptivity ($a$). Phase dependent values for all of these properties can be found in Table 4.1. The natural convection coefficient ($h$) is calculated internally within COMSOL Multiphysics© [119] framework based on the domain geometry and orientation.

The phase-dependent property values in Table 4.1 are calculated using an average of the elemental properties for each constituent, weighted by the corresponding atomic percent. This rule-of-mixtures approximation is necessitated by the lack of experimental thermophysical property measurements for this custom NiNb alloy. A weighted average is sufficient in this case because the alloy is a very dilute single-phase solid-solution. In particular, the absorptivity values were chosen to approximate a recent study by Trapp et al. [178] which shows experimental evidence for low effective absorptivity of the solid/liquid phases and high effective absorptivity upon vaporization and keyhole formation. Additionally, a powder layer with effective material properties is not directly modeled due to the fact that its primary effect (increased laser absorptivity) is negligible at steady-state conditions when the laser is solely incident upon the solid, liquid and vapor phases.

Smooth transitions between the phase-dependent thermophysical property values in Table 4.1 are accomplished by averaging the properties of each phase based on their respective fractions during the transformation. Latent heat contributions for melting and vaporization ($L_m$ and $L_v$) are included in the model by adding the appropriate term directly to the heat capacity value during their respective transformations. Details of this effective property approach can be found in [179].

### 4.4.2 Phase Field Model with Finite Interface Dissipation

The phase field model with finite interface dissipation introduced by Steinbach et al. [170, 171] is adopted in the present work to investigate the rapid solidification process during LPBF of Ni-5 wt. % Nb (Ni-3.2 at. % Nb) alloy. The model has been proven to be capable of modeling non-equilibrium solidification behavior. Here, a brief description of the model is presented. The further details on full derivation can be found in the references provided above.

The derivation of a typical phase field model starts with the description of the free energy functional. The free energy functional has contributions from the chemical energy density ($f^{chem}$) and from the interface ($f^{intf}$).

$$F = \int_{\Omega} \left\{ f^{intf} + f^{chem} \right\} \tag{4.9}$$

$$f^{intf} = \frac{4\sigma_{\alpha\beta}}{\eta} \{ -\frac{\eta^2}{\pi^2} \nabla\phi_\alpha \cdot \nabla\phi_\beta + \phi_\alpha\phi_\beta \} \tag{4.10}$$

$$f^{chem} = \phi_\alpha f_\alpha(c_\alpha) + \phi_\beta f_\beta\left(c_\beta\right) + \lambda\{c - (\phi_\alpha c_\alpha + \phi_\beta c_\beta)\} \tag{4.11}$$

where, $\sigma_{\alpha\beta}$, $\eta$, $\phi_{\alpha/\beta}, c_{\alpha/\beta}, c$ are the interfacial energy, the interface width, the phase fractions of *α/β* phases, the phase concentrations of *α/β* phases, and the overall concentration, respectively. The summation of the phase fractions is 1 throughout the system with the relationship of $\phi_\alpha + \phi_\beta = 1$. $\lambda$ is the Lagrange multiplier, which is introduced to assure the solute conservation constraint given by: $c = c_\alpha \phi_\alpha + c_\beta \phi_\beta$. Note that, $\phi_{\alpha/\beta}, c_{\alpha/\beta}$ are the phase field variables, hence, function of space and time as follows: $\phi_\alpha(x,t), \phi_\beta(x,t), c_\alpha(x,t), c_\beta(x,t)$. However, we will be using the short forms of $\phi_\alpha, \phi_\beta, c_\alpha, c_\beta$ for simplification. $f_\alpha$and $f_\beta$ are the free energy densities of the corresponding phases and described within the CALPHAD formalism. At the selected alloy composition of $c_\alpha$=3.2 (at. % Nb), two phases (liquid and $\gamma$-FCC) can be described as:

$$f_\alpha = x_{Nb}^\alpha G_{Nb}^0 + (1 - x_{Nb}^\alpha) G_{Ni}^0 + RT(x_{Nb}^\alpha \ln x_{Nb}^\alpha + (1 - x_{Nb}^\alpha) \ln(1 - x_{Nb}^\alpha)) + x_{Nb}^\alpha (1 - x_{Nb}^\alpha) \sum_{i=0}^{n} G_i (2x_{Nb}^\alpha - 1)^i \qquad (4.12)$$

Here, $x_{Nb}^\alpha$ is the mole fractions of phase $\alpha$ (liquid or $\gamma$-FCC), described as $x_{Nb}^\alpha = \frac{c_\alpha}{V_m}$, in which $V_m$ represents the molar volume. $R$ and $T$ represent ideal gas constant and temperature, respectively. $G_{Nb}^0$, $G_{Ni}^0$ are reference states of constituent elements. $G_i$ terms are coefficients contributing to excess Gibbs energy. The determination of the coefficients (i.e. $G_{Nb}^0$, $G_{Ni}^0$ and $G_i$) are calculated through thermodynamic assessments [180].

The evolution equations of the phase concentrations, $c\alpha$ and $c\beta$, are derived through the variational principles. The final form of the evolution equations of the phase concentrations:

$$\phi_\alpha \dot{c}_\alpha = \nabla(\phi_\alpha D_\alpha \nabla c_\alpha) + P^{intf} \phi_\alpha \phi_\beta \left( \frac{\partial f_\beta}{\partial c_\beta} - \frac{\partial f_\alpha}{\partial c_\alpha} \right) + \phi_\alpha \dot{\phi}_\alpha (c_\beta - c_\alpha) \tag{4.13}$$

$$\phi_\beta \dot{c}_\beta = \nabla(\phi_\beta D_\beta \nabla c_\beta) + P^{intf} \phi_\alpha \phi_\beta \left( \frac{\partial f_\alpha}{\partial c_\alpha} - \frac{\partial f_\beta}{\partial c_\beta} \right) + \phi_\beta \dot{\phi}_\beta (c_\alpha - c_\beta) \tag{4.14}$$

where $D_\alpha$ and $D_\beta$ are the chemical diffusivities in the $\alpha$ and $\beta$ phases, respectively, and $P^{intf}$ is the interface permeability defined as: $P^{intf} = \frac{8M}{a\eta}$. Here, $M$ is the atomic mobility and $a$ is the lattice constant. Further information on the physical meaning of the interface permeability, $P^{intf}$, can be found in the referenced papers [171, 181].

Similarly, the evolution equations of the phase fractions, $\phi_\alpha$ and $\phi_\beta$, are derived through the variational principle. The final evolution equation for the phase fraction $\phi_\alpha$ is:

$$\dot{\phi}_\alpha = K \left\{ \sigma_{\alpha\beta} \left[ \nabla^2 \phi_\alpha + \frac{\pi^2}{\eta^2} \left( \phi_\alpha - \frac{1}{2} \right) \right] - \frac{\pi^2}{8\eta} \Delta g_{\alpha\beta}^{phi} \right\} \tag{4.15}$$

$$K = \frac{8P\eta \mu_{\alpha\beta}}{8P\eta + \mu_{\alpha\beta} \pi^2 (c_\alpha - c_\beta)^2} \tag{4.16}$$

$$\Delta g_{\alpha\beta}^{phi} = f_\alpha - f_\beta + \left( \phi_\alpha \frac{\partial f_\alpha}{\partial c_\alpha} + \phi_\beta \frac{\partial f_\beta}{\partial c_\beta} \right) (c_\beta - c_\alpha) \tag{4.17}$$

where, $\mu_{\alpha\beta}$ is the interfacial mobility, $K$ is the kinetic coefficient describing the effect of finite diffusion and redistribution at the interface and $\Delta g_{\alpha\beta}^{phi}$ is the chemical driving force. The evolution equation for $\phi_\beta$ can be easily obtained using the relationship: $\phi_\beta = 1 - \phi_\alpha$. Therefore, it is not explicitly demonstrated here.

In order to model the cellular/dendritic structure, the phase field equation (Eq. 4.15) should be modified properly. Following the simplification suggested in [170], the interfacial energy $\sigma_{\alpha\beta}$ and interface mobility $\mu_{\alpha\beta}$ terms are modified to their anisotropic forms as $\sigma^*_{\alpha\beta}(\vec{n})$ and $\mu^*_{\alpha\beta}(\vec{n})$, where $\vec{n}$ is the interface normal vector described as $\vec{n} = |\nabla\phi_\alpha|/\nabla\phi_\alpha$, in which $\alpha$ represents the solid phase. More explicitly, these two terms are described as follows:

$$\sigma^*_{\alpha\beta}(\vec{n}) = \sigma_{\alpha\beta}(\vec{n}) + \sigma''_{\alpha\beta}(\vec{n}) \tag{4.18}$$

$$\mu^*_{\alpha\beta}(\vec{n}) = \mu_{\alpha\beta}(\vec{n}) + \mu''_{\alpha\beta}(\vec{n}) \tag{4.19}$$

where $\sigma''_{\alpha\beta}(\vec{n})$ and $\mu''_{\alpha\beta}(\vec{n})$ are the second derivatives of $\sigma_{\alpha\beta}(\vec{n})$ and $\mu_{\alpha\beta}(\vec{n})$ with respect to $\vec{n}$. For the solid-liquid interface with 4-fold anisotropy $\sigma_{\alpha\beta}(\vec{n})$ and $\mu_{\alpha\beta}(\vec{n})$ are approximated as:

$$\sigma_{\alpha\beta}(\vec{n}) = \sigma^0_{\alpha\beta}\left(1 - \epsilon\left[3 - 4(n_x^4 + n_y^4)\right]\right) \tag{4.20}$$

$$\mu_{\alpha\beta}(\vec{n}) = \mu^0_{\alpha\beta}\left(1 - \epsilon\left[3 - 4(n_x^4 + n_y^4)\right]\right) \tag{4.21}$$

where $\sigma^0_{\alpha\beta}$, $\mu^0_{\alpha\beta}$ and $\epsilon$ are the interfacial energy coefficient, interface mobility coefficient and anisotropy coefficient, respectively. $n_x$ and $n_y$ represent the x and y components of the norm $\vec{n}$.

To account for the varying temperature during solidification process, the frozen temperature approach is employed. It neglects the latent heat release during solidification and assumes a constant temperature gradient $G$. The temperature field along $y$ axis is calculated as:

$$T(y) = T_0 + G(y - Rt) \tag{4.22}$$

where $T_0$ is the reference temperature, $R$ is the growth rate and $t$ is the time. This approach has been widely adopted in the literature to model directional solidification [165, 182].

### 4.4.3 Computational Procedures

#### 4.4.3.1 Macroscopic Thermal Model

Numerical simulation of the thermal history during LPBF was implemented in Comsol Multiphysics [119]. A fine element with the size of (2 μm) was adopted in and around the melt pool, while relatively coarser elements were utilized at the further locations. The domain size was set to 7 mm × 1.5 mm × 1.5 mm which is sufficiently large enough to negate boundary effects for any combination of power and speed simulated in this work.

Single track laser melting simulations were run at varying laser power (P: 70-255 [W]) and laser speed (*V*: 50-2300 [mm/s]). The values of G and R parameters were extracted from these simulations to use as inputs for the phase field model as illustrated in Fig. 1. Both G and R are calculated on the trailing half of the melt pool which is the portion subject to solidification as the melt pool travels through the substrate at a constant velocity. As suggested in the frozen temperature approach, G is assumed to be constant in the simulation domain of the phase field model and calculated from the partial derivatives of temperature with respect to each Cartesian coordinate with:

$$G = \sqrt{\left(\frac{\partial T}{\partial x}\right)^2 + \left(\frac{\partial T}{\partial y}\right)^2 + \left(\frac{\partial T}{\partial z}\right)^2} \tag{4.23}$$

The growth rate is geometrically derived as the projection of laser velocity V onto the normal vector of the solidification front using the angle (θ) between said vectors [183]:

$$R = V.cos(\theta) \tag{4.24}$$

### 4.4.3.2 Finite Interface Dissipation Phase Field Model

The phase-field and concentration evolution equations, 13,14,15 are numerically solved using the finite difference method (forward in time, centered in space). A dynamic time step is adopted to ensure numerical stability. Neumann boundary conditions are applied to all boundaries. A Fortran code with OpenMP parallelization directives was utilized to reduce the computational time. To investigate the general features of the microstructure, a 2-dimensional simulation domain with the size of 616$\Delta x$ by 4500$\Delta y$ is utilized, where the grid spacing $\Delta x = \Delta y$ =0.008 µm, resulting in a physical size of ~5 µm by 36 µm, while a relatively smaller simulation domain with the size of 800$\Delta x$ by 800$\Delta y$ is adopted to study the effect of process parameters. Initial simulation domain consists of a thin layer of $\gamma$-FCC solid at the bottom and a thick layer of liquid on the top. Initially, random perturbations are applied to the solid-liquid interface to promote cellular/dendritic growth structure. Initial Nb compositions of the solid and liquid are set to $c_s^0 = c_s^{eq}(at\, T = T_0) = 0.022$ and $c_l^0 = c_{alloy} = 0.032$at $(at\, T = 1695\, K)$. The material parameters used in the simulations are listed in Table 4.2. The chemical free energies of each phase are expressed within CALPHAD formalism as described in Eq. 4.12, using the thermodynamic data given in [180]. The frozen temperature approach as described above is used to model the influence of the temperature. Varying values of temperature gradient, G, and growth rate, R, obtained from the thermal model, with the order of magnitudes varying from $10^6$ K/m to $10^8$ K/m, and $10^{-3}$ m/s to 1 m/s, respectively, are fed into the PF model to investigate the morphology, size, and segregation of the simulated microstructures.

**Table 4.2:** The material properties used in the phase field simulations

| Parameters | Values |
|---|---|
| Grid spacing, $\Delta x$ $(\mu m)$ | 0.008 |
| Interface width, $\eta$ $(cm)$ | $1.0x10^{-5}$ |
| Molar volume, $V_m$ $(cm^3/mol)$ | 6.59 |
| Interface energy, $\sigma_{\alpha\beta}^0$ $(J/cm^2\ )$ | $1.0x10^{-5}$ |
| Interface mobility, $\mu_{\alpha\beta}^0$ $(cm^4/Js)$ | 0.99 |
| Diffusivity of solid, $D_S$ $(cm^2/s)$ | $1x10^{-8}$ |
| Diffusivity of liquid, $D_L$ $(cm^2/s)$ | $3x10^{-5}$ |
| Interface permeability, $P$ $(cm^3/Js)$ | 8333 |
| Lattice constant, $a$ $(cm)$ | $3x10^{-8}$ |
| Atomic mobility, $M$ (J/mol) | $1x10^{-10}$ |

| | |
|---|---|
| Anisotropy coefficient, $\epsilon$ | 0.03 |
| Equilibrium freezing range, $\Delta T\ (K)$ | 14 |
| Equilibrium segregation coefficient, $k_e$ | 0.68 |

## 4.5 Results and Discussion

Energy density is often employed as a metric to determine the printability range of LPBF manufactured components. A number of energy density formulations using different process parameters (e.g., laser power, laser speed, hatch spacing, layer thickness, laser beam diameter) have been defined and adopted in the current literature. A thorough discussion on the success and limitation of the energy density formulations as a design parameter can be found elsewhere [184, 185]. Keeping those limitations in mind, in the present work, for simplification, we use the linear energy density (LED) based categorization (e.g. low LED, high LED) while discussing the effect of P and V on the melt pool characteristics (e.g. melt pool size, geometry, temperature gradient, cooling rate) and microstructure (e.g. morphology, size, segregation). LED in this work is calculated by:

$$LED = \frac{P}{v} \tag{4.25}$$

### 4.5.1 Macrostructure Characterization: Experiments

For the experimental validation, three set of process parameters are determined. Figure 4.2 shows optical micrographs of transverse cross-sections of single track laser melts using these three set of process parameters: (a) P: 162 W, V: 957 mm/s, LED (low): 0.169 J/mm (b) P: 96 W, V: 67 mm/s, LED (medium): 1.43 J/mm (c) P: 122 W, V: 50 mm/s, LED (high): 2.44 J/mm. The optical micrographs demonstrate a variation in the melt pool size and geometry depending on the variation in the values of LED. The melt pool widths are measured as 97.79 ± 1.3 μm, 288.29 ± 9.28 μm, and 353.53 ± 10.83 μm, while the melt pool depths are measured as 48.55 ± 1.98 μm, 177.84 ± 6.05 μm, and 321.48 ± 3.64 μm, respectively for low, medium and high LED cases. From left to right in Fig. 4.2, an increase in both melt pool width and depth is revealed due to the increase in the LED.

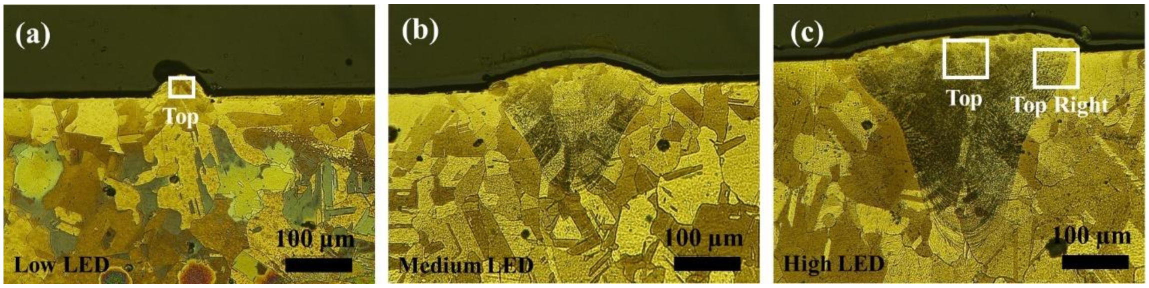

**Figure 4.2:** Optical micrographs demonstrating transverse cross-sections of melt pool obtained under (a) P: 162 W, V: 957 mm/s, LED (low): 0.169 J/mm (b) P:96 W, V: 67 mm/s, LED (medium): 1.43 J/mm (c) P: 122 W, V: 50 mm/s, LED (high): 2.44 J/mm. From left, to right a clear transition from conduction mode to keyhole mode is shown.

Typically, there are three laser heating modes, which influence the melt pool geometry: conduction mode, transition keyhole mode, and keyhole (penetration)mode. Conduction mode heating occurs at low LED and characterized by wide and shallow melt pool shape. Transition keyhole mode is performed at medium LED and results in a melt pool with the aspect ratio (depth/width) of around 1. Keyhole mode heating occurs at high LED and characterized by deep melt pools with a large aspect ratio typically greater than 1.5 [173]. The optical micrographs reveal a clear trend from conduction to transition keyhole mode heating as the LED increases from left to right in Fig. 4.2. Note that, within the range of P: 70-255 [W] and V: 50-2300 [mm/s] used in the present work, conduction mode heating was achieved in the majority of single-track experiments. All the successful prints with P<100 W or V>957 mm/s revealed conduction mode heating, while varying heating modes were achieved depending on the combination of P and V. It is apparent from these results that a variation in process parameters leads to a variation in melt pool characteristics, in turn the solidification microstructure.

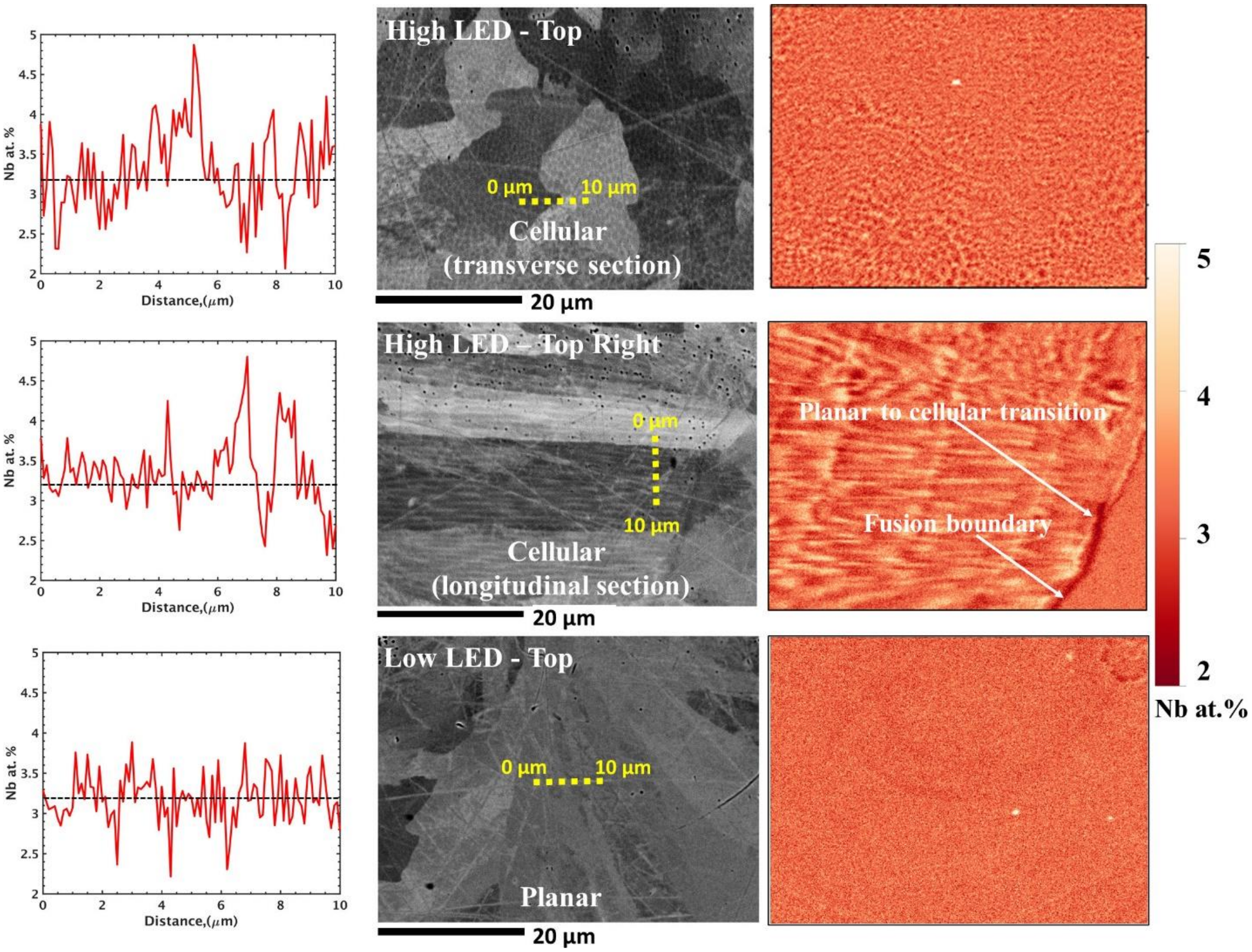

**Figure 4.3:** The microstructure of the selected rectangular regions in Fig. 4.2 are characterized using SEM (middle column), WDS (right column), and WDS line scans (left column). SEM images show cellular and planar morphologies for the corresponding LED conditions in Fig. 4.2.

### 4.5.2 Microstructure Characterization: Experiments

Multiple regions from the melt pools indicated with small rectangles in Fig. 4.2 are selected and characterized using SEM and WDS techniques as shown in Fig. 4.3. SEM micrographs of the selected regions reveal two types of growth structures: cellular and planar. The SEM micrograph corresponding to the top right position under high LED as shown in Fig. 4.3 presents a cellular structure growing normal to the fusion boundary and antiparallel to the heat flux direction. The appearance of columnar cells indicates the directional growth in a positive temperature gradient [186]. Cells are also perceptible in the WDS mappings of the corresponding region due to the composition differences between the cell cores and walls. This variation in the composition is the result of solute rejection by the growing cells. The WDS mapping indicates that cell walls are Nb-rich while cell cores are Ni-rich. Cell growth rates can vary from below the limit of constitutional supercooling to beyond the limit of absolute stability [186]. It is worthwhile to note that the tiny region with Nb depletion in the WDS mapping (right middle in Fig. 4.3 is indicative of the local equilibrium planar structure. The appearance of the planar structure near the fusion boundary can be explained due to the presence of extremely low growth rate. The solidification starts near the fusion boundary once the temperature is below the liquidus temperature (1701 K for the alloy composition of 3.2 (at % Nb) used in the present work [180]). According to the phase diagram [180], the equilibrium composition of the solid phase just below the solidus temperature is around 2.2 (at % Nb), which agrees well with the low Nb composition shown in the planar region at the WDS map. This planar structure quickly transitions to a cellular structure as the temperature decreases below the liquidus temperature and the growth rate exceeds the limit of constitutional supercooling. The constitutional supercooling criteria will further be discussed in the following subsections. Second, according to classical G versus R analysis [187], equiaxed dendrites are formed under low G/R while cells are stable at a higher G/R.

The thermal model simulations in the present work predicted a higher G/R at the top region compared to the top right region indicating the structure at the top region to be cellular. On the other hand, in the low LED case, the SEM micrograph (middle bottom in Fig. 4.3) corresponding to the top region of the melt pool reveals a planar structure with a uniform composition as shown in the corresponding WDS map.

To compare the composition variations in the aforementioned three distinct regions, line scans are extracted from WDS mappings (shown in the left column in Fig. 4.3). The corresponding locations of these line scans are indicated with dashed lines in SEM micrographs. For the cellular structures, the maximum segregation is measured to be Ni-5 at % Nb based on 40 different line scans obtained from the WDS maps of different regions in a melt pool. For the planar structure, although the profile shows a noisy data, the maximum composition is shown to be much lower than the value obtained from the cellular structure. In each figure, the alloy composition of Ni-3.2 at % Nb is shown (dashed line) as a reference. These results indicate that the microstructure vary locally in a single melt pool (e.g. planar vs. cellular in high LED) under constant process parameter as well as from melt pool to melt pool (e.g. planar in low LED vs cellular in high LED) depending on the variation in the applied process parameters.

### 4.5.3 General Features of the Microstructure

Understanding non-planar interfaces (cellular and dendritic) is essential since these growth structures lead to microsegregation and second-phase formation, which affect the mechanical properties and reliability of the solidified material. The characteristic features of a typical non-planar interface (cellular) under AM conditions will be discussed in the following paragraphs.

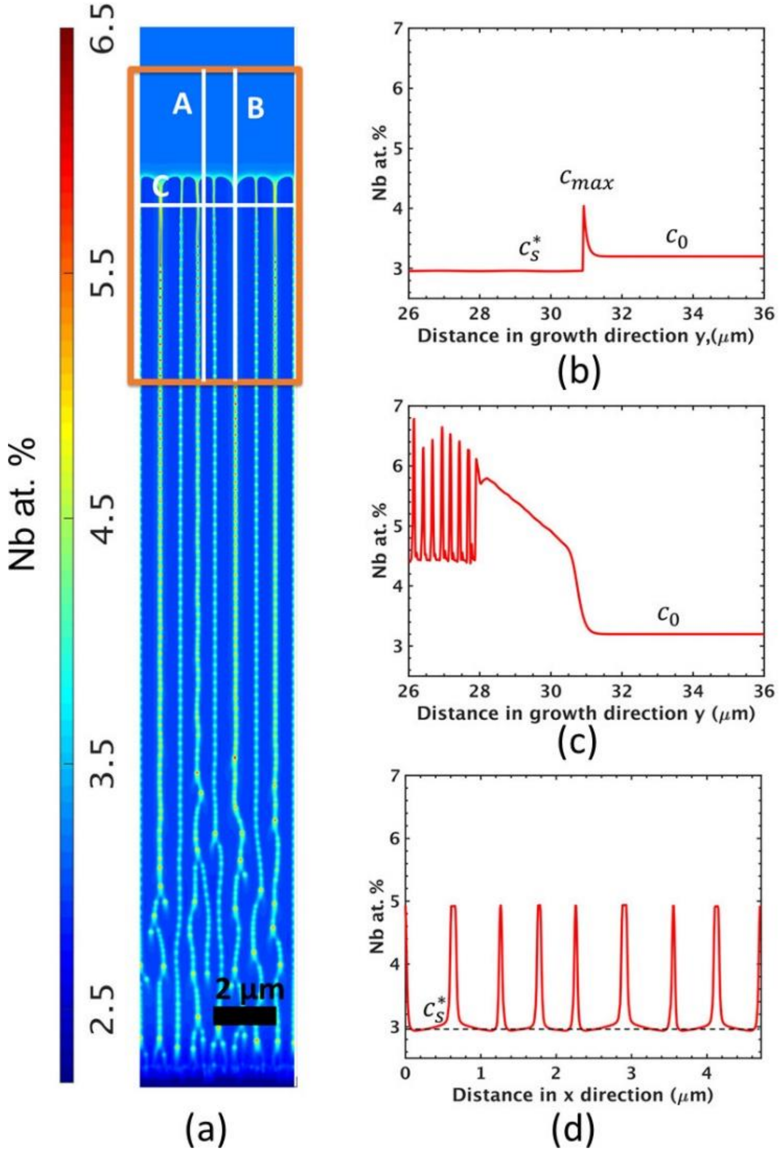

**Figure 4.4:** Typical cellular microstructure forms under LPBF condition. Nb concentration varies along line A (a), B (b), and C (c).

Figure 4.4 (a) represents a typical cellular microstructure predicted in our simulations with the values of G=3×$10^6$ K/m and R=0.03 m/s. Note that, these values of G and R and in turn the simulated microstructure correspond to a particular location in the melt pool. The variation in the morphology and size of the microstructural features under varying G and R across the melt pool will be discussed in the following subsections. The simulation domain was initialized with a thin layer of solid $\gamma$-FCC at the bottom and liquid with the composition of Ni-5 wt.% Nb on top. The initial solid-liquid interface is perturbed randomly to promote the growth of the cellular structure. A number of small cells appears at the fluctuated interface and grow into the liquid in the direction of applied temperature gradient. As solidification advances, competitive growth at the cell fronts occurs and only a few become primary cells. The primary dendrite arm spacing (PDAS) varies at the initial stages and remain constant once the steady state is reached. At this stage, the cell tips advance at a constant velocity and constant temperature as shown in Fig. 4.5. Note that the interface velocity reaches to the applied solidification growth rate R=0.03m/s at steady state.

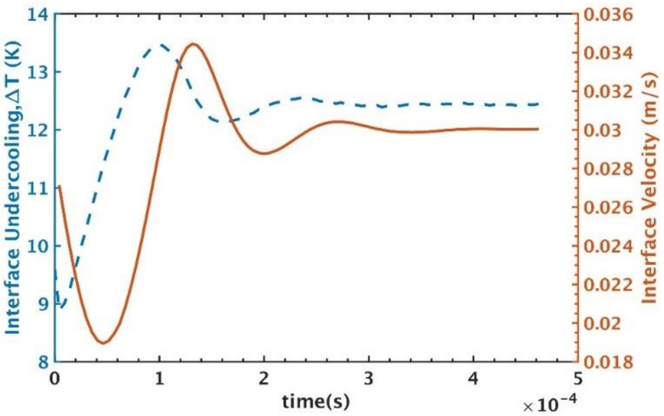

**Figure 4.5:** Phase field evolution of the tip velocity and tip undercooling with time.

The solute microsegregation is a typical phenomenon observed in the solidification process and has significant influence on the mechanical properties of the solidified material. As cells grow, Nb is rejected into the liquid, resulting in Nb enriched intercellular regions as shown in Fig. 4.4 (a). The Nb enriched liquid droplets appearing along the cell grooves as solidification advances are also shown in Fig. 4.4. With time, these Nb enriched droplets may transform to secondary phases such as $Ni_3Nb$. The Scheil simulations~\cite{keller2017application} indicated that for the selected alloy composition (Ni-5 wt.% Nb) implemented in the present work, at least Ni-10 wt.% Nb is needed for such a transformation to occur. However, in the present work, the Nb amount in those droplets have not reached to the sufficient level needed for the precipitation of the secondary phases.

In order to investigate the solute segregation, three lines denoted by A, B, C are selected in Fig. 4.4 (a) and the corresponding Nb concentration profiles along the selected lines are presented in Fig. 4.4 (b) to 4.4 (d). Figure 4.4 (b) demonstrates the Nb concentration variations through the core of the cell into the liquid along the growth direction y (line A in Fig. 4.4 (a)). Left side of this profile denoted by $c_s^*$ corresponds to the concentration in the cell core near the solid-liquid interface (cell tip), while the spike denoted by $c_s^{max}$ represents the concentration at the liquid side of the interface. Beyond this, concentration decreases rapidly and eventually reaches to the far-field liquid composition given by $c_0$.

In Fig. 4.4 (c), the Nb concentration variation is shown along the intercellular region (line B in Fig. 4.4 (a)). Nb concentration gradually decreases in the growth direction y along the intercellular region and reaches the far-field liquid concentration of Ni-3.2 at % Nb beyond the cell tips. The slope of the linearly decaying part, between 28 μm and 30 μm, in Fig. 4.4 (c) is calculated to be 3.33%/ μm. Ignoring the interface curvature effects, the concentration gradient in the above region can be estimated by dc/dx = G/m, where G is the applied temperature gradient,m is the liquidus slope. G and m in this work are 3×10^6K/m and -869 K/%, respectively. Substituting the values in the equation, the solute concentration gradient is found to be 3.45%/ μm, which agrees well with the calculated value.

In Fig. 4.4 (d), the Nb concentration variation is presented perpendicular to the growth direction (line C in Fig. 4.4 (a)). Here, the top and bottom of the U-shaped profile correspond to the Nb concentration in the intercellular regions and the cell cores, respectively. Note that $c_s^*$ in Fig. 4.4 (b) corresponds to the bottom of the U-shaped profile, representing the concentration at the cell core. It is observed that the concentration at the intercellular region is much higher than the concentration inside the cell cores. This happens due to the fact that the solute is rejected from the growing cells into the liquid and since the growth of cells happen rapidly, there is no time for solute to diffuse back and eventually the enrichment of Nb occurs.

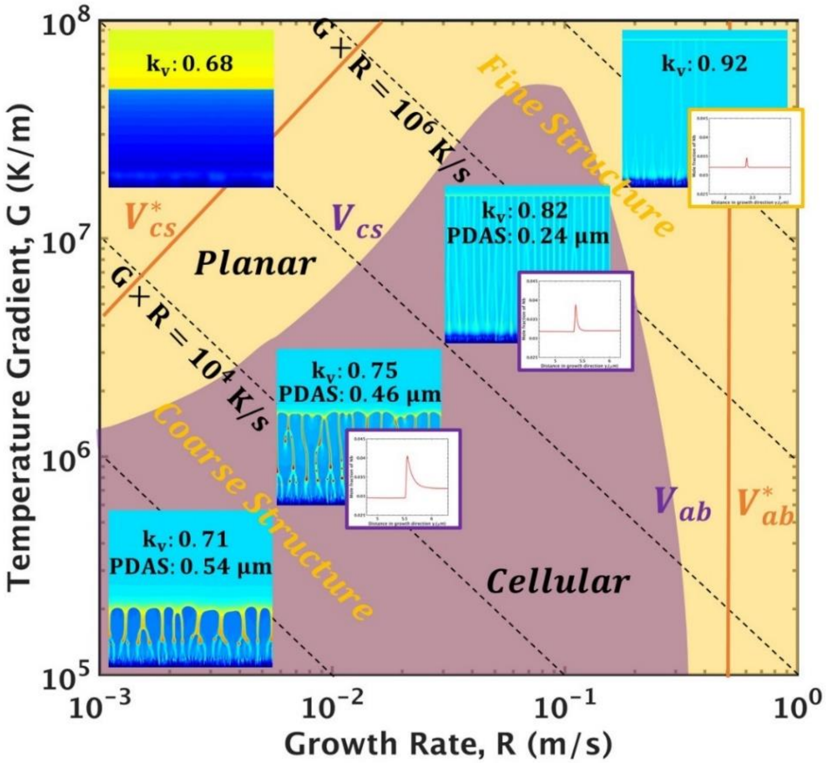

**Figure 4.6:** The variation in morphology, size, and microsegregation as a function of growth rate and temperature gradient is shown.

### 4.5.4 Microstructural Variability as a Function of Thermal Parameters (G, R)

The temperature gradient, G, and the solidification growth rate, R, are the most significant parameters in determining the solidification microstructure. The ratio of these parameters, G/R, determines the morphology of the solidification microstructure (e.g. planar, cellular, columnar dendritic, and equiaxed dendritic), while the product of these parameters G× R, the cooling rate $\dot{T}$, determines the size of the microstructure (the higher the cooling rate the finer the structure is). A solidification morphology selection map for Ni-3.2 at % Nb demonstrating the variation in the morphology and size as a function of G and R is illustrated in Fig. 4.6. For the selected alloy composition and under LPBF process with varying P and V, two types of growth morphologies, planar and cellular, are predicted. As the growth rate increases, a transition from planar to cellular and again to planar morphology is predicted. Typically, the constitutional supercooling criterion [186] and the absolute stability criterion [186] are utilized to roughly estimate these limits of growth rates in between which the cellular morphology is stable, given by $V_{cs}$ < R < $V_{ab}$. Here, the lower limit is determined by the constitutional supercooling criterion, $V_{cs} = \frac{GD_L}{\Delta T}$, while the upper limit is approximated by the absolute stability criterion, $V_{ab}$=$\frac{\Delta T D_L}{k_e \Gamma}$, where $\Delta T$, $k_e$, $\Gamma$ are the equilibrium freezing range, equilibrium segregation coefficient, and Gibbs-Thomson coefficient, respectively. Beyond these limits, a planar structure becomes stable (either for low growth rates (R < $V_{cs}$) or for extremely high growth rates (R > $V_{ab}$)).

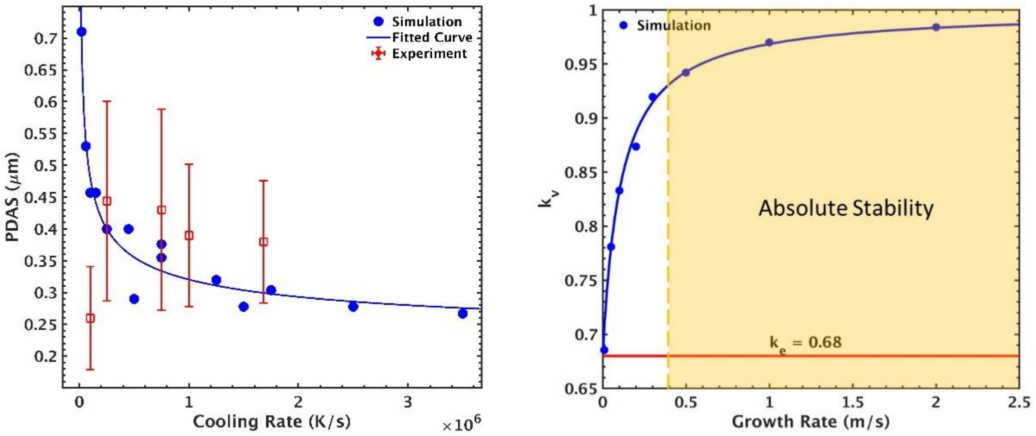

**Figure 4.7:** The calculated primary dendrite arm spacing (PDAS) reduces as the cooling rate increases.As the solidification growth rate $R$ increases the segregation coefficient increases.

In the present work, the aforementioned solidification limits are determined in two ways: the classical theory (linear solid lines) and PF simulations (curvy region). The theoretically determined limits are indicated with $V_{cs}^{*}$ and $V_{ab}^{*}$, while the limits predicted by PF simulations are indicated with $V_{cs}$ and $V_{ab}$ as shown in Fig. 4.6. A triangular region in the middle of map is indicated as cellular in both cases. A less than an order of magnitude difference is shown between the lower and upper limits predicted from model and theory especially for high G conditions, while a much better agreement is achieved as G decreases. Note that the theory gives a rough estimate and have some limitations. For example, the constitutional supercooling criterion ignores the effect of surface tension, which is considered in our PF simulations. Also, the absolute stability criterion has other limitations. For instance, it accounts only for the species diffusion in the liquid and thus neglects solid diffusion, which is taken into account in PF predictions. Therefore, we believe that the theoretical predictions are less accurate, especially under rapid solidification conditions.

In addition to the type of growth structures (planar and cellular), the presented solidification map in Fig. 4.6 can be utilized to gain information on the variation in size and microsegregation as a function of G and R. As the cooling rate increases (from the bottom left corner to the top right corner), PDAS reduces (within $V_{cs}$<R<$V_{ab}$) and finally the interface restabilizes and a segregation-free planar structure is achieved (beyond R>$V_{ab}$). We would like to recall that in the majority of current literature, a cellular/dendritic structure with nonuniform properties is predicted/observed as the typical growth structure under AM. In the present work, we emphasis the possibility of a planar structure with uniform properties for the high cooling rates (~$10^7$ -$10^8$ K/s).

On the other hand, increasing the cooling rate/growth rate results in a decrease in the calculated $k_v$. The $k_v$ in equilibrium condition for the selected alloy is calculated as $k_e$=0.68. Our simulations demonstrated that $k_v$=$k_e$ with $c_s^0$=$c_s^{eq}$ is achieved only for the low growth rates, observed near the fusion boundary, and resulted in a planar growth structure as demonstrated in top left image in Fig. 4.6. This finding agrees well with the Nb depleted region near the fusion boundary as presented in Fig. 4.3. Beyond the fusion boundary and through the center line of the track, the growth rate is much higher and the resultant segregation coefficient given by $k_v$ diverges from the equilibrium value and eventually reaches to $k_v$~=1, indicating the full solute trapping condition, which takes place during rapid solidification beyond the velocity limit of absolute stability (R>>$V_{ab}$) as represented with the top right image in Fig. 4.6. The inset images in Fig. 4.6 illustrates the variation in the concentration profile (in mole fraction Nb) and the calculated $k_v$ for the representative microstructure predictions. It is shown that as cooling rate/growth rate increases, the peak of the profile reduces while the concentration at the left and right side of the profile approach and become equal with the value of $c_0$ and $k_v$~=1, indicating the solute trapping. It should be noted that the finite interface dissipation phase field model utilized in the present work is well suited to study the rapid solidification phenomenon such as solute trapping. By adjusting the permeability parameter $\mathrm{P}^{\mathrm{intf}}$ (Eq.~\ref{eq:permeability}), we can quantify the solute trapping behavior, as well as the non-equilibrium segregation coefficient.

The variation in PDAS and $k_v$ as a function of G and R are further analyzed in Fig. 4.7. As discussed in the above paragraphs, during rapid solidification the system deviates from the local equilibrium. To quantify this deviation, the velocity-dependent partition coefficient kv, given by: $k_v(R)$ =$c_s^*/c_s^{max}$ [188] is plotted against the growth rate as shown in Fig. 4.7 (b). The horizontal line in Fig. 4.7 (b) represents the equilibrium segregation coefficient of the NiNb alloy. As the solidification growth rate R increases, the calculated segregation coefficient deviates from this value and approaches to 1 beyond the velocity limit of absolute stability indicated with a vertical dashed line in Fig. 4.7 (b). Above this limit, the solid-liquid interface restabilizes to a planar interface.

Fig. 4.7 (a) presents the variation in predicted PDAS with respect to the cooling rate (G×R) along with a fitted line. It is evident that as the cooling rate increases, the PDAS decreases. The typical cooling rate under AM ranges from $10^5$ K/s to $10^8$ K/s depending on the process parameters and the location in the melt pool. The predicted PDAS varies from 0.58 µm to 0.2 µm, as the cooling rate increases from $10^5$ K/s to 3.5×$10^6$ K/s. Above this, a transition from cellular to planar interface is observed. Note that, although both increasing G and R leads to an increase in the cooling rate (G × R), hence smaller PDAS, their effects might be different. For example, at G=5×$10^5$ K/m and R=3×$10^{-1}$ m/s fine cellular structure is observed with the PDAS of 0.3 µm while a planar structure for R < $V_{cs}$ is observed at G=1.5×$10^7$ K/m and R=1×$10^{-2}$ m/s. Although in both cases the cooling rate is calculated as G × R=1.5×$10^5$ K/s, two different growth structure is observed. In another example with the condition of G=5×$10^5$ K/m and R=1×$10^{-1}$ m/s results in a PDAS of 0.4 µm, whereas G=5×$10^6$ K/m and R=1×$10^{-2}$ m/s leads to a PDAS of 1 µm.

Therefore, one should be careful on using the PDAS vs. cooling rate information when there is a few orders of magnitude variation in G. On the other hand, by keeping the G constant and varying R, a consistent correlation between PDAS and cooling rate can be obtained. Note that, Fig. 4.7 (a) is created by varying G within the range of $10^6$-$10^7$ K/m and R from R=$10^{-2}$ m/s to R=$10^{-1}$ m/s. Therefore, the information provided in this plot will be valid only for the given ranges of G and R.

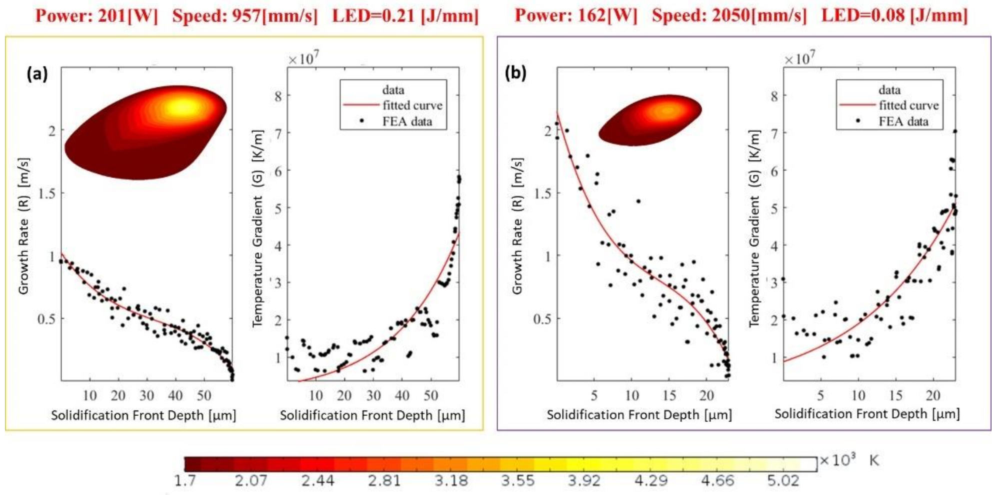

**Figure 4.8:** The predicted temperature gradient, G and growth rate, R are shown for varying solidification front depths for two set of process parameters

### 4.5.5 Microstructural Variability as a Function of Process Parameters

Microstructural features vary spatially within a single melt pool as well as from melt pool to melt pool depending on the process parameters applied. It is therefore essential to understand and control these variabilities by tailoring the process parameters so that a final product with desired properties can be achieved. In this subsection, the influence of process parameters on the thermal parameters (G, R) will be discussed first, followed by a description of the microstructural features as a function of these estimated thermal parameters.

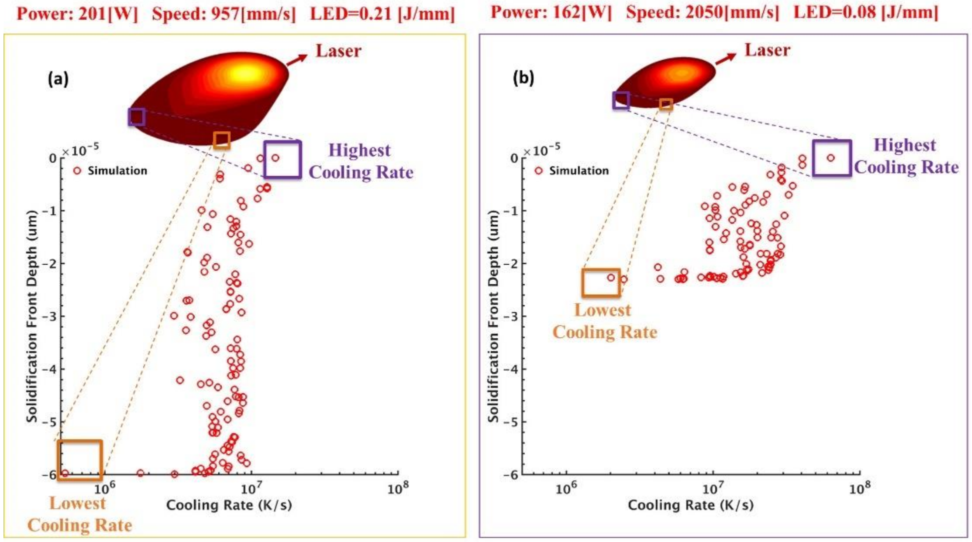

**Figure 4.9:** The predicted cooling rates at varying solidification front depths are shown for two set of process parameters

### 4.5.5.1 Effects of Temperature Gradient, Growth Rate, and Cooling Rate

Single track laser melting simulations were run at varying laser power (P: 70-255 [W]) and laser speed (V: 50-2300 [mm/s]). To investigate spatial variations in the microstructural features, the output G and R were predicted both along the longitudinal section and transverse section of the resultant melt pool. Fig. 4.8 represents an example of output G and R for two sets of P and V along the longitudinal section of the melt pool boundary, corresponding to high and low LED cases. Depending on the location of the melt pool, the calculated G and R varied within the range of [$3\times10^6$ K/m - $5\times10^7$ K/m] and [$3\times10^{-5}$ m/s - 1 m/s], respectively. The maximum R is calculated near the top of the melt pool (with a low solidification front depth) while the minimum is found near the bottom of the melt pool (with a high solidification front depth). In contrast, the maximum G is calculated at the bottom of the melt pool as the minimum G is observed at the top.

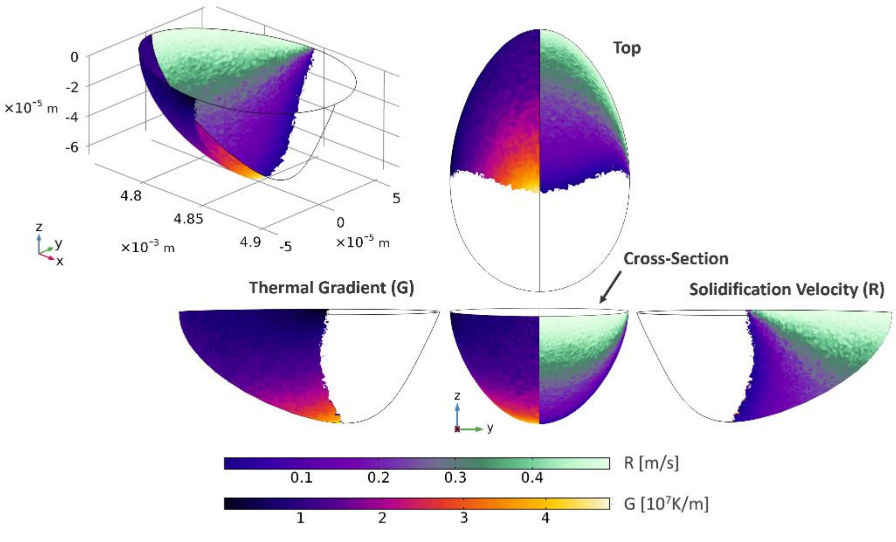

**Figure 4.10:** Variation in G and R are shown across the melt pool.

Since with the increase in the solidification front depth, G increases and R decreases, it is not clear from Fig. 4.8 how the resultant cooling rate $\dot{T} = GR$ will vary as a function of the depth. In figure 4.9, the variation of $\dot{T}$ along the melt pool boundary with increasing depth is explicitly shown for the same process parameters as in Fig. 4.8. On the left, an example of high LED case is shown, while on the right a low LED case is presented. In both cases, we observe that, on average, the cooling rate increases as we move from the bottom to the top along the melt pool boundary. On the other hand, the predicted cooling rate at different LED cases show differences; the lower the LED, the higher the cooling rate, on average. While the maximum predicted cooling rate in the high LED case is around $\dot{T}=1.5\times10^7$ K/s, in the low LED case, the maximum $\dot{T}=7\times10^7$ K/s. Variations in the cooling rate affect the solidification microstructure, which will be discussed in the following sections.

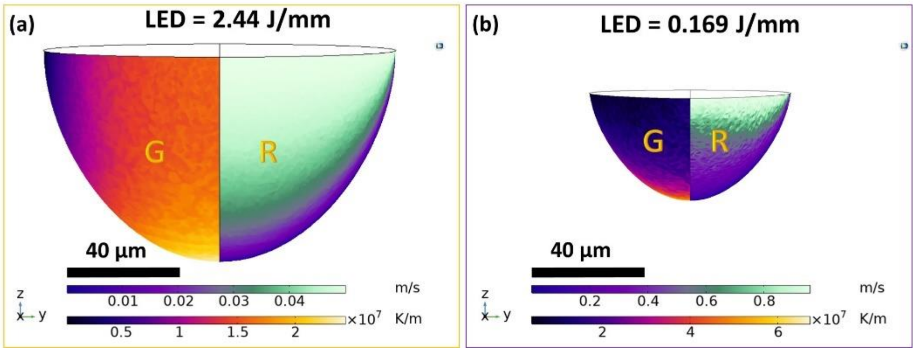

**Figure 4.11:** The calculated G and R along the transverse section of the melt pool boundary are shown for two set of process parameters with different linear energy densities (LED).

The variation in G and R along the longitudinal section of the melt pool boundary is already discussed in the above paragraphs. Fig. 4.10 presents a top, side (longitudinal), cross-section (transverse), and oblique views of the three-dimensional melt pool at P:162 [W] and V: 500 [mm/s], demonstrating the local variation in the G and R throughout the melt pool boundary. The same trend for the G and R as presented in Fig. 4.8 is shown along the melt pool boundary in the longitudinal view (as the depth increases along the melt pool boundary, G increases while R decreases). In addition, the local variation in G and R across the melt pool can be seen in Fig. 4.10. The left half of the cross-sectional view in Fig. 4.10 demonstrates the temperature gradient G, while the right half represents the solidification growth rate R. G increases from top ($1.5\times10^6$ K/m) to bottom ($4.8\times10^7$ K/m) across the melt pool with the minimum and the maximum being at the top (left) edge and the bottom of the melt pool, respectively. In contrast, R reduces from the top to the bottom as well as from the interior of the melt pool to the edge of the melt pool.

In the present work, the experimental analysis of the microstructure is performed at the transverse cross-sections of the melt pool. Therefore, the G and R data across the transverse cross-section will be utilized for the validation purpose. To predict the spatial variation in the microstructural features across the transverse section, the G and R data at corresponding locations are extracted from the associated melt pools (Fig. 4.11). For the experimental validation, we will be using three different cases: low, medium and high LED. Here, we show the variation in G and R for the low and high LED cases as an example. The G and R data needed for the medium LED case is also extracted from the associated melt pool, but not explicitly shown here. The high LED case results in a larger melt pool size with a lower G and R values, when compared to the low LED case as expected. This can be due to the fact that as the laser speed Vincreases, the heat accumulated in the laser interaction zone decreases, leading to formation of smaller melt pools. In both the cases, G increases from the top to the bottom. While a high degree of variation in G from the top-edge to the top-interior location in the melt pool is observed in the high LED condition, it is almost constant in the low LED condition. In contrast to G, R decreases from the top to the bottom and from interior to edge in both cases. Since

R is a function of V, it is reasonable to observe higher cooling rate for higher V. This is the case with the low LED condition.

#### 4.5.5.2 Morphology and Size

We have discussed the general features of the solidification microstructures in the above paragraphs. As mentioned previously, the growth structure and size vary locally within a melt pool as well as from melt pool to melt pool under different processing conditions. To investigate the variation in the microstructure along the longitudinal section of melt pools under different AM conditions, the calculated cooling rates along the melt pool boundaries, as shown in Fig. 4.8, are utilized.

Fig. 4.12 demonstrates the variation in the solidification microstructure at different locations of the melt pool boundary under high LED condition. It is observed that the resultant cooling rates in this case lead to the formation of cellular structure with varying size of the cells (PDAS) along the melt pool boundary. As the cooling rate increases from the bottom to the top of the melt pool, the cells become finer. Here, the predicted cooling rate varied from $2\times10^4$ K/s to $3.5\times10^6$ K/s as we go from the bottom to the top of the melt pool, and the PDAS ranged from 0.7 μm to 0.3 μm, respectively. It is worthwhile to note that Ghosh et al. [36] predicted the cooling rate varying from $5\times10^4$ K/s to $3\times10^6$ K/s, and corresponding PDAS to be within the range of 1.6 μm-0.14 μm under similar laser processing parameters (P=195W and V=800mm/s), using the conventional PF model with local equilibrium assumption. It is clear that in the work by Ghosh et al., a larger range of PDAS were predicted. This difference could be due to many sources. First of all, although both studies use the binary Ni-5 wt. % Nb as the modeling material, the aforementioned work aimed to approximate the microstructure of Inconel 718, hence adopted the thermodynamic data from a quasi-binary phase diagram of Inconel 718. Based on the utilized phase diagram, the freezing range and equilibrium segregation coefficient were reported as 57 K [159], 0.48 [159], respectively in the aforementioned study, whereas these properties in the present work are given as 14 K and 0.68, respectively. It is inevitable that these variations in the material properties will also influence the microstructure predictions. The other source of this difference could be due to the differences in the employed PF models (local equilibrium model vs non-equilibrium model).

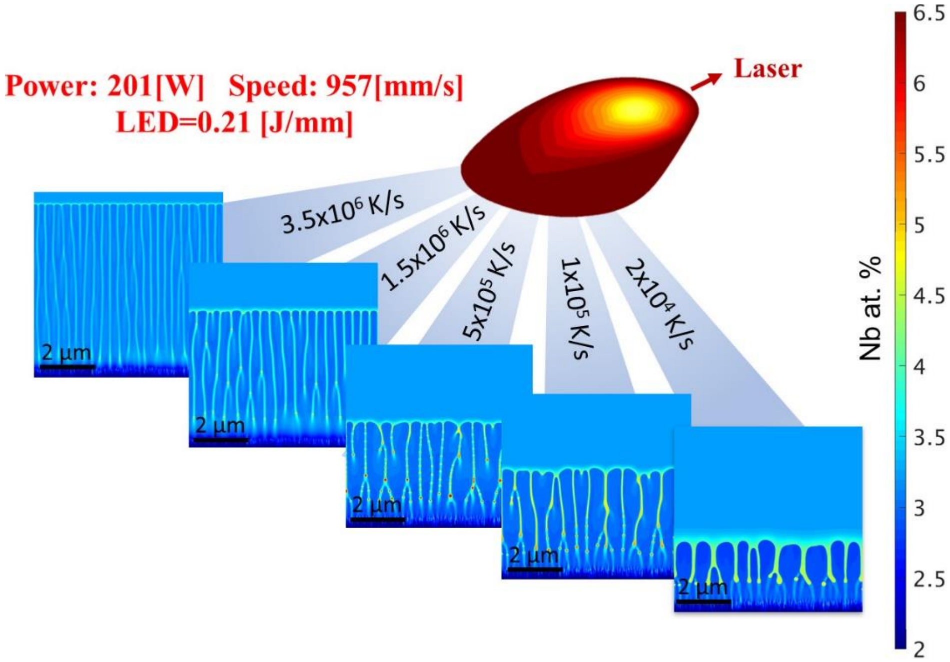

**Figure 4.12:** Variation in the cellular structure and size at varying cooling rates along the melt pool boundary is shown for high LED condition.

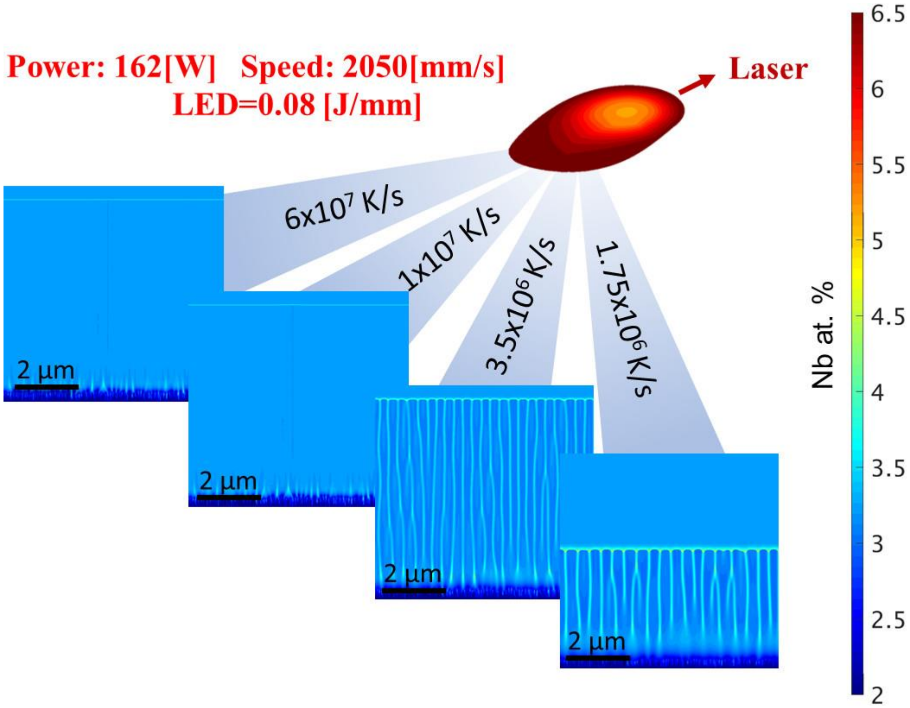

**Figure 4.13:** Variation in the solidification structure and size at varying cooling rates along the melt pool boundary is shown for low LED condition. A transition from cell to plane structure is observed at high cooling rates.

Fig. 4.13 demonstrates the variation in the solidification microstructure at different locations of the melt pool boundary under low LED condition. Here, the predicted cooling rate varied from $1.75\times10^6$ K/s to $6\times10^7$ K/s from bottom to top of the melt pool. Near the bottom of the melt pool, a cellular structure is predicted, while a planar structure is observed near the top of the melt pool due to extremely high cooling rates. Note that the transition from cellular to planar structure at high solidification growth rate (hence the cooling rate) is already reported in the literature. One can refer to the solidification map in Fig. 4.6 to gain an understanding of the effect of G and R on such a transition in the growth morphology.

Next, the predicted growth morphology and size throughout the transverse section of melt pool are demonstrated along with the experimental measurements for three set of process parameters as high LED (P: 122 W, V: 50 mm/s, LED: 2.44 J/mm), medium LED (P: 96 W, V: 67 mm/s, LED: 1.43 J/mm), and low LED (P: 162 W, V: 957 mm/s, LED:

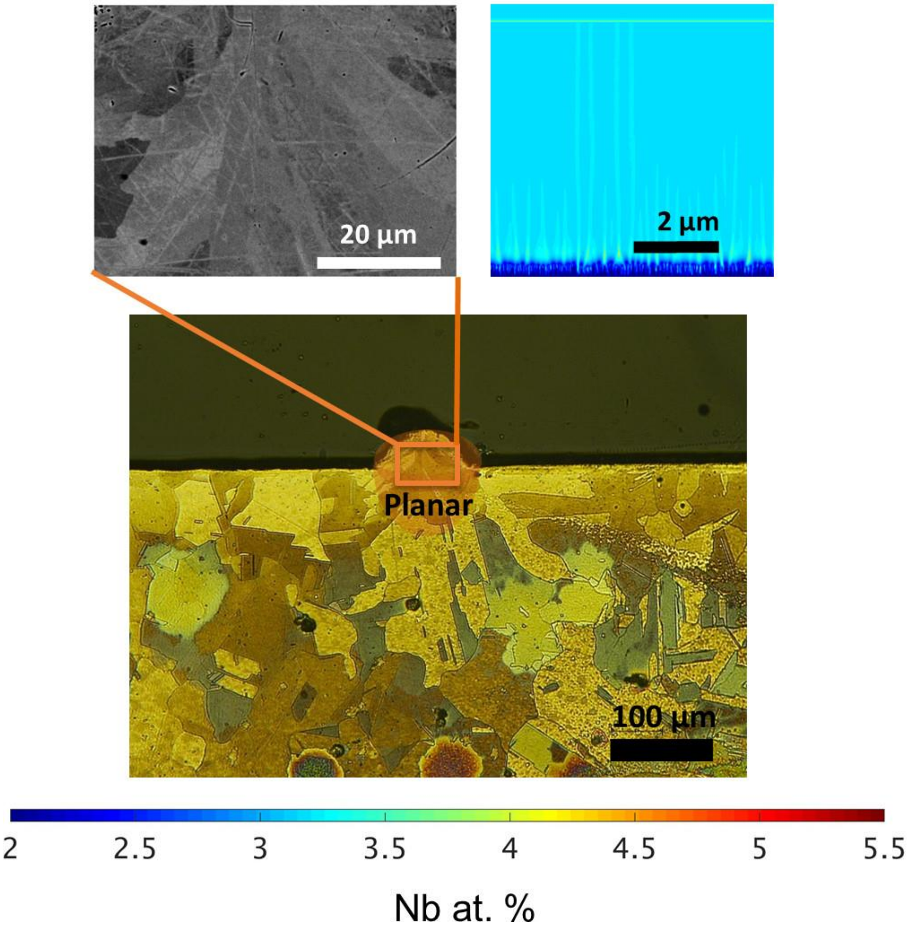

**Figure 4.14:** The predicted growth morphology and size throughout the melt pool are demonstrated along with the experimental measurements. Planar structure is observed throughout the melt pool. (P: 162 W, V: 957 mm/s, LED: 0.169 J/mm)

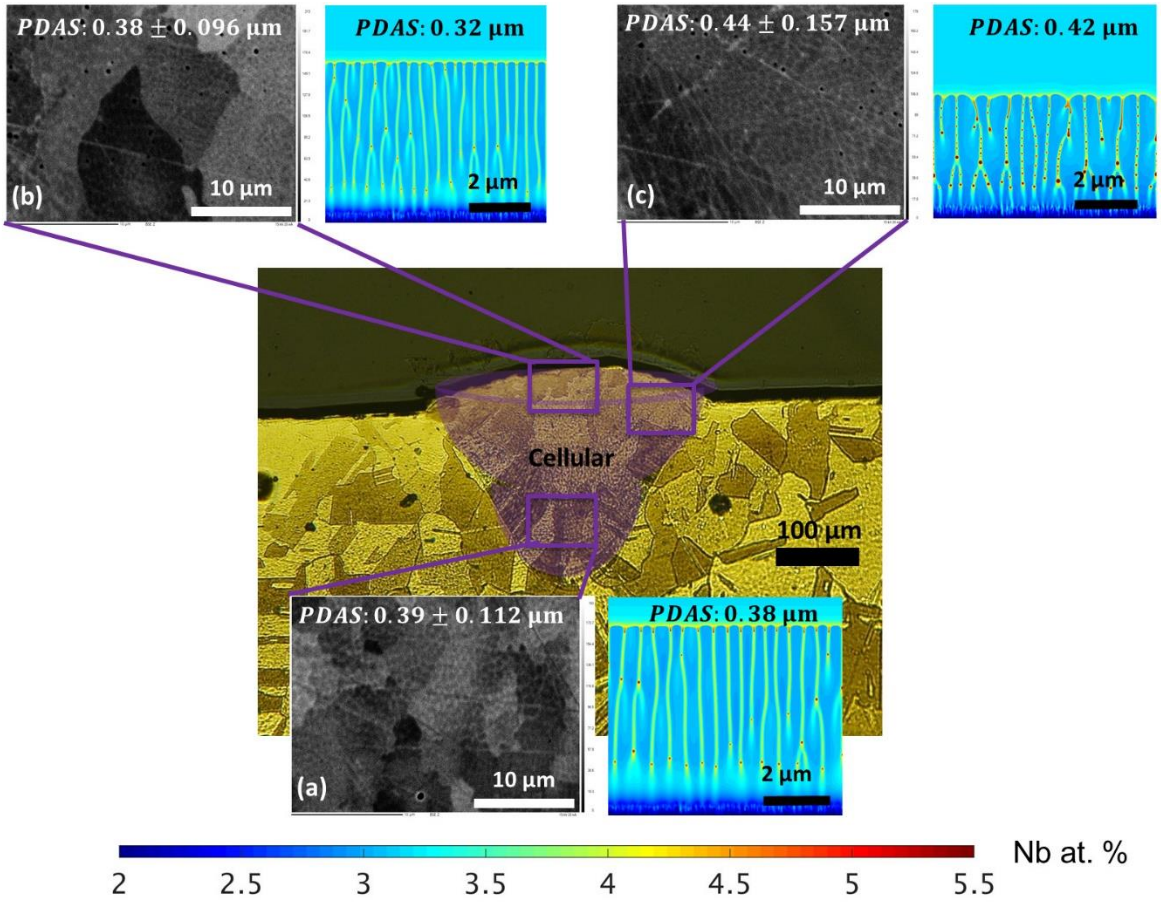

**Figure 4.15:** The predicted growth morphology and size throughout the melt pool are demonstrated along with the experimental measurements. Cellular structure is observed throughout the melt pool. (P: 96 W, V: 67 mm/s, LED: 1.43 J/mm)

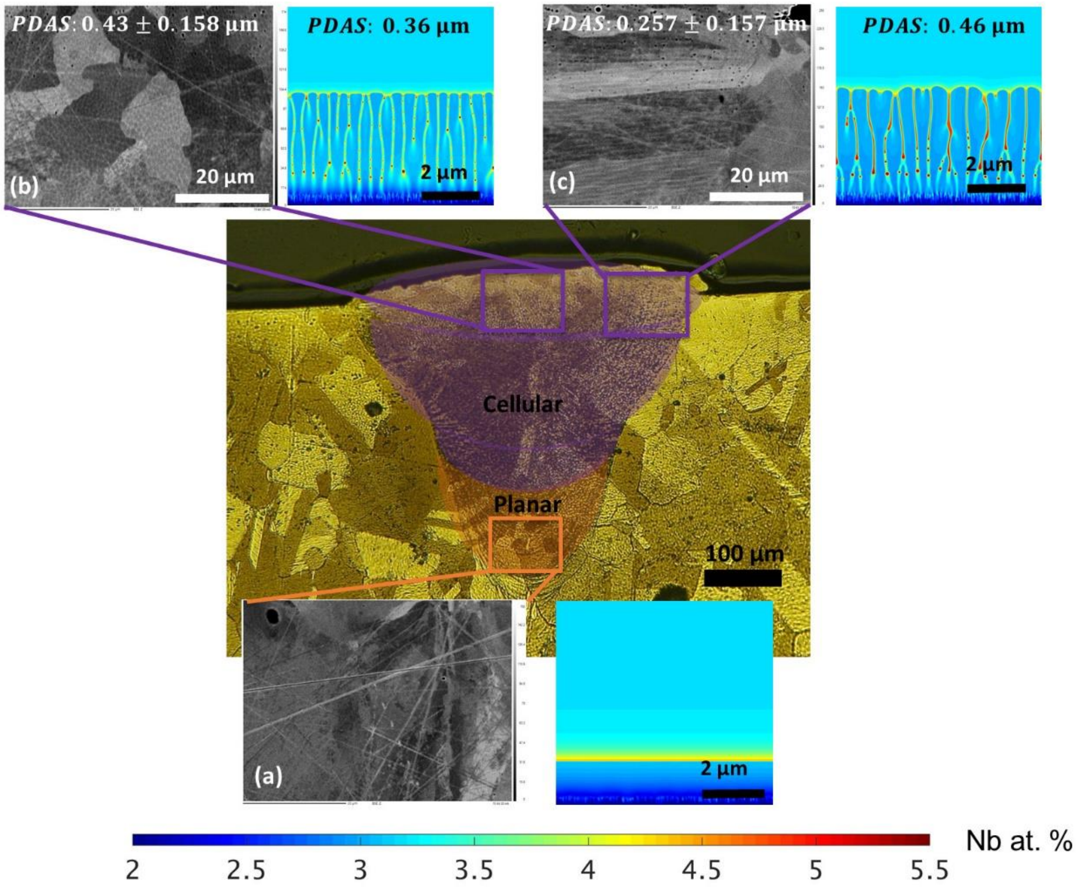

**Figure 4.16:** The predicted growth morphology and size throughout the melt pool are demonstrated along with the experimental measurements at the corresponding locations. A transition from a planar to a cellular structure from the bottom to the top of the melt pool is observed. (P: 122 W, V: 50 mm/s, LED: 2.44 J/mm)

0.169 J/mm). Fig. 4.14 demonstrates the predicted and measured microstructure at varying locations along the transverse section of the melt pool for P: 162 W, V: 957 mm/s. The calculated LED is 0.169 J/mm at this condition, which we call as the low LED case. A conduction mode melt pool with the low depth-to-width aspect ratio is shown in the optical micrography image. The SEM micrographs in Fig. 4.14 present a planar structure. From the thermal model, a very low R with R < $V_{cs}$ is predicted near the edge of the melt pool, hence a planar structure is expected to form. in the low LED case, the values of R vary within the range of 0.2-0.9 m/s (Fig. 4.11), which falls into the region of R > $V_{ab}$. Note that, in experiments solidification always begins with a planar structure at the melt pool boundary (R < $V_{cs}$), which is followed by a transition to cellular ($V_{cs}$ < R < $V_{ab}$) or planar structure (R > $V_{ab}$), depending on the laser processing conditions.

Fig. 4.15 demonstrates the predicted and measured microstructure at varying locations along the transverse section of the melt pool for P: 96 W, V: 67 mm/s. The calculated LED is 1.43 J/mm at this condition, which we call as the medium LED case. A conduction to keyhole transition mode melt pool with the medium depth-to-width aspect ratio is shown in the optical micrography image. The SEM micrographs in Fig. 4.15 present the microstructure and size at three different locations: bottom (a), top-middle (b), and top-edge (c). All locations show cellular structure with measured PDAS of 0.39 ± 0.112 μm, 0.38 ± 0.096 μm, and 0.44 ± 0.157 μm, and the PF-predicted PDAS of 0.38 μm, 0.32 μm, and 0.42 μm, respectively, indicating a very good agreement between the simulation and experimental measurement. The predicted morphologies and PDAS at varying locations, from top to bottom and from top-middle to top-edge, are also presented in Fig. 4.15. The results show that the PDAS decreases from the top to the bottom of the melt pool with the maximum and the minimum being 0.46 μm and 0.38 μm, respectively. In contrast, the PDAS increases from the top-middle to the top-edge region with minimum and maximum being 0.32 μm and 0.42 μm, respectively. The predictions show that the cooling rate decreases from top-middle to top-edge explaining the increase in PDAS.

Fig. 4.16 demonstrates the predicted and measured microstructure at varying locations along the transverse section of the melt pool for P: 122 W, V: 50 mm/s. The calculated LED is 2.44 J/mm at this condition, which we call as the high LED case. A keyhole mode melt pool with the high depth-to-width aspect ratio is shown in the optical micrography image. The bottom region is exposed to a high G and low R < $V_{cs}$, hence corresponds to the planar region as shown in Fig. 4.6. On the other hand, the top region shows a relatively lower G and R (between $V_{cs}$ and $V_{ab}$). Therefore, a cellular structure is stable at this region, as depicted in Fig. 4.6. The SEM micrographs in Fig. 4.16 present the microstructure and size at three different locations: the bottom (a), top-middle (b), and top-edge (c). The bottom (a) location shows a planar structure. Similarly, a planar structure is predicted by the PF simulations at the corresponding location. The top-middle location (b) shows a cellular structure with the measured PDAS of 0.43 ± 0.158 μm. The PF-predicted PDAS at this location is 0.36 μm. The top-edge (c) shows a long cellular structure which grow from the melt pool boundary to the interior melt pool. The measured PDAS at this location is 0.4257 ± 0.157 μm while the PF-predicted PDAS is 0.46 μm. While the PF-predicted PDAS increases from the top-middle to the top-edge region, the experimentally measured PDAS decreases. The simulations and experiments do not agree in this scenario. We wish to note that, PDAS at the top-edge location is measured to be greater than that of at the top-middle region for almost half of the total number of melt pool measurements corresponding to multiple sets of process parameters. Therefore, it is difficult to make a conclusion on how the PDAS should vary from the top-middle to the top-edge location. For example, in Fig. 4.15, PDAS increases with the increasing distance from the top-middle to the top-edge region. On the other hand, the model consistently shows that the predicted PDAS increases as we move from top-middle to top-edge. Another source of this discrepancy could be due to the fact that the convection in the melt pool is not taken into account in the thermal model, hence the FE model is not accurate for predicting the keyhole mode melt pool shape, as seen in the high LED case.

In the previous paragraphs, we explained the variation in the morphology and size of the microstructural features across the solidified melt pool for different processing conditions. Nb microsegregation is another important phenomenon to discuss. The overall results indicate that as the cooling rate increases, the concentration of Nb in the intercellular region decreases. For example, a reduction in the cooling rate from $7.5\times10^5$K/s to $1.5\times10^5$K/s leads to an increase in the amount of Nb in the intercellular region from 4 to 5 (in at % Nb). Also, once the growth rate reaches beyond the absolute stability limit, a segregation-free planar structure is formed. Since the growth rate is a strong function of the laser speed, it is assumed to have this type of segregation free structure to be formed under sufficiently high laser speed conditions.

### 4.6 Summary and Conclusion

In the present work, we developed a computational modeling framework by coupling a FE-based thermal model to a non-equilibrium PF model to investigate the rapid solidification microstructure that forms during the single track melting of Ni-3.2 at.% Nb.

In contrast with the most existing work in the literature in which a PF model with the assumption of local equilibrium at the solid-liquid interface is adopted, the developed framework employs the finite interface dissipation PF model, which can successfully describe the out-of-equilibrium systems, hence is well suited to predict the rapid solidification microstructure during the LPBF process.

The present study provides a consistent framework by adopting a binary Ni-3.2 at.% Nb alloy in both phase field model and validation experiments. Note that the finite interface dissipation PF model adopted in the present work is well suited for describing multi-phase multi-component alloy systems. The main goal of the present work is to elucidate the influence of the process parameters on the variabilities in solidification microstructure under single-track laser melting conditions. Once the microstructure variabilities in a simple binary alloy during single-track experiments is well understood, the next step would be employing the present framework to investigate more complex alloy systems (e.g. Inconel 718) under multi-track laser melting conditions.

The major findings of the present work can be summarized as follows:

1. The single-track laser melting simulations were run at varying laser power (P: 70-255 [W]) and laser speed (V: 50-2300 [mm/s]) and a planar to cellular transition was predicted as we go from the melt pool boundary to the interior of majority of the keyhole mode melt pools. A planar interface beyond the limit of absolute stability was predominant in the conduction mode melt pools with high growth rates.

2. A solidification map of Ni-Nb alloy under L-PBF conditions (Fig. 4.6), describing the variation in the morpholgy and size as a function of temperature gradient

G and growth rate R was presented. The minimum G and R conditions, leading to a segregation-free planar structure (beyond the absolute stability) was demonstrated.

3. The typical cooling rate during LPBF ranged from ~$10^5$ K/s to ~$10^8$ K/s depending on the process parameters and the location in the melt pool. Above 3.5×106 K/s, a transition from cellular to planar interface was predicted with growth rates beyond $V_{ab}$.

4. The predicted morphology and size during the single-track melt pool solidification under varying process conditions were compared against the experimental measurements, and a very good agreement was achieved regarding the cell spacing (ranging between ~0.2 and ~0.5 μm) and the amount of Nb in the intercellular region (from 4-5 at. %Nb).

# 5. SUMMARY AND FUTURE WORK

In this Chapter, we summarize each part of this dissertation, emphasize the key contributions and address the future directions.

In Chapter 2, a three-dimensional FE model was developed for studying the thermal history during laser powder bed fusion (LPBF) of Ti-6Al-4V alloy. In contrast to most existing works in the literature, the developed model considers material evaporation, which was achieved by employing a new physics-based approach. The validation experiments including state-of-the-art in-situ thermal measurements were also conducted to measure the size of the HAZ as well as to monitor the thermal history on the surface, which were then compared to the calculated values to validate the model. To our knowledge, this is the first study demonstrating a comparison of multi-track thermal history with in-situ experimental measurements using dual-wavelength pyrometry, in addition to concurrently presenting two FE model validation techniques (physical experimentation observations with SEM and pyrometer).

In Chapter 3, a V&V study for thermal modeling of LPBF processes was presented. Although the focus was on the code-to-code Verification assessments, which went unheeded in the existent literature, experimental validation was also conducted for completeness. Two different finite element-based thermal models were developed and implemented in two different platforms (Comsol Multiphysics® and Sierra Mechanics). The same process parameters, material properties and physics were used in both models, while the numerical implementation and the modeling parameters such as mesh size, mesh type or error tolerances used in the models were set differently. Overall, a very good agreement in the results was achieved. In this chapter, we emphasized the value of V&V in building credibility in thermal modeling of AM processes and provided a methodology for code-to-code Verification assessments.

In Chapter 4, a computational modeling framework coupling a FE-based thermal model to a non-equilibrium PF model was presented to investigate the rapid solidification microstructure that forms during the single-track melting of Ni-3.2 at % Nb. In contrast with the most existing work in the literature in which a PF model with the assumption of local equilibrium at the solid-liquid interface is adopted, the developed framework employs the finite interface dissipation PF model, which can successfully describe the out-of-equilibrium systems, hence is well suited to predict the rapid solidification microstructure during the LPBF process. The present study provides a consistent framework by adopting a binary Ni-3.2 at. % Nb alloy in both phase field model and validation experiments. Note that the finite interface dissipation PF model adopted in the present work is well suited for describing multi-phase and multi-component alloy systems. To our knowledge, this is the first study investigating the spatial variations in the rapid solidification microstructure under varying additive manufacturing conditions utilizing the non-equilibrium PF model and validation experiments of the same material.

The main goal of this dissertation was to provide a consistent computational modeling framework to predict the variabilities in solidification microstructure as a function of process parameters of LPBF process. The developed framework was utilized to investigate the single-track laser melting of binary Ni-Nb alloy. The future research includes employing the present framework to investigate more complex alloy systems (e.g. Inconel 718) under multi-track laser melting conditions.

The developed modeling framework does not consider the influence of fluid flow in the solidification microstructure. It is expected that due to the high temperature gradients in the melt pool, the convection has a significant impact on the melt pool shape and the microstructure pattern. Therefore, the future work includes the incorporation of Lattice Boltzmann method to the developed modeling framework in order to investigate the influence of fluid flow on rapid solidification microstructure.

# REFERENCES

1. Wohlers, T., *Wohlers report.* Wohlers Associates Inc, 2014.

2. Schoinochoritis, B., D. Chantzis, and K. Salonitis, *Simulation of metallic powder bed additive manufacturing processes with the finite element method: a critical review.* Proceedings of the Institution of Mechanical Engineers, Part B: Journal of Engineering Manufacture, 2015: p. 0954405414567522.

3. Tolosa, I., et al., *Study of mechanical properties of AISI 316 stainless steel processed by "selective laser melting", following different manufacturing strategies.* International Journal of Advanced Manufacturing Technology, 2010. **51**(5-8): p. 639-647.

4. Garibaldi, M., et al., *Metallurgy of high-silicon steel parts produced using Selective Laser Melting.* Acta Materialia, 2016. **110**: p. 207-216.

5. Niendorf, T. and F. Brenne, *Steel showing twinning-induced plasticity processed by selective laser melting - An additively manufactured high performance material.* Materials Characterization, 2013. **85**: p. 57-63.

6. Murr, L.E., et al., *Microstructure and mechanical behavior of Ti-6Al-4V produced by rapid-layer manufacturing, for biomedical applications.* Journal of the Mechanical Behavior of Biomedical Materials, 2009. **2**(1): p. 20-32.

7. Vrancken, B., et al., *Microstructure and mechanical properties of a novel beta titanium metallic composite by selective laser melting.* Acta Materialia, 2014. **68**(15): p. 150-158.

8. Louvis, E., P. Fox, and C.J. Sutcliffe, *Selective laser melting of aluminium components.* Journal of Materials Processing Technology, 2011. **211**(2): p. 275-284.

9. Loh, L.E., et al., *Numerical investigation and an effective modelling on the Selective Laser Melting (SLM) process with aluminium alloy 6061.* International Journal of Heat and Mass Transfer, 2015. **80**: p. 288-300.

10. Mumtaz, K.A., P. Erasenthiran, and N. Hopkinson, *High density selective laser melting of Waspaloy (R).* Journal of Materials Processing Technology, 2008. **195**(1-3): p. 77-87.

11. Kanagarajah, P., et al., *Inconel 939 processed by selective laser melting: Effect of microstructure and temperature on the mechanical properties under static and cyclic loading.* Materials Science and Engineering a-Structural Materials Properties Microstructure and Processing, 2013. **588**: p. 188-195.

12. Li, X.P., et al., *The role of a low-energy-density re-scan in fabricating crack-free Al85Ni5Y6Co2Fe2 bulk metallic glass composites via selective laser melting.* Materials & Design, 2014. **63**: p. 407-411.

13. Pauly, S., et al., *Processing metallic glasses by selective laser melting.* Materials Today, 2013. **16**(1-2): p. 37-41.

14. Yuan, P.P., D.D. Gu, and D.H. Dai, *Particulate migration behavior and its mechanism during selective laser melting of TiC reinforced Al matrix nanocomposites.* Materials & Design, 2015. **82**: p. 46-55.

15. Jia, Q.B. and D.D. Gu, *Selective laser melting additive manufacturing of TiC/Inconel 718 bulk-form nanocomposites: Densification, microstructure, and performance.* Journal of Materials Research, 2014. **29**(17): p. 1960-1969.

16. Markl, M. and C. Körner, *Multi-Scale Modeling of Powder-Bed-Based Additive Manufacturing.* Annual Review of Materials Research, 2016. **46**: p. 1-34.

17. Ma, J., et al., *Spatial Control of Functional Response in 4D-Printed Active Metallic Structures.* Scientific Reports, 2017. **7**.

18. Leuders, S., et al., *On the mechanical behaviour of titanium alloy TiAl6V4 manufactured by selective laser melting: Fatigue resistance and crack growth performance.* International Journal of Fatigue, 2013. **48**: p. 300-307.

19. Kerwien, S., et al., *Measurement Science Roadmap for Metal-based Additive Manufacturing*. 2013, NIST.

20. Zhang, B., Y. Li, and Q. Bai, *Defect formation mechanisms in selective laser melting: a review.* Chinese Journal of Mechanical Engineering, 2017. **30**(3): p. 515-527.

21. Pollock, D.D., *Thermocouples: theory and properties*. 1991: CRC press.

22. Tapia, G. and A. Elwany, *A review on process monitoring and control in metal-based additive manufacturing.* Journal of Manufacturing Science and Engineering, 2014. **136**(6): p. 060801.

23. Everton, S.K., et al., *Review of in-situ process monitoring and in-situ metrology for metal additive manufacturing.* Materials & Design, 2016. **95**: p. 431-445.

24. Rice, R.C., *Metallic Materials Properties Development and Standardization (MMPDS): Chapters 1-4*. Vol. 1. 2003: National Technical Information Service.

25. Khairallah, S.A., et al., *Laser powder-bed fusion additive manufacturing: Physics of complex melt flow and formation mechanisms of pores, spatter, and denudation zones.* Acta Materialia, 2016. **108**: p. 36-45.

26. Foroozmehr, A., M. Badrossamay, and E. Foroozmehr, *Finite element simulation of selective laser melting process considering optical penetration depth of laser in powder bed.* Materials & Design, 2016. **89**: p. 255-263.

27. Madenci, E. and I. Guven, *The finite element method and applications in engineering using ANSYS®*. 2015: Springer.

28. Karma, A., *Phase-field formulation for quantitative modeling of alloy solidification.* Physical Review Letters, 2001. **87**(11): p. 115701.

29. Yu, F., et al., *Phase field modeling of solidification microstructure evolution during welding.* Journal of Materials Processing Technology, 2018. **255**: p. 285-293.

30. Attari, V. and R. Arroyave, *Phase Field Modeling of Joint Formation During Isothermal Solidification in 3DIC Micro Packaging.* Journal of Phase Equilibria and Diffusion, 2016. **37**(4): p. 469-480.

31. Steinbach, I. and M. Apel, *Multi phase field model for solid state transformation with elastic strain.* Physica D: Nonlinear Phenomena, 2006. **217**(2): p. 153-160.

32. Heo, T.W. and L.-Q. Chen, *Phase-field modeling of nucleation in solid-state phase transformations.* Jom, 2014. **66**(8): p. 1520-1528.

33. Yi, S.-i., et al., *Strain-induced suppression of the miscibility gap in nanostructured Mg 2 Si–Mg 2 Sn solid solutions.* Journal of Materials Chemistry A, 2018. **6**(36): p. 17559-17570.

34. Attari, V., A. Cruzado, and R. Arroyave, *Exploration of the microstructure space in tialzrn ultra-hard nanostructured coatings.* arXiv preprint arXiv:1811.05017, 2018.

35. Acharya, R., J.A. Sharon, and A. Staroselsky, *Prediction of microstructure in laser powder bed fusion process.* Acta Materialia, 2017. **124**: p. 360-371.

36. Ghosh, S., et al., *On the primary spacing and microsegregation of cellular dendrites in laser deposited Ni–Nb alloys.* Modelling and Simulation in Materials Science and Engineering, 2017. **25**(6): p. 065002.

37. Keller, T., et al., *Application of finite element, phase-field, and CALPHAD-based methods to additive manufacturing of Ni-based superalloys.* Acta materialia, 2017. **139**: p. 244-253.

38. Bauereiß, A., T. Scharowsky, and C. Körner, *Defect generation and propagation mechanism during additive manufacturing by selective beam melting.* Journal of Materials Processing Technology, 2014. **214**(11): p. 2522-2528.

39. Cheng, B., et al., *On Process Temperature in Powder-Bed Electron Beam Additive Manufacturing: Model Development and Validation.* Journal of Manufacturing Science and Engineering, 2014. **136**(6): p. 061018.

40. Jamshidinia, M., F. Kong, and R. Kovacevic, *Numerical Modeling of Heat Distribution in the Electron Beam Melting® of Ti-6Al-4V.* Journal of Manufacturing Science and Engineering, 2013. **135**(6): p. 061010.

41. Hussein, A., et al., *Finite element simulation of the temperature and stress fields in single layers built without-support in selective laser melting.* Materials & Design, 2013. **52**: p. 638-647.

42. Ladani, L., et al., *Effective liquid conductivity for improved simulation of thermal transport in laser beam melting powder bed technology.* Additive Manufacturing, 2017. **14**: p. 13-23.

43. Masmoudi, A., R. Bolot, and C. Coddet, *Investigation of the laser–powder–atmosphere interaction zone during the selective laser melting process.* Journal of Materials Processing Technology, 2015. **225**: p. 122-132.

44. Chiumenti, M., et al., *Numerical simulation and experimental calibration of Additive Manufacturing by blown powder technology. Part I: thermal analysis.* Rapid Prototyping Journal, 2017. **23**(2): p. 448-463.

45. Denlinger, E.R., et al., *Thermomechanical model development and in situ experimental validation of the Laser Powder-Bed Fusion process.* Additive Manufacturing, 2017. **16**: p. 73-80.

46. Nikam, S.H. and N.K. Jain, *Three-dimensional thermal analysis of multi-layer metallic deposition by micro-plasma transferred arc process using finite element simulation.* Journal of Materials Processing Technology, 2017.

47. Fu, C. and Y. Guo. *3-Dimensional Finite Element Modeling of Selective Laser Melting Ti-6Al-4V Alloy*. in *Solid Freeform Fabrication Symposium 2014 Proceedings*. 2014.

48. Huang, Y., et al., *Finite element analysis of thermal behavior of metal powder during selective laser melting.* International Journal of Thermal Sciences, 2016. **104**: p. 146-157.

49. Khairallah, S.A. and A. Anderson, *Mesoscopic simulation model of selective laser melting of stainless steel powder.* Journal of Materials Processing Technology, 2014. **214**(11): p. 2627-2636.

50. Ganeriwala, R. and T.I. Zohdi, *A coupled discrete element-finite difference model of selective laser sintering.* Granular Matter, 2016. **18**(2): p. 1-15.

51. Qiu, C., et al., *On the role of melt flow into the surface structure and porosity development during selective laser melting.* Acta Materialia, 2015. **96**: p. 72-79.

52. Leitz, K.-H., et al., *Multi-physical simulation of selective laser melting.* Metal Powder Report, 2016.

53. Panwisawas, C., et al., *Mesoscale modelling of selective laser melting: Thermal fluid dynamics and microstructural evolution.* Computational Materials Science, 2017. **126**: p. 479-490.

54. Matsumoto, M., et al., *Finite element analysis of single layer forming on metallic powder bed in rapid prototyping by selective laser processing.* International Journal of Machine Tools and Manufacture, 2002. **42**(1): p. 61-67.

55. Kolossov, S., et al., *3D FE simulation for temperature evolution in the selective laser sintering process.* International Journal of Machine Tools and Manufacture, 2004. **44**(2): p. 117-123.

56. Zäh, M., et al. *Determination of Process Parameters for Electron Beam Sintering (EBS)*. in *Excerpt from the Proceedings of the COMSOL Conference Hannover*. 2008.

57. Li, R., et al., *Effects of processing parameters on the temperature field of selective laser melting metal powder.* Powder Metallurgy and Metal Ceramics, 2009. **48**(3-4): p. 186-195.

58. Roberts, I., et al., *A three-dimensional finite element analysis of the temperature field during laser melting of metal powders in additive layer manufacturing.* International Journal of Machine Tools and Manufacture, 2009. **49**(12): p. 916-923.

59. Verhaeghe, F., et al., *A pragmatic model for selective laser melting with evaporation.* Acta Materialia, 2009. **57**(20): p. 6006-6012.

60. Zhang, D., et al., *Select laser melting of W–Ni–Fe powders: simulation and experimental study.* The International Journal of Advanced Manufacturing Technology, 2010. **51**(5-8): p. 649-658.

61. Contuzzi, N., S. Campanelli, and A. Ludovico, *3 D FINITE ELEMENT ANALYSIS IN THE SELECTIVE LASER MELTING PROCESS.* International Journal of Simulation Modelling, 2011. **10**(3): p. 113-121.

62. Shen, N. and K. Chou. *Thermal modeling of electron beam additive manufacturing process: Powder sintering effects*. in *ASME 2012 International Manufacturing Science and Engineering Conference collocated with the 40th North American Manufacturing Research Conference and in participation with the International Conference on Tribology Materials and Processing*. 2012. American Society of Mechanical Engineers.

63. Shen, N. and Y. Chou. *Numerical thermal analysis in electron beam additive manufacturing with preheating effects*. in *Proceedings of the 23rd Solid Freeform Fabrication Symposium, Austin, TX*. 2012.

64. Antony, K., N. Arivazhagan, and K. Senthilkumaran, *Numerical and experimental investigations on laser melting of stainless steel 316L metal powders.* Journal of Manufacturing Processes, 2014. **16**(3): p. 345-355.

65. Dai, D. and D. Gu, *Thermal behavior and densification mechanism during selective laser melting of copper matrix composites: simulation and experiments.* Materials & Design, 2014. **55**: p. 482-491.

66. Li, Y. and D. Gu, *Parametric analysis of thermal behavior during selective laser melting additive manufacturing of aluminum alloy powder.* Materials & Design, 2014. **63**: p. 856-867.

67. Li, Y. and D. Gu, *Thermal behavior during selective laser melting of commercially pure titanium powder: Numerical simulation and experimental study.* Additive Manufacturing, 2014. **1**: p. 99-109.

68. Mohanty, S. and J.H. Hattel, *Numerical model based reliability estimation of selective laser melting process.* Physics Procedia, 2014. **56**: p. 379-389.

69. Criales, L.E., Y.M. Arısoy, and T. Özel. *A Sensitivity Analysis Study on the Material Properties and Process Parameters for Selective Laser Melting of Inconel 625*. in *ASME 2015 International Manufacturing Science and Engineering Conference*. 2015. American Society of Mechanical Engineers.

70. Dai, D. and D. Gu, *Tailoring surface quality through mass and momentum transfer modeling using a volume of fluid method in selective laser melting of TiC/AlSi10Mg powder.* International Journal of Machine Tools and Manufacture, 2015. **88**: p. 95-107.

71. Loh, L.-E., et al., *Numerical investigation and an effective modelling on the Selective Laser Melting (SLM) process with aluminium alloy 6061.* International Journal of Heat and Mass Transfer, 2015. **80**: p. 288-300.

72. Ma, L., et al. *Using design of experiments in finite element modeling to identify critical variables for laser powder bed fusion*. in *International Solid Freeform Fabrication Symposium*. 2015. Laboratory for Freeform Fabrication and the University of Texas Austin, TX, USA.

73. Romano, J., et al., *Temperature distribution and melt geometry in laser and electron-beam melting processes–A comparison among common materials.* Additive Manufacturing, 2015. **8**: p. 1-11.

74. Romano, J., L. Ladani, and M. Sadowski, *Thermal Modeling of Laser Based Additive Manufacturing Processes within Common Materials.* Procedia Manufacturing, 2015. **1**: p. 238-250.

75. Tan, X., et al., *An experimental and simulation study on build thickness dependent microstructure for electron beam melted Ti–6Al–4V.* Journal of Alloys and Compounds, 2015. **646**: p. 303-309.

76. Yuan, P. and D. Gu, *Molten pool behaviour and its physical mechanism during selective laser melting of TiC/AlSi10Mg nanocomposites: simulation and experiments.* Journal of Physics D: Applied Physics, 2015. **48**(3): p. 035303.

77. Criales, L.E., Y.M. Arısoy, and T. Özel, *Sensitivity analysis of material and process parameters in finite element modeling of selective laser melting of Inconel 625.* The International Journal of Advanced Manufacturing Technology, 2016: p. 1-14.

78. Gu, D. and B. He, *Finite element simulation and experimental investigation of residual stresses in selective laser melted Ti–Ni shape memory alloy*. Computational Materials Science, 2016. **117**: p. 221-232.

79. Romano, J., L. Ladani, and M. Sadowski, *Laser Additive Melting and Solidification of Inconel 718: Finite Element Simulation and Experiment.* Jom, 2016. **68**(3): p. 967-977.

80. Vastola, G., et al., *Modeling the Microstructure Evolution During Additive Manufacturing of Ti6Al4V: A Comparison Between Electron Beam Melting and Selective Laser Melting.* JOM, 2016. **68**(5): p. 1370-1375.

81. Cheng, B. and K. Chou. *Melt Pool Evolution Study in Selective Laser Melting*. in *26th Annual International Solid Freeform Fabrication Symposium—An Additive Manufacturing Conference*. 2015.

82. Li, J. and Y. Shi, *Numerical Simulation of Transient Temperature Field in Selective Laser Melting.* China Mechanical Engineering, 2008. **19**(20): p. 2492-2495.

83. Zhao, B.-j. and F.-z. Shi, *Modeling of selective laser sintering for PC powder*. JOURNAL-BEIJING UNIVERSITY OF AERONAUTICS AND ASTRONAUTICS, 2002. **28**(6; ISSU 118): p. 660-663.

84. Yifu, S., G. Dongdong, and Y. Chenye, *Simulation of temperature field in direct metal laser sintering processes.* Chinese Mechanical Engineering, 2005. **16**(1): p. 67-73.

85. XING, J., et al., *Simulation and testing of the transient temperature field of infrared laser sintering.* Journal of Harbin Engineering University, 2011. **7**: p. 025.

86. Tolochko, N.K., et al., *Mechanisms of selective laser sintering and heat transfer in Ti powder.* Rapid prototyping journal, 2003. **9**(5): p. 314-326.

87. Gusarov, A., et al., *Heat transfer modelling and stability analysis of selective laser melting.* Applied Surface Science, 2007. **254**(4): p. 975-979.

88. Yang, Q., et al., *Finite element modeling and validation of thermomechanical behavior of Ti-6Al-4V in directed energy deposition additive manufacturing.* Additive Manufacturing, 2016.

89. Raghavan, N., et al., *Numerical modeling of heat-transfer and the influence of process parameters on tailoring the grain morphology of IN718 in electron beam additive manufacturing.* Acta Materialia, 2016. **112**: p. 303-314.

90. Vásquez, F., J.A. Ramos-Grez, and M. Walczak, *Multiphysics simulation of laser–material interaction during laser powder depositon.* The International Journal of Advanced Manufacturing Technology, 2012. **59**(9-12): p. 1037-1045.

91. Xia, M., et al., *Porosity evolution and its thermodynamic mechanism of randomly packed powder-bed during selective laser melting of Inconel 718 alloy.* International Journal of Machine Tools and Manufacture, 2017. **116**: p. 96-106.

92. Heeling, T., M. Cloots, and K. Wegener, *Melt pool simulation for the evaluation of process parameters in selective laser melting.* Additive Manufacturing, 2017. **14**: p. 116-125.

93. Liu, C., B. Wu, and J.X. Zhang, *Numerical investigation of residual stress in thick titanium alloy plate joined with electron beam welding.* Metallurgical and Materials Transactions B, 2010. **41**(5): p. 1129-1138.

94. Taylor, G.A., et al., *Finite volume methods applied to the computational modelling of welding phenomena.* Applied Mathematical Modelling, 2002. **26**(2): p. 311-322.

95. De, A. and T. DebRoy, *Improving reliability of heat and fluid flow calculation during conduction mode laser spot welding by multivariable optimisation.* Science and Technology of Welding & Joining, 2013.

96. Sih, S.S. and J.W. Barlow, *The prediction of the emissivity and thermal conductivity of powder beds.* Particulate science and technology, 2004. **22**(4): p. 427-440.

97. Yin, J., et al., *Simulation of temperature distribution in single metallic powder layer for laser micro-sintering.* Computational Materials Science, 2012. **53**(1): p. 333-339.

98. Neira Arce, A., *Thermal modeling and simulation of electron beam melting for rapid prototyping on Ti6Al4V alloys*. 2012.

99. Yang, J., et al., *Experimental investigation and 3D finite element prediction of the heat affected zone during laser assisted machining of Ti6Al4V alloy*. Journal of Materials Processing Technology, 2010. **210**(15): p. 2215-2222.

100. Gusarov, A. and I. Smurov, *Modeling the interaction of laser radiation with powder bed at selective laser melting.* Physics Procedia, 2010. **5**: p. 381-394.

101. Boley, C., S. Khairallah, and A. Rubenchik, *Calculation of laser absorption by metal powders in additive manufacturing.* Applied optics, 2015. **54**(9): p. 2477-2482.

102. Rubenchik, A., et al., *Direct measurements of temperature-dependent laser absorptivity of metal powders.* Applied optics, 2015. **54**(24): p. 7230-7233.

103. Rosenthal, D. *The theory of moving sources of heat and its application to metal treatments*. 1946. ASME.

104. Eagar, T. and N. Tsai, *Temperature fields produced by traveling distributed heat sources.* Welding Journal, 1983. **62**(12): p. 346-355.

105. Goldak, J., M. Bibby, and A. Chakravarti, *A double ellipsoid finite element model for welding heat sources*. 1985: International Institute of Welding.

106. Dong, L., et al., *Three-dimensional transient finite element analysis of the selective laser sintering process.* Journal of materials processing technology, 2009. **209**(2): p. 700-706.

107. Patil, R.B. and V. Yadava, *Finite element analysis of temperature distribution in single metallic powder layer during metal laser sintering.* International Journal of Machine Tools and Manufacture, 2007. **47**(7): p. 1069-1080.

108. Mumtaz, K. and N. Hopkinson, *Selective laser melting of thin wall parts using pulse shaping.* Journal of Materials Processing Technology, 2010. **210**(2): p. 279-287.

109. Morsbach, C., S. Höges, and W. Meiners, *Modeling the selective laser melting of polylactide composite materials.* Journal of Laser Applications, 2011. **23**(1): p. 012005.

110. Bai, J., et al., *Thermal Influence of CNT on the Polyamide 12 Nanocomposite for Selective Laser Sintering.* Molecules, 2015. **20**(10): p. 19041-19050.

111. Wang, X., et al., *Direct selective laser sintering of hard metal powders: experimental study and simulation.* The International Journal of Advanced Manufacturing Technology, 2002. **19**(5): p. 351-357.

112. Gusarov, A. and J.-P. Kruth, *Modelling of radiation transfer in metallic powders at laser treatment.* International Journal of Heat and Mass Transfer, 2005. **48**(16): p. 3423-3434.

113. Niebling, F., A. Otto, and M. Geiger. *Analyzing the DMLS-process by a macroscopic FE-model*. in *Proc. of 13th Solid Freeform Fabrication Symposium*. 2002.

114. Dai, K. and L. Shaw, *Thermal and stress modeling of multi-material laser processing.* Acta Materialia, 2001. **49**(20): p. 4171-4181.

115. Van Belle, L., G. Vansteenkiste, and J.C. Boyer. *Comparisons of numerical modelling of the Selective Laser Melting*. in *Key Engineering Materials*. 2012. Trans Tech Publ.

116. Zeng, K., D. Pal, and B. Stucker. *A review of thermal analysis methods in laser sintering and selective laser melting*. in *Proceedings of Solid Freeform Fabrication Symposium Austin, TX*. 2012.

117. Brook, G., *Smithells Metals Reference Book, Ed. by EA Brandes and GB Brook*. 1992, Butterworth-Heinemann Ltd., Oxford.

118. Mills, K.C., *Recommended values of thermophysical properties for selected commercial alloys*. 2002: Woodhead Publishing.

119. Multiphysics, C., *Heat Transfer Module User's Guide.* Documentation within Software Package, Ver, 2014. **4**.

120. Welsch, G., R. Boyer, and E. Collings, *Materials properties handbook: titanium alloys*. 1993: ASM international.

121. Fan, Y., et al., *Effect of phase transformations on laser forming of Ti–6Al–4V alloy*. Journal of applied physics, 2005. **98**(1): p. 013518.

122. Yadroitsev, I., et al., *Single track formation in selective laser melting of metal powders.* Journal of Materials Processing Technology, 2010. **210**(12): p. 1624-1631.

123. Thijs, L., et al., *A study of the microstructural evolution during selective laser melting of Ti–6Al–4V.* Acta Materialia, 2010. **58**(9): p. 3303-3312.

124. Kruth, J.-P., et al., *Selective laser melting of iron-based powder*. Journal of Materials Processing Technology, 2004. **149**(1): p. 616-622.

125. Shen, F., et al., *Finite element simulation of thermal distribution in direct metal laser multi-track sintering.* Journal of Sichuan University: Engineering Science Edition, 2005. **37**(1): p. 47-51.

126. Nakamura, H., et al., *Elucidation of melt flows and spatter formation mechanisms during high power laser welding of pure titanium.* Journal of Laser Applications, 2015. **27**(3): p. 032012.

127. Hijazi, A., et al., *A calibrated dual-wavelength infrared thermometry approach with non-greybody compensation for machining temperature measurements.* Measurement Science and Technology, 2011. **22**(2): p. 025106.

128. Larrick, T., *Understanding Modern Infrared Pyrometers for Demanding Steel Mill Applications*. Williamson Corporation, Concord MA , USA.

129. Bober, M. and J. Singer, *High temperature vapor pressures of stainless steel type 1.4970 and of some other pure metals from laser evaporation*. 1984, Kernforschungszentrum Karlsruhe GmbH (Germany.

130. Gu, D., et al., *Densification behavior, microstructure evolution, and wear performance of selective laser melting processed commercially pure titanium.* Acta Materialia, 2012. **60**(9): p. 3849-3860.

131. Dai, K. and L. Shaw, *Distortion minimization of laser-processed components through control of laser scanning patterns.* Rapid Prototyping Journal, 2002. **8**(5): p. 270-276.

132. Cheng, B. and K. Chou. *Melt pool geometry simulations for powder-based electron beam additive manufacturing*. in *24th Annual International Solid Freeform Fabrication Symposium-An Additive Manufacturing Conference, Austin, TX, USA*. 2013.

133. Bremen, S., W. Meiners, and A. Diatlov, *Selective laser melting.* Laser Technik Journal, 2012. **9**(2): p. 33-38.

134. Franco, B., et al., *A sensory material approach for reducing variability in additively manufactured metal parts.* Scientific Reports, 2017. **7**(1): p. 3604.

135. Markl, M., et al. *Numerical investigations of selective electron beam melting on the powder scale*. in *Proceedings of the Fraunhofer Direct Digital Manufacturing Conference*. 2016.

136. Karayagiz, K., et al., *Numerical and Experimental Analysis of Heat Distribution in the Laser Powder Bed Fusion of Ti-6 Al-4 V.* IISE Transactions, 2018(just-accepted): p. 1-44.

137. Pace, D.K., *Modeling and simulation verification and validation challenges.* Johns Hopkins APL Technical Digest, 2004. **25**(2): p. 163-172.

138. Schwer, L.E., *Guide for Verification and Validation in Computational Solid Mechanics.* 2009.

139. Committee, V., *Standard for verification and validation in computational fluid dynamics and heat transfer.* American Society of Mechanical Engineers: New York, NY, USA, 2009.

140. Thacker, B.H., et al., *Concepts of model verification and validation*. 2004, Los Alamos National Lab.

141. Liu, X., et al., *Vision 2040: A Roadmap for Integrated, Multiscale Modeling and Simulation of Materials and Systems.* 2018.

142. Ly, S., et al., *Metal vapor micro-jet controls material redistribution in laser powder bed fusion additive manufacturing.* Scientific Reports, 2017. **7**.

143. Pei, W., et al., *Numerical simulation and parametric analysis of selective laser melting process of AlSi10Mg powder.* Applied Physics A, 2017. **123**(8): p. 540.

144. Liu, Y., J. Zhang, and Z. Pang, *Numerical and experimental investigation into the subsequent thermal cycling during selective laser melting of multi-layer 316L stainless steel.* Optics & Laser Technology, 2018. **98**: p. 23-32.

145. Ghosh, S., et al., *Simulation of temperature, stress and microstructure fields during laser deposition of Ti–6Al–4V.* Modelling and Simulation in Materials Science and Engineering, 2018. **26**(7): p. 075005.

146. Denlinger, E.R., *Thermo-Mechanical Modeling of Large Electron Beam Builds*, in *Thermo-Mechanical Modeling of Additive Manufacturing*. 2018, Elsevier. p. 167-181.

147. DebRoy, T., et al., *Additive manufacturing of metallic components–process, structure and properties.* Progress in Materials Science, 2018. **92**: p. 112-224.

148. Frazier, W.E., *Metal additive manufacturing: a review.* Journal of Materials Engineering and Performance, 2014. **23**(6): p. 1917-1928.

149. Nastac, L., *Numerical modeling of solidification morphologies and segregation patterns in cast dendritic alloys.* Acta Materialia, 1999. **47**(17): p. 4253-4262.

150. Xu, Q.Y., et al., *Multiscale Modeling and Simulation of Directional Solidification Process of Ni-Based Superalloy Turbine Blade Casting.* Metals, 2018. **8**(8).

151. Asle Zaeem, M., *Advances in Modeling of Solidification Microstructures.* JOM, 2015. **67**(8): p. 1774-1775.

152. Karma, A. and D. Tourret, *Atomistic to continuum modeling of solidification microstructures.* Current Opinion in Solid State & Materials Science, 2016. **20**(1): p. 25-36.

153. Attari, V., et al., *On the interfacial phase growth and vacancy evolution during accelerated electromigration in Cu/Sn/Cu microjoints.* Acta Materialia, 2018. **160**: p. 185-198.

154. Zhu, M., S. Pan, and D. Sun, *Modeling of Microstructure Evolution During Alloy Solidification*, in *Advances in the Science and Engineering of Casting Solidification: An MPMD Symposium Honoring Doru Michael Stefanescu*, L. Nastac, et al., Editors. 2016, Springer International Publishing: Cham. p. 183-190.

155. Boettinger, W.J., et al., *Solidification microstructures: recent developments, future directions.* Acta Materialia, 2000. **48**(1): p. 43-70.

156. Rappaz, M., et al., *Modelling of Solidification Microstructures.* Materials Science Forum, 2000. **329-330**: p. 389-396.

157. Stefanescu, D.M., *Methodologies for Modeling of Solidification Microstructure and Their Capabilities.* ISIJ International, 1995. **35**(6): p. 637-650.

158. Körner, C., et al., *Tailoring the grain structure of IN718 during selective electron beam melting.* MATEC Web of Conferences, 2014. **14**: p. 08001.

159. Nie, P., O.A. Ojo, and Z. Li, *Numerical modeling of microstructure evolution during laser additive manufacturing of a nickel-based superalloy.* Acta Materialia, 2014. **77**: p. 85-95.

160. Lopez-Botello, O., et al., *Two-dimensional simulation of grain structure growth within selective laser melted AA-2024.* Materials & Design, 2017. **113**: p. 369-376.

161. Francois, M.M., et al., *Modeling of additive manufacturing processes for metals: Challenges and opportunities.* Current Opinion in Solid State and Materials Science, 2017: p. Medium: ED; Size: p. 198-206.

162. Ghosh, S., *Predictive modeling of solidification during laser additive manufacturing of nickel superalloys: recent developments, future directions.* Materials Research Express, 2018. **5**(1): p. 012001.

163. W. J. Boettinger, et al., *Phase-Field Simulation of Solidification.* Annual Review of Materials Research, 2002. **32**(1): p. 163-194.

164. Ode, M., S.G. Kim, and T. Suzuki, *Recent Advances in the Phase-field Model for Solidification.* ISIJ International, 2001. **41**(10): p. 1076-1082.

165. Echebarria, B., et al., *Quantitative phase-field model of alloy solidification.* Physical Review E, 2004. **70**(6): p. 061604.

166. Wang, S.L., et al., *Thermodynamically-consistent phase-field models for solidification.* Physica D: Nonlinear Phenomena, 1993. **69**(1): p. 189-200.

167. Keller, T., et al., *Application of finite element, phase-field, and CALPHAD-based methods to additive manufacturing of Ni-based superalloys.* Acta Materialia, 2017. **139**: p. 244-253.

168. Ghosh, S., N. Ofori-Opoku, and J.E. Guyer, *Simulation and analysis of γ-Ni cellular growth during laser powder deposition of Ni-based superalloys.* Computational Materials Science, 2018. **144**: p. 256-264.

169. Geng, R.-w., et al., *Simulation of microstructure evolution in fused-coating additive manufacturing based on phase field approach.* China Foundry, 2017. **14**(5): p. 346-352.

170. Steinbach, I., *Phase-field models in materials science.* Modelling and Simulation in Materials Science and Engineering, 2009. **17**(7): p. 073001.

171. Zhang, L. and I. Steinbach, *Phase-field model with finite interface dissipation: Extension to multi-component multi-phase alloys.* Acta Materialia, 2012. **60**(6-7): p. 2702-2710.

172. Ghosh, S., et al., *Uncertainty analysis of microsegregation during laser powder bed fusion.* Modelling and Simulation in Materials Science and Engineering, 2019. **27**(3): p. 034002.

173. Roehling, J.D., et al., *Rapid Solidification in Bulk Ti-Nb Alloys by Single-Track Laser Melting.* JOM, 2018. **70**(8): p. 1589-1597.

174. McKeown, J.T., et al., *Time-Resolved In Situ Measurements During Rapid Alloy Solidification: Experimental Insight for Additive Manufacturing.* JOM, 2016. **68**(3): p. 985-999.

175. Nomoto, S., M. Segawa, and H. Wakameda, *Non-equilibrium phase field model using thermodynamics data estimated by machine learning for additive manufacturing solidification.*

176. Ghosh, S., et al., *Formation of Nb-rich droplets in laser deposited Ni-matrix microstructures.* Scripta Materialia, 2018. **146**: p. 36-40.

177. Block-Bolten, A. and T.W. Eagar, *Metal vaporization from weld pools.* Metallurgical Transactions B, 1984. **15**(3): p. 461-469.

178. Trapp, J., et al., *In situ absorptivity measurements of metallic powders during laser powder-bed fusion additive manufacturing.* Applied Materials Today, 2017. **9**: p. 341-349.

179. Karayagiz, K., et al., *Numerical and experimental analysis of heat distribution in the laser powder bed fusion of Ti-6Al-4V.* IISE Transactions, 2019. **51**(2): p. 136-152.

180. Joubert, J.M., B. Sundman, and N. Dupin, *Assessment of the niobium–nickel system.* Calphad, 2004. **28**(3): p. 299-306.

181. Steinbach, I., *Why Solidification? Why Phase-Field?* JOM, 2013. **65**(9): p. 1096-1102.

182. Takaki, T., et al., *Two-dimensional phase-field simulations of dendrite competitive growth during the directional solidification of a binary alloy bicrystal.* Acta Materialia, 2014. **81**: p. 272-283.

183. Wei, H.L., J. Mazumder, and T. DebRoy, *Evolution of solidification texture during additive manufacturing.* Scientific Reports, 2015. **5**: p. 16446.

184. Scipioni Bertoli, U., et al., *On the limitations of Volumetric Energy Density as a design parameter for Selective Laser Melting.* Materials & Design, 2017. **113**: p. 331-340.

185. Mahmoudi, M., et al., *On the printability and transformation behavior of nickel-titanium shape memory alloys fabricated using laser powder-bed fusion additive manufacturing.* Journal of Manufacturing Processes, 2018. **35**: p. 672-680.

186. Kühn, G., *W. Kurz, D. J. Fisher, Fundamentals of Solidification. Trans Tech Publications, Switzerland-Germany-UK-USA, 1986 (Erstauflage 1984), 242 Seiten, zahlreiche Abbildungen und Tabellen, Sachwortindex, SFr 54.00, ISBN 0-87849-523-3.* Crystal Research and Technology, 1986. **21**(9): p. 1176-1176.

187. *Library.* MRS Bulletin, 2011. **28**(9): p. 674-675.

188. Danilov, D. and B. Nestler, *Phase-field modelling of solute trapping during rapid solidification of a Si–As alloy.* Acta Materialia, 2006. **54**(18): p. 4659-4664.

# APPENDIX A

## SUPPLEMENTARY MATERIAL (CHAPTER 2)

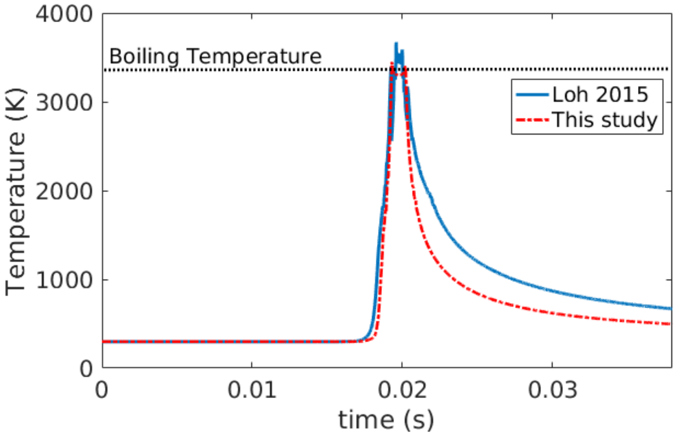

**Figure A.1**: Comparison of single-track thermal histories from two models using different evaporation methods. The peak temperatures are: 3315 K (this study), 3650 K (Loh 2015) [71]

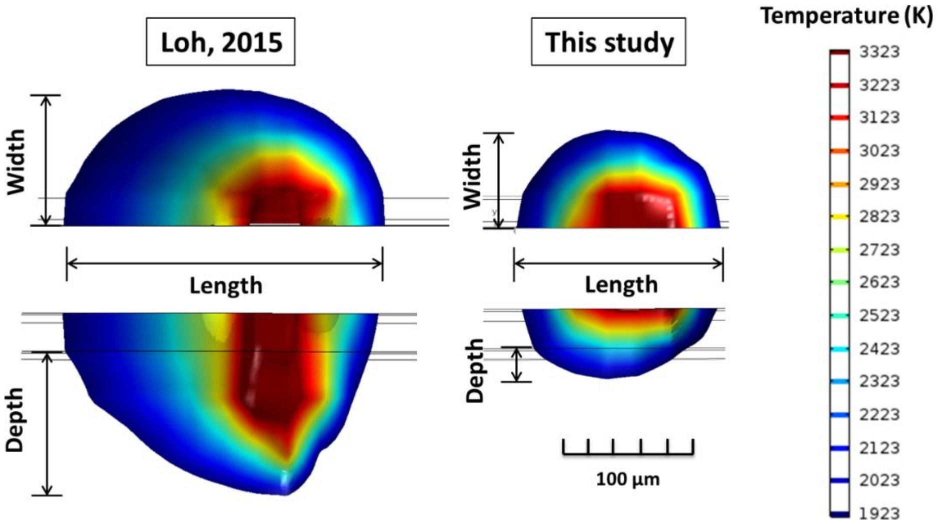

**Figure A.2:** Comparison of melt pool sizes from two models using different evaporation methods. The predicted melt pool length, width and depth in the substrate are: 149 µm, 144 µm, 22 µm for this study, and 246 µm, 210 µm, 112 µm for Loh, 2015 [71]

# APPENDIX B

## SUPPLEMENTARY MATERIAL (CHAPTER 4)

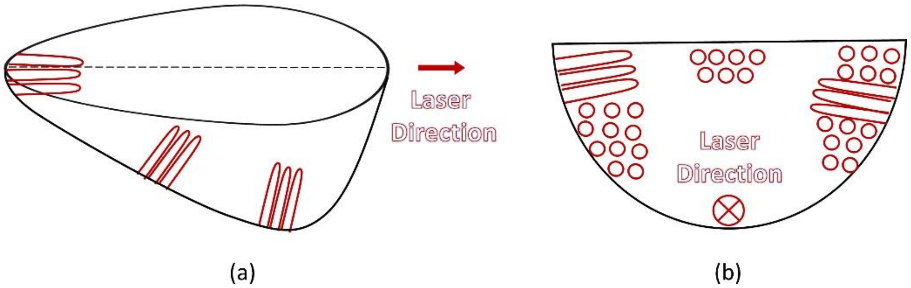

**Figure B.1**: The formation of cellular structures is shown in (a) longitudinal section (b) transverse section of melt pool. Depending on the orientation of the cells, two different view of cellular structure (columnar and circular) is observed in the transverse section of melt pool